Charge and Spin Effects in Semiconductor Nanostructures

A thesis presented

by

Andy Vidan

to

The Division of Engineering and Applied Sciences

in partial fulfillment of the requirements

for the degree of

Doctor of Philosophy

in the subject of

Applied Physics

Harvard University

Cambridge, Massachusetts

June 2006

Dissertation Advisor:
Professor Robert M. Westervelt

Author:
Andy Vidan

Charge and Spin Effects in Semiconductor Nanostructures

ABSTRACT

Semiconductor nanostructures are tunable systems and can serve as probes of strongly correlated electron behavior. These nanostructured devices are also promising candidates for building blocks of efficient, highly parallel nanoelectronic circuits and spin-qubit circuits. In this thesis, we present low-temperature transport measurements of semiconductor quantum dots and nanowires. We explore charge and spin effects in the context of the Coulomb blockade and the collective many-body phenomena of the Kondo effect and superconductivity.

In the first part of this thesis, we present experiments on quantum dots defined in GaAs/AlGaAs heterostructures containing two-dimensional electron gases. We investigate a triple quantum dot artificial molecule, where the three dots are arranged in a ring structure. When asymmetric coupling is introduced in the system, we show that the three coupled quantum dots in the Coulomb blockade regime act as an electron rectifier. This triple dot system can be used as a single-electron charge rectifier in single-electron circuits. A symmetric triple dot artificial molecule is also investigated. We supplement our experimental investigations with numerical calculations to determine the singlet-triplet splitting for a two electron triple quantum dot.

In a separate experiment, we investigate a quantum dot containing just one or two electrons in the Kondo regime. We observe several sharp peaks in the differential conductance, occurring at both zero and finite source-drain bias, for the one and two

electron quantum dot. At zero source-drain bias, the temperature and magnetic field dependence of the conductance is consistent with a standard Kondo resonance. The peaks at finite-bias are related to a Kondo effect through excited states of the quantum dot. Measurements in an applied magnetic field were also performed to probe these additional Kondo resonances.

In the second part of this thesis, we present transport measurements of one-dimensional hole gases formed in Ge/Si core/shell heterostructure nanowires. When connected to superconducting aluminum electrodes, a dissipationless supercurrent flows through the semiconductor nanowire. By using a local top gate, which modulates the carrier density of the nanowire and the number of one-dimensional subbands populated, the critical current can be tuned. Resonant multiple Andreev reflections in the superconductor-nanowire-superconductor system is also observed. Finally, we investigate the interplay between one-dimensional quantum confinement and superconductivity.

CONTENTS

ACKNOWLEDGEMENTS

When thinking of the numerous people who contributed to my studies, I am reminded of the proverb "It takes a village to raise a child." It seems to me that the support of an entire city worth of people is needed to complete a PhD here at Harvard. Each individual that I have encountered, from my professors to my undergraduates, from the technical support staff to my fellow graduate students, has helped me in this long journey.

I would like to begin by thanking my thesis advisor Bob Westervelt for his support and counsel throughout my five years as a graduate student. First and foremost, he taught me what it takes to be an excellent physicist. He encouraged me to collaborate with others, which tremendously helped in developing me as a scientist. Bob's suggestions and advice were always insightful and correct, and I feel privileged to have benefited from his expertise.

At Harvard, I had the opportunity to interact with extremely brilliant and accomplished physicists. I would like to begin by thanking the members of my thesis committee, Professor Federico Capasso, Professor Eric Heller, and Professor Venky Narayanamurti. I value the time they spent with me, following my progress over the years. While studying the superconducting proximity effect in nanowires, I encountered the BTK Theory and was excited to learn that the T in BTK is Professor Michael Tinkham. I am grateful to Professor Tinkham for his input and interest in my work. It was a pleasure to be able to interact with him and learn from him. I enjoyed serving as a Teaching Fellow under the guidance of Professor Tim Kaxiras. His exceptional teaching methods taught me how to appropriately relay difficult mathematical concepts in a simple

manner. Dr. Michael Stopa has been a great friend and confidant. His cheerful and positive personality constantly helped me see the brighter side of life. I will always appreciate his enthusiasm to carry out numerous simulations to supplement my research. Mike's exceptional knowledge of computation and mesoscopic physics has enhanced both my understanding of quantum dots and the depth of my research.

I would like to thank Jie Xiang and Professor Charlie Lieber for providing the Ge/Si nanowires. In addition to being a fantastic partner in the nanowire project, Jie is an outstanding person. I truly enjoyed all of our conversations while working with him, regardless of their relevance to physics.

Micah Hanson and Professor A.C. Gossard deserve special mention for providing the excellent GaAs/AlGaAs wafers without which my research could not have been performed.

I am extremely fortunate to have been surrounded by such talented peers in the Westervelt Group. It has been a pleasure to get to know all of them. I thank Ian Chan for showing me around the lab and teaching me his fabrication and measurement techniques. None of the work in this thesis would have been possible without the training I received from him. Parisa Fallahi was the other quantum dots student when I joined, and also helped in training me. I thank her for always being encouraging and helpful. Kathy Aidala and I joined the group together and are now graduating together – it was fun to be able to share similar experiences with her throughout our time at Harvard. Kathy was always around to talk whenever I needed a sounding board. I thank her for listening. Ania Bleszynski taught me a tremendous deal about organization and motivation. Tom Hunt and David Issadore were always able to provide me with creative solutions to all my

technical problems. I would like to also thank Jonathan Aguilar, the undergraduate working in our group, for being enthusiastic about our research and devoting his free time to conduct research in the lab. Also, thanks to REU undergraduate Alin Cosmanescu for working with me over the summer. He reminded me why research is better than programming and how to always make time for fun. Thanks to former group members Chungsok Lee, Hak-Ho Lee, and Brian LeRoy for their willingness to help and readiness to share their experiences. Thanks to Katie Humphry for many wonderful discussions and for knitting the most amazing baby booties. I would also like to express my appreciation to Ben Lee and Muhammed Yildirim for being good friends. Muhammed made work entertaining and I thank him for sharing with me his insights on a wide variety of topics. Best of luck to Erin Boyd, Melaku Muluneh, and Halvar Trodahl who have recently joined the Westervelt group.

My work would not have been successful without the assistance of the greater physics community. Steve Shepard really kept the clean rooms running smoothly ensuring that all the equipment remained functional, which has made the many hours I spent fabricating in the clean rooms enjoyable. Steve was always around to help with any fabrication issues and was always willing to share his knowledge about material science and instrumentation techniques. Yuan Lu trained me in electron beam lithography and always kept the electron microscopes in their optimal condition. I appreciate his enthusiasm in always trying to help with the lithography process. John Tsakirgis has also been a great help in the clean room and was of great assistance in getting the leak detector back from Pfieffer! Louis DeFeo and his team of expert machinists have always been ready to help. I will always be grateful to you guys for helping me during the

dilution fridge fiasco. Thanks to Tinkham Group members Steve Cronin, John Free, William Neils, and Sergio Valenzuela. It was always a pleasure to spend lunchtime talking with all of you. In particular, Sergio and Will were always eager to help with experimental problems and with the dilution fridge operation. I enjoyed sharing the fridges with them. Thanks to all the Marcus and Capasso group members, including Jiming Bao, Michael Biercuk, Nathaniel Craig, Ertugrul Cubukcu, Leonardo Di Carlo, Alex Johnson, Edward Laird, Nadya Mason, Jeff Miller, Jason Petta, Jenny Smythe, Yiming Zhang, and Dominik Zumbuhl, for making McKay Lab a nice place to work. I would also like to thank Susan Wieczorek and Naomi Brave for helping with all the problems that inevitably arise during a graduate student's hectic life.

I would like to thank my professors at Cornell in the Applied and Engineering Physics Department, especially Professor Joel Brock, Professor Bob Buhrman, and Professor Frank Wise, for being excellent mentors and inspiring me to pursue a career in physics.

I would like to thank Jean Herbert and Brian Kimball at NSC for allowing me to spend time working in their laboratories. Their approach towards science and technology has been a strong positive influence on me.

Josh Amini, David Elson, Steven Jaspan, Michael Meltzer, Jonathan Salfeld, Daniel Setzman, Michael Sorokorensky, and David Turkel-Parrella were always able to cheer me up and encourage me. I will always remember how they never missed an opportunity to point out that I am not in New York.

The love and support of my family was integral to my success. My sincerest gratitude goes to my father for consistently pushing me to achieve my best and for always

directing me to follow the right path, my mother for always being understanding of me and for the constant encouragement she provided, my sister for always caring for me, and my brother Erez who taught me everything I know and whose constant ridicule keeps me motivated. Also, thank you to the Sussman family for always being proud of me.

Thank you to my wife Eliana for encouraging me to work hard and for always supporting me. I truly appreciate how understanding and patient she was during the numerous episodes where the dilution fridge controlled my life. I will forever be grateful to her for standing by me. Finally, to my beautiful baby Asher: you are my inspiration. I cannot imagine life without you.

I

INTRODUCTION

1.1 Overview

The combination of physics, material science, and device engineering has proved to be very valuable. The ability to artificially create new materials allows and inspires new device concepts. For example, band structure engineering [1] of semiconductor heterostructures has allowed for many new electronic and optical devices. The development of compound semiconductor technologies, and the ability to scale down the size of field-effect transistors and other electronic components, has led to an extraordinary success for semiconductor electronics. However, new device concepts and computing architectures are now needed to continue such a trend. With advances in nanoscale science, the ability to create small, artificial structures is now possible, as is the precise control over the position and movement of electrons and atoms. This level of control allows for developments of smaller electronic components that have the potential to replace the conventional field-effect transistor and also offer the possibility for the eventual realization of a quantum computer.

Aside from improvements to technology, our ability to create structures at the nanoscale has also allowed for the study of low-dimensional electron systems and many-body physics. The most compelling illustrations of this are the experimental discoveries of the integer [2] and fractional quantum Hall effect [3]. The fractional quantum Hall effect, where electrons condense into liquid-like states, is a correlation-dominated two-

dimensional electron system in the extreme quantum limit [4]. These low-dimensional electron systems are some of the most fascinating systems in condensed matter physics.

In order to investigate lower-dimensional electron systems, the dimensionality needs to be reduced by confining the electrons in certain directions. In this thesis, we investigate electron transport in semiconductor quantum dots and nanowires, where the techniques of band structure engineering are employed to create a two-dimensional electron gas and a one-dimensional hole gas. These nanostructures are tunable systems, ideal for studying the electrical properties of confined electrons. Furthermore, these nanostructures can be used as the building blocks in future nanoelectronic circuits and quantum computers. An example of a coupled quantum dot system studied in this thesis is shown in Figure 1.1 (a).

Zero-dimensional quantum dots and one-dimensional nanowires have also revealed interesting and rich physics. In this thesis, we have the opportunity to investigate strongly correlated electron systems. Using a quantum dot containing just one or two electrons, we study the Kondo effect and investigate the effect of a multilevel quantum dot energy spectrum on the Kondo resonances. Using semiconductor nanowires contacted by superconducting electrodes, we study proximity-induced superconductivity and observe dissipationless supercurrents flowing through the nanowires. We also investigate the interplay between one-dimensional quantum confinement and superconductivity. A schematic of the Ge/Si nanowire studied in this thesis is shown in Figure 1.1 (b). The nanowires are one-dimensional and can be operated in the regime where only the first few one-dimensional subbands are populated.

(a)

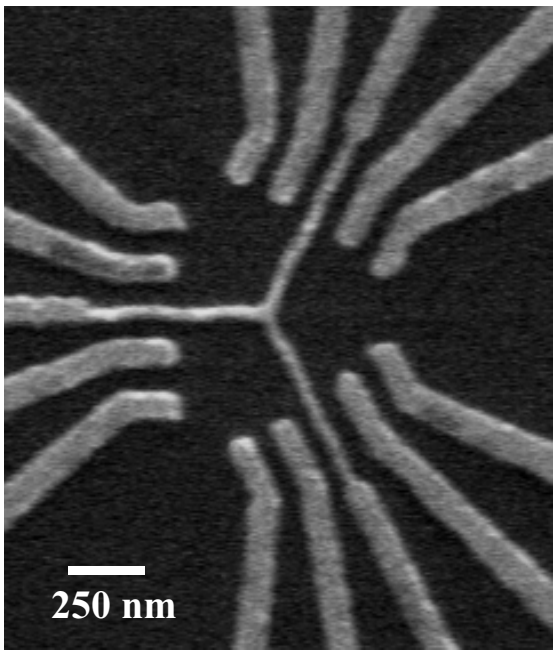

(b)

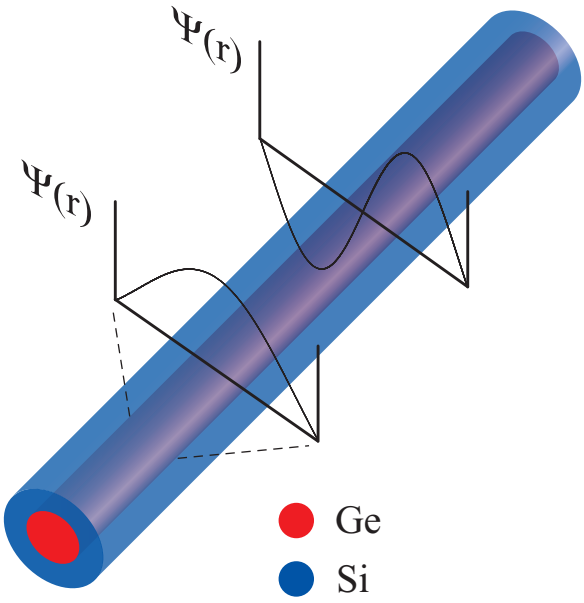

Figure 1.1 (a) Scanning electron micrograph of a triple quantum dot fabricated in a GaAs/AlGaAs heterostructure containing a two-dimensional electron gas. (b) Schematic of a one-dimensional Ge/Si core/shell heterostructure nanowire which can be tuned down to contain just the first few 1D modes.

1.2 Outline

This thesis focuses on the electrical properties of two low-dimensional systems: semiconductor quantum dots and semiconductor nanowires. The quantum dots are fabricated in a GaAs/AlGaAs heterostructure containing a two-dimensional electron gas and the nanowires are Ge/Si core/shell heterostructures containing a one-dimensional hole gas. A brief overview of the structure of the thesis is as follows:

In the first part of this thesis, we discuss our work on semiconductor quantum dots. In **Chapter 2**, useful background material is presented, covering the properties of the two-dimensional electron gas and quantum dots. **Chapter 3** describes the fabrication techniques used to form the quantum dots and the experimental setups for the low-temperature electrical measurements. A discussion of Shubnikov-de Haas oscillations and the measurements used to determine the sheet carrier density and mobility is also provided. **Chapter 4** covers our studies of triple quantum dots, artificial molecules consisting of three coupled quantum dots. The three dots are arranged in a ring structure, with each dot coupled to the other two dots. We begin with a derivation of the triple dot stability diagram, followed by experimental results on a triple dot charge rectifier. We also present numerical results, using density functional theory and exact diagonalization, of the exchange interaction in a two-electron triple quantum dot. **Chapter 5** describes our experiments regarding a few-electron quantum dot. The quantum dot can be tuned down to contain just one or two electrons while maintaining strong coupling to the leads, ideal for the study of the Kondo effect. We measure several sharp peaks in the differential conductance for the one and two electron quantum dot that we attribute to a Kondo effect through excited states of the quantum dot.

The second part of this thesis describes our experimental study of Ge/Si nanowires. Semiconductor nanowires are finding increased importance in nanoelectronics due to their controlled growth and reduced dimensions. **Chapter 6** describes our unique one-dimensional nanowires. The nanowires have a core/shell (radial heterostructure) geometry. The 15 nm diameter core is made of germanium and the 2 nm thick shell is made of silicon. Due to a valence band offset, holes are confined to the core, and a one-dimensional hole gas is formed. Nonlinear conductance measurements of the nanowires, demonstrating one-dimensional quantum confinement, are also presented in this chapter. The chapter concludes with a review covering useful background information on proximity-induced superconductivity. In **Chapter 7**, we present a thorough experimental investigation of proximity-induced superconductivity in Ge/Si nanowires. The first section of this chapter covers experimental techniques and low-noise electronic filtering. The second and third sections describe low-temperature transport measurements of the nanowires in the superconducting state. We measure tunable dissipationless supercurrents and resonant multiple Andreev reflections in the superconductor-nanowire hybrid structure. The final section describes the interplay of one-dimensional modes and superconductivity.

II

GaAs/AlGaAs HETEROSTRUCTURES AND SPLIT-GATE DEVICES

2.1 Overview

Two-dimensional electron systems realized in semiconductor heterostructures provide an ideal material to study, in a controlled way, coherent quantum mechanical effects in electron transport. In Section 2.2, we introduce the high mobility GaAs/AlGaAs two-dimensional electron gas, and give a short review of its main physical and electrical properties. The low carrier density in this system, compared to metallic systems, results in a relatively large Fermi wavelength. Therefore, using standard semiconductor processing techniques, fabrication of split-gate devices with features comparable to the Fermi wavelength is possible and allows for quantum effects in transport to be observed. Section 2.3 describes the quantum point contact and the phenomenon of quantized conductance. In Section 2.4, we describe the transport properties of a quantum dot and review single-electron tunneling and the Coulomb blockade. Finally, in Section 2.5, we describe the double quantum dot system and present data on a few-electron double dot device that we have fabricated. Information regarding processing, fabrication, and measurement techniques is described in Chapter 3.

2.2 Two-Dimensional Electron Gas

By using a modulation-doped [5] GaAs/$Al_xGa_{1-x}As$ heterostructure, grown by molecular beam epitaxy [6,7], we can confine the motion of electrons to the plane perpendicular to the growth direction, at the interface between the GaAs and $Al_xGa_{1-x}As$

layers. The motivation behind using a heterostructure is the concept of band structure engineering. Using two different materials with different band gaps E_g, in this case GaAs (E_g = 1.41 eV) and $Al_{0.3}Ga_{0.7}As$ (E_g = 1.75 eV), we can form a straddling alignment of the conduction and valence bands at the heterojunction, as shown in Figure 2.1 (a). Due to the conduction band offset of approximately 300 meV, carriers prefer the GaAs layer. Doping the heterostructure with Si provides conduction electrons which migrate to the GaAs layer. This process leaves behind positively charged Si ions that create an electric field that bends the conduction band. The electrons are then confined to a narrow triangular well of approximately 10 nm that is formed at the heterojunction.

In general, for our heterostructures, the doping efficiency is such that roughly one-half of the Si donors are thermally activated. Furthermore, more electrons from the ionized Si donors migrate to the surface rather than to the GaAs layer to satisfy the surface states.

Electrons at the heterojunction are free to move in the x-y plane (parallel to the growth direction) but motion in the z-direction is quantized inside the narrow well. Assuming a triangular potential, as shown in Figure 2.1 (b), we can solve for the energy levels in the quantum well [8,9]. The well is modeled by an electric field $F = 4\pi n_s/\varepsilon$ due to the ionized Si donors, where n_s is the sheet carrier density and $\varepsilon = 13$ is the dielectric constant of GaAs, and an infinite barrier at the heterojunction. Solutions of the Schrödinger equation take the form of

$$\psi(\vec{r}, z) = Ae^{i\vec{k}\cdot\vec{r}}\varphi_n(z) \tag{2.1}$$

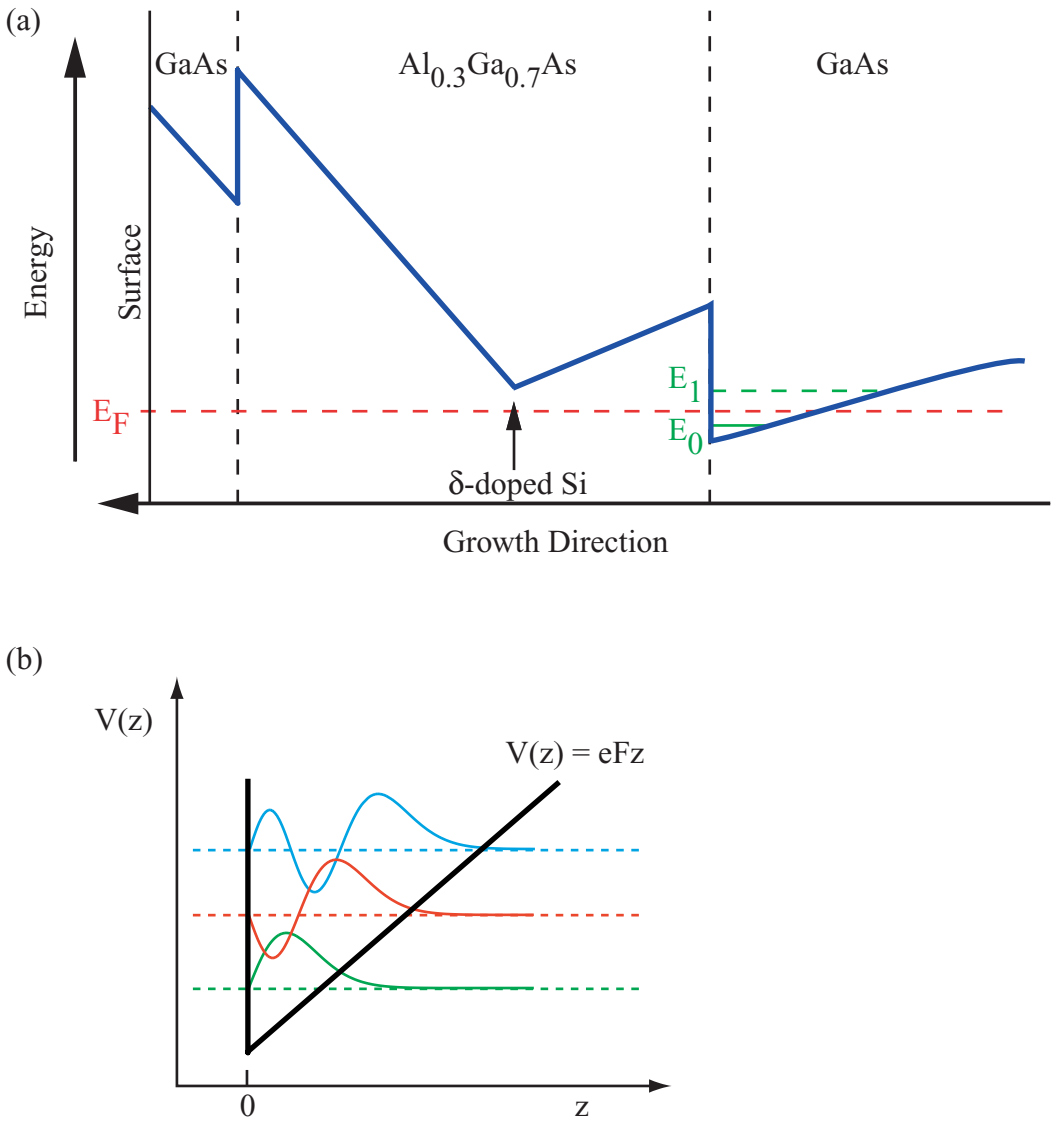

Figure 2.1 (a) Conduction band energy versus growth direction of a GaAs/$Al_{0.3}Ga_{0.7}As$ heterostructure. A conduction band offset at the heterojunction is present. Silicon donors supply conduction electrons which migrate toward the GaAs layer leaving behind positively charged ions. An electric field is generated which bends the conduction band edge and confines the electrons to a narrow region approximately 10 nm wide.
(b) Triangular well approximation of the GaAs-$Al_{0.3}Ga_{0.7}As$ interface, showing the first three solutions (Airy functions) of the Schrödinger equation. At low temperature and low dopant concentration, only the lowest energy level is occupied.

corresponding to free electron motion in the x-y plane and quantized eigenstates in the z-direction. $\varphi_n(z)$ are the well known Airy functions depicted in Figure 2.1 (b). The eigenenergies are given by

$$E_n = \left(\frac{\hbar^2}{2m^*}\right)^{1/3}\left(\frac{3\pi F}{2}\left[n+\frac{3}{4}\right]\right)^{2/3} \tag{2.2}$$

The first excited state is approximately 150 meV above the ground state. At dilution refrigerator temperature with $k_B T \le 100\ \mu eV$ and low carrier sheet density (low dopant concentration), electrons occupy only the lowest energy level with a negligible probability for excitation to the higher states. Electrons are therefore confined in the z-direction, but remain free in the x-y plane, resulting in a two-dimensional electron gas (2DEG).

At zero magnetic field, the free particle energy spectrum is

$$E(k_x, k_y) = \frac{\hbar^2}{2m^*}\left(k_x^2 + k_y^2\right) \tag{2.3}$$

where $m^* = 0.067m_e$ is the electron effective mass in GaAs. The number of electron states per unit area is

$$n(E) = \frac{m^* E}{\pi\hbar^2} \tag{2.4}$$

which yields a density of states

$$\rho(E) = \frac{dn(E)}{dE} = \frac{m^*}{\pi\hbar^2} \tag{2.5}$$

that is a constant. As a consequence, the Fermi energy is simply $E_F = n_s/\rho$. The Fermi wavenumber k_F and Fermi wavelength λ_F are

$$k_F = \sqrt{\frac{2m^* E_F}{\hbar^2}} = \sqrt{2\pi n_s}$$
$$\lambda_F = \frac{2\pi}{k_F} = \sqrt{\frac{2\pi}{n_s}} \tag{2.6}$$

λ_F is typically 40 nm in this system. Another relevant length scale for the two-dimensional electron gas is the mean free path

$$l = v_F \tau \tag{2.7}$$

where $v_F = \hbar k_F / m^*$ is the Fermi velocity and $\tau = m^* \mu / e$ is the elastic scattering time. The electron mobility μ is typically as high as 10^4-10^6 cm^2/Vs resulting in a mean free path, at low temperature, on the order of 1-10 μm. Ref. [10] provides a thorough review of the electronic properties of two-dimensional systems.

2.3 Quantum Point Contacts

The two-dimensional electron gas can be further confined into a one-dimensional system by using the standard split-gate technique [11,12]. Electron beam lithography can be used to pattern metallic gates on the surface of the heterostructure. When a negative voltage is applied to the metallic gate, the electron gas underneath is depleted. Using two surface gates, as shown in Figure 2.2, a narrow channel can be defined with a width *W* and length L. This device is called a quantum point contact (QPC) and is similar to the extensively studied metallic point contacts [13,14]. The main difference is that in this semiconductor system, W and L are both comparable to the Fermi wavelength and much less than the mean free path. Figure 2.2 (a) is a simulation of the potential profile created by the two surface gates, showing the resultant saddle point potential. Because W, L are

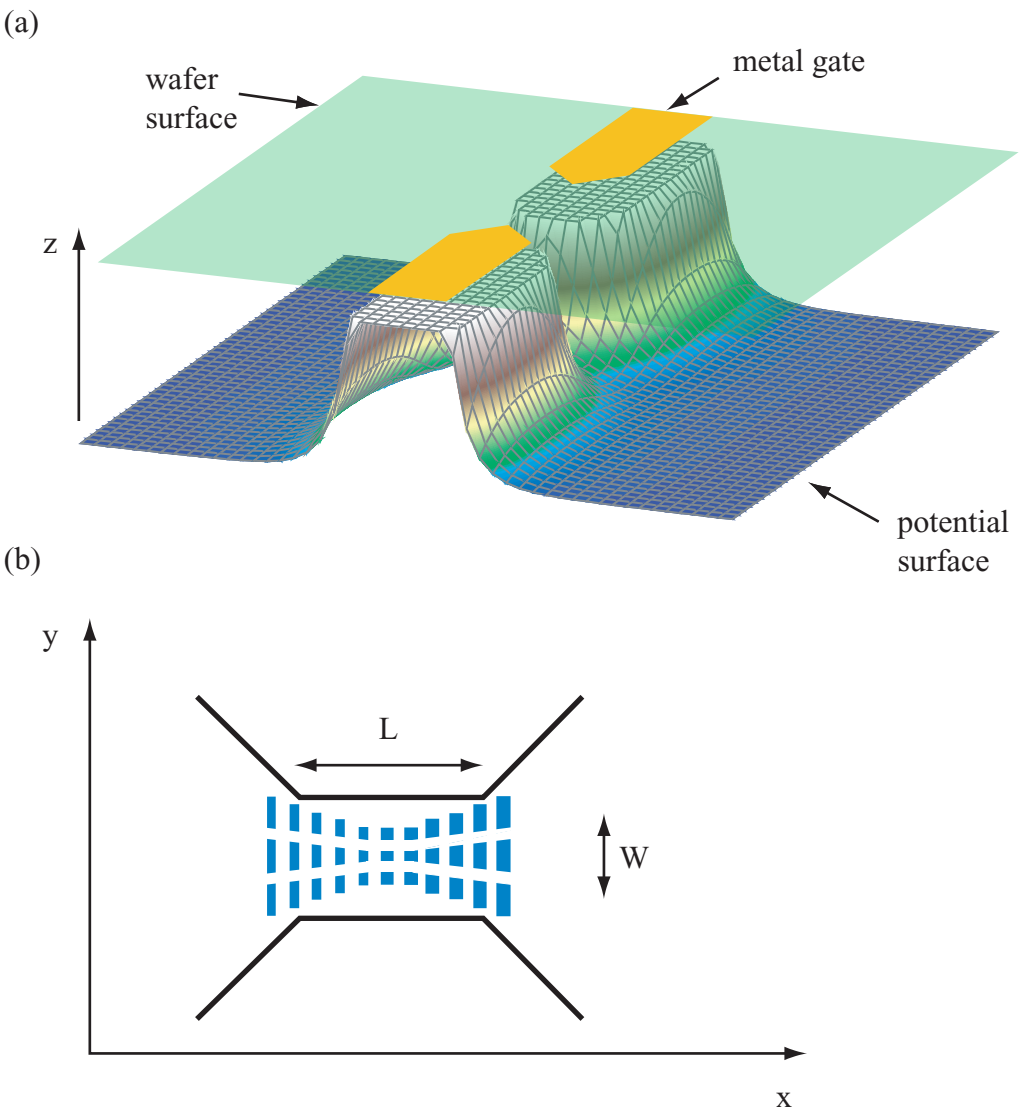

Figure 2.2 (a) Simulation of the resulting potential profile of the two-dimensional electron gas when a negative voltage is applied to the surface metal gates forming a quantum point contact. (b) Schematic diagram of a quantum point contact, with three modes. The width W is comparable to the Fermi wavelength λ_F. As the width is decreased, the number of modes flowing through the quantum point contact can be tuned down to zero.

both less than the mean free path, the channel is effectively one-dimensional, with an energy spectrum given by

$$E_n(k_x) = E_n + \frac{\hbar^2 k_x^2}{2m^*} \tag{2.8}$$

Transport through the QPC is ballistic and occurs through quantized one-dimensional subbands. Each transverse mode that flows through the channel contributes a factor of $2e^2/h$ to the conductance G of the QPC. Therefore, the total QPC conductance is given by [15-17]

$$G = \frac{2e^2}{h}\sum_i T_i \tag{2.9}$$

where T_i is the transmission probability of the i^{th} subband.

The first observation of quantized conductance in a QPC was made in 1988 [18,19]. For a review, see Refs. [20] and [21]. A scanning electron micrograph of a QPC is shown in Figure 2.3 along with the measured conductance. This measurement was performed at 125 mK. Each gate has a width of approximately 100 nm with the distance between the two gates being 200 nm. As the voltage on the gates is made more negative, the channel width is decreased and quantized conductance in units of $2e^2/h$ is clearly observed.

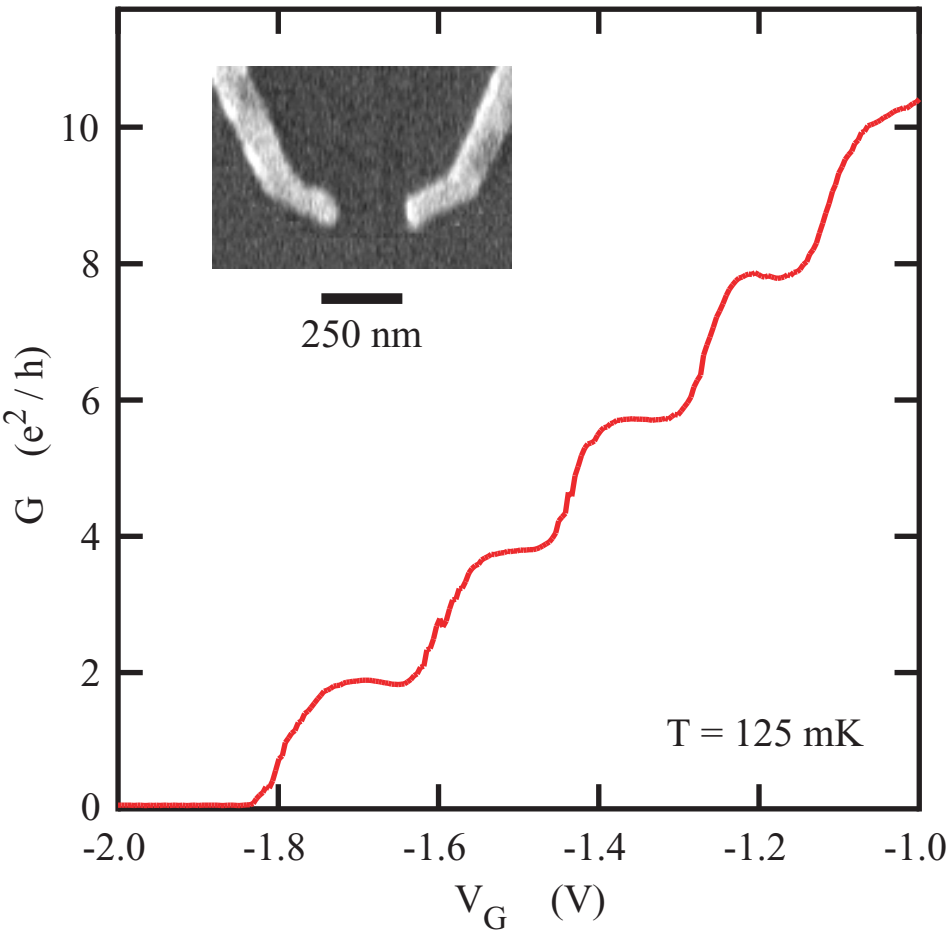

Figure 2.3 Quantum point contact conductance G as a function of side gate voltage V_G, measured at T = 125 mK. Clear conductance quantization is observed in multiples of $2e^2/h$. At $V_G < -1.8$ V, the quantum point contact begins to be pinched off. As V_G is increased, the width of the quantum point contact is increased continuously, allowing just an integer number of one-dimensional subbands to be occupied, resulting in the plateau structure. When $V_G > -1.0$ V, the width of the quantum point contact becomes large and the conductance resumes ohmic (linear) behavior. *Inset*: Scanning electron micrograph of a quantum point contact fabricated on a GaAs/$Al_{0.3}Ga_{0.7}$As heterostructure containing a two-dimensional electron gas 57 nm below the surface.

2.4 Quantum Dots and Coulomb Blockade

An electron must be provided with a charging energy of $e^2/2C$ if it is to be added to a conductor with total capacitance C. The capacitance is proportional to the size of the conductor, and as the size of the conductor decreases, the charging energy increases. For a small conducting island with a small capacitance, this charging energy can become quite large, leading to suppression in current, known as the Coulomb blockade effect. Nanofabrication techniques has allowed for the realization of small, artificially created, nanostructures with small capacitances ($C \sim 10^{-18}$ F). The Coulomb blockade was first observed in the I-V characteristics of small metal grains [22,23]. This effect was then used to explain single-electron charging in semiconductor devices [24]. An external side gate can be used as a way of tuning the dot through the Coulomb blockade [25], just as in a field-effect transistor.

A two-dimensional electron gas is ideal for creating small conducting islands of arbitrary geometry to investigate electron transport in the Coulomb blockade regime. A small region can be defined in the 2DEG by placing two quantum point contacts in series (with additional confinement gates), as shown in Figure 2.4. This zero-dimensional nanostructure, possessing a discrete energy spectrum, is called a quantum dot. Electrons are confined in all three dimensions due to electrostatic depletion from the patterned gates in the x-y plane and the strong electrostatic confinement to the quantum well in the z-direction. Figure 2.4 (a) shows a simulation of the quantum dot potential for a typical gate geometry. The tunnel barriers coupling the quantum dot to the large 2DEG reservoirs are defined by quantum point contacts. Therefore, the width and height of the barriers can be easily tuned by simply changing the voltage applied to the gates. This

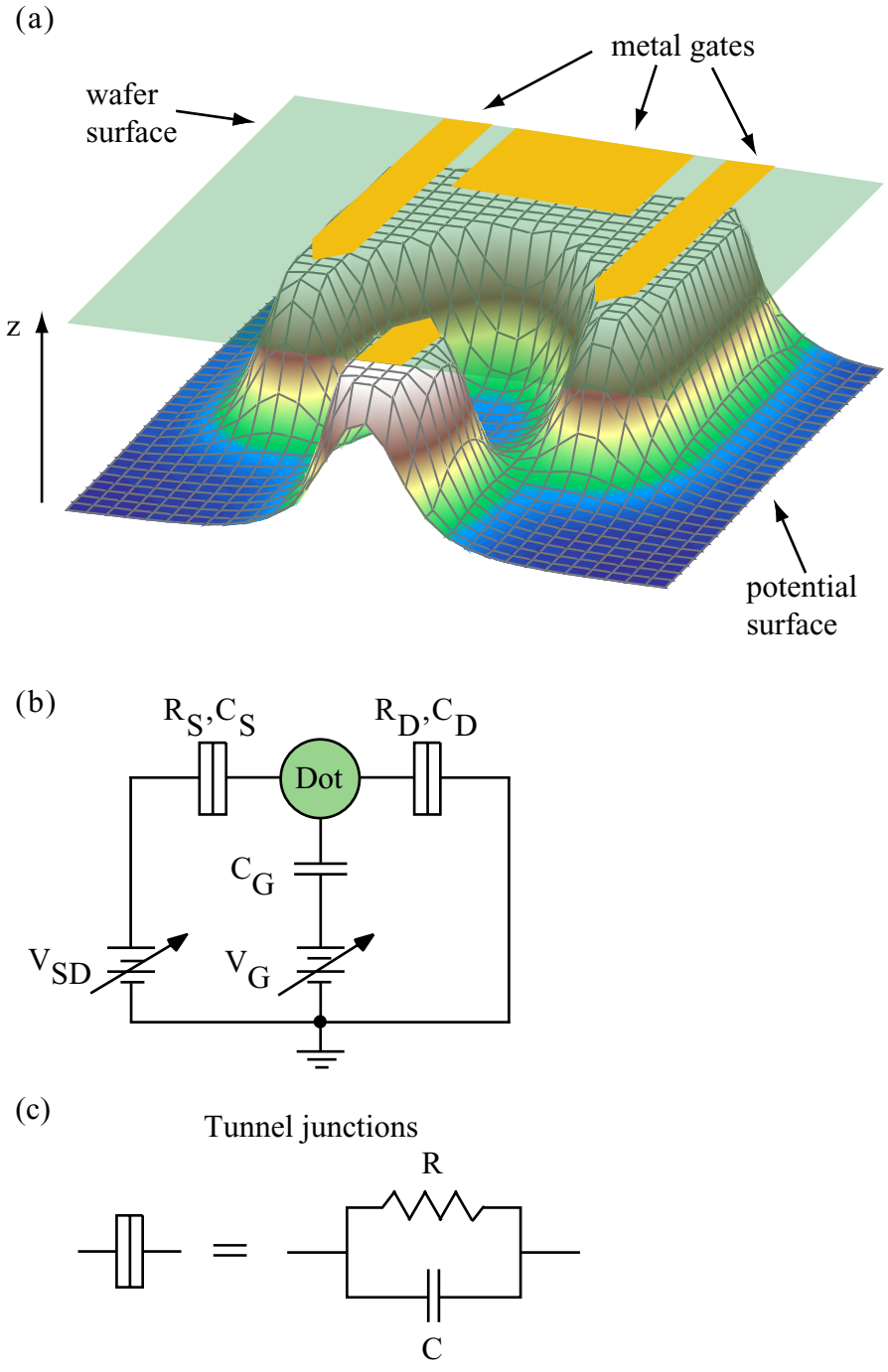

Figure 2.4 (a) Simulation of the resulting potential profile of the two-dimensional electron gas when a negative voltage is applied to the surface metal gates forming a quantum dot. Electrons are confined in all three dimensions to the small center region. Two tunable tunnel barriers are formed using quantum point contacts. (b) Circuit diagram of a quantum dot. The dot is connected to the source and drain by tunnel junctions, represented as split boxes. The gate is capacitively coupled to the dot. (c) The tunnel junctions are modeled as a parallel combination of a resistor and a capacitor. Tunnel junctions permit transfer of charge between the dot and the leads.

flexibility is what makes semiconductor quantum dots a well-controlled system.

Figure 2.4 (b) shows a circuit diagram modeling a quantum dot as a small conducting island coupled to its environment through two tunnel junctions and a capacitively coupled side gate with variable voltage. A small source-drain voltage V_{SD} is applied across the dot. The tunnel junctions are modeled as "leaky" capacitors (parallel arrangement of a capacitor and resistor). There are two basic requirements that need to be satisfied to observe the Coulomb blockade. The first is that the charging energy must be much larger than the thermal energy k_BT:

$$\frac{e^2}{2C_\Sigma} \gg k_B T \tag{2.10}$$

This ensures that electrons will not be able to tunnel from the contact leads to the conducting island due to their thermal energy. The total capacitance of the system C_Σ includes the gate capacitance, the two tunnel junction capacitances, and any stray capacitance in the system. That is, C_Σ is the capacitance between the conducting island and the rest of the world. The other requirement is that the charge on the island needs to be a well-defined integer (charge quantization). This can be related to a minimum resistance for the tunnel junctions by using the RC time constant for the circuit in Figure 2.4 (b) and the energy uncertainty relation:

$$\Delta E \Delta t > h \rightarrow \frac{e^2}{C_\Sigma} RC_\Sigma > h \rightarrow R \gg \frac{h}{e^2} \sim 25.8k\Omega \tag{2.11}$$

where $\Delta t = RC_\Sigma$ is used as the time required to charge or discharge the island. In the laboratory, we satisfy these two conditions by making the conductor small, working at low temperatures, and by weakly coupling it to the junctions.

We can analyze the circuit in Figure 2.4 (b) using a simple approach [26] where we assume that the Coulomb interactions between the electrons are parameterized by a constant capacitance. Let the total charge on the conducting island equal -N*e*, where N is an integer. In general, for a circuit with n conductors, the total charge Q_i of the i^{th} conductor can be written in terms of its electrostatic potential V_i as

$$Q_i = \sum_{j=1}^{n} C_{ij} V_j \tag{2.12}$$

where the coefficient C_{ij} is the capacitance matrix. The electrostatic energy can be written as a sum over all n conductors:

$$U = \frac{1}{2}\sum_{i=1}^{n} Q_i V_i = \frac{1}{2}\sum_{i=1}^{n}\sum_{j=1}^{n} V_i C_{ij} V_j = \frac{1}{2}\sum_{i=1}^{n}\sum_{j=1}^{n} Q_i C_{ij}^{-1} Q_j \tag{2.13}$$

It is important to emphasize that the charge in Equation (2.12) is a polarization charge and does not have to be quantized in units of electron charge.

Let

$$\Phi = \sum_i \frac{C_i V_i - Ne}{C_\Sigma} \tag{2.14}$$

be the potential on the dot (with i summing over any capacitance present in the system). The total electrostatic energy of the dot with N electrons is

$$U = \frac{1}{2}\sum_i C_i (V_i - \Phi)^2 - \sum_i C_i V_i (V_i - \Phi) \tag{2.15}$$

Equation (2.15) is the total energy stored in the capacitors minus the work done by the external voltage sources. Substituting Equation (2.14) into (2.15), summing only over the side gate voltage source (assume $V_{SD} = 0$), and taking only the terms dependent on N, we have

$$U(N) = \frac{(C_G V_G - Ne)^2}{2C_\Sigma} \tag{2.16}$$

which represents the difference in energy of the induced and actual charge in a capacitor, C_Σ.

Equation (2.16) assumes a continuous energy spectrum for the quantum dot. However, because of confinement, electrons in the dot occupy quantized energy levels with a finite level spacing. Assuming that the discrete energy spectrum is independent of the number of electrons in the dot, we can simply modify Equation (2.16) to include the energy of the occupied single particle states E_i [27]:

$$U(N) = \frac{(C_G V_G - Ne)^2}{2C_\Sigma} + \sum_{i=1}^{N} E_i \tag{2.17}$$

The electrochemical potential of the quantum dot is, by definition [28],

$$\mu_{dot}(N) = U(N) - U(N-1) = \frac{e^2}{C_\Sigma}(N - \frac{1}{2}) - e\frac{C_G}{C_\Sigma}V_G + E_N \tag{2.18}$$

The charging energy, which is the addition energy that is required to add a single electron to the quantum dot, is given as the difference in the electrochemical potential of the N + 1 electron dot and the N electron dot:

$$E_C \equiv \mu_{dot}(N+1) - \mu_{dot}(N) = \frac{e^2}{C_\Sigma} + E_{N+1} - E_N \tag{2.19}$$

It is this energy, which can become very large for very small total capacitance, that is the source of the Coulomb blockade.

In GaAs quantum dots, E_C can range from several milli-electron volts for small dots in the few-electron regime to a few hundred micro-electron volts, if the dot is large and contains several hundred electrons. For large dots, we can replace the $E_{N+1} - E_N$ term

in Equation (2.19) with a mean level spacing δE that is inversely proportional to the dot area A_{dot}. The number of electrons N on a dot can be approximated as $N = n_s A_{dot}$, and because the density of states is a constant, we find $\delta E = 2E_F / N$. The factor of 2 comes from the spin degeneracy of the states. For E_F = 15 meV and N = 500 electrons, δE ~ 0.06 meV.

By shifting the bottom of the conduction band of the quantum dot using the external side gate, we can lift the Coulomb blockade and add or remove just a single electron, resulting in a conductance peak. The spacing between the peaks ΔV_G can be determined from equating the electrochemical potential of the two charge states:

$$\begin{aligned} \mu_{dot}(N+1, V_G + \Delta V_G) &= \mu_{dot}(N, V_G) \\ \rightarrow \Delta V_G &= \frac{C_\Sigma}{eC_G}\left(\frac{e^2}{C_\Sigma} + E_{N+1} - E_N\right) \end{aligned} \tag{2.20}$$

Ignoring the effects of the discrete energy spectrum ($\delta E \rightarrow 0$), Equation (2.20) simplifies to

$$\Delta V_G = \frac{e}{C_G} = \frac{E_C}{\alpha e} \tag{2.21}$$

where the ratio of gate capacitance to total capacitance $\alpha = C_G/C_\Sigma$ is the "capacitive lever arm" that converts the change in side gate voltage to the change in the quantum dot energy. We see that the conductance peaks are periodic in V_G. If a finite energy level spacing δE is included, the conductance peaks are, in general, not periodic.

Figure 2.5 provides a simple graphical interpretation of the analysis presented above. Figure 2.5 (a) shows the difference between the induced charge and the actual charge on the quantum dot as a function of the side gate voltage. The dot can only contain an integer number of electrons. Consequently, as V_G is varied, the total charge on the dot

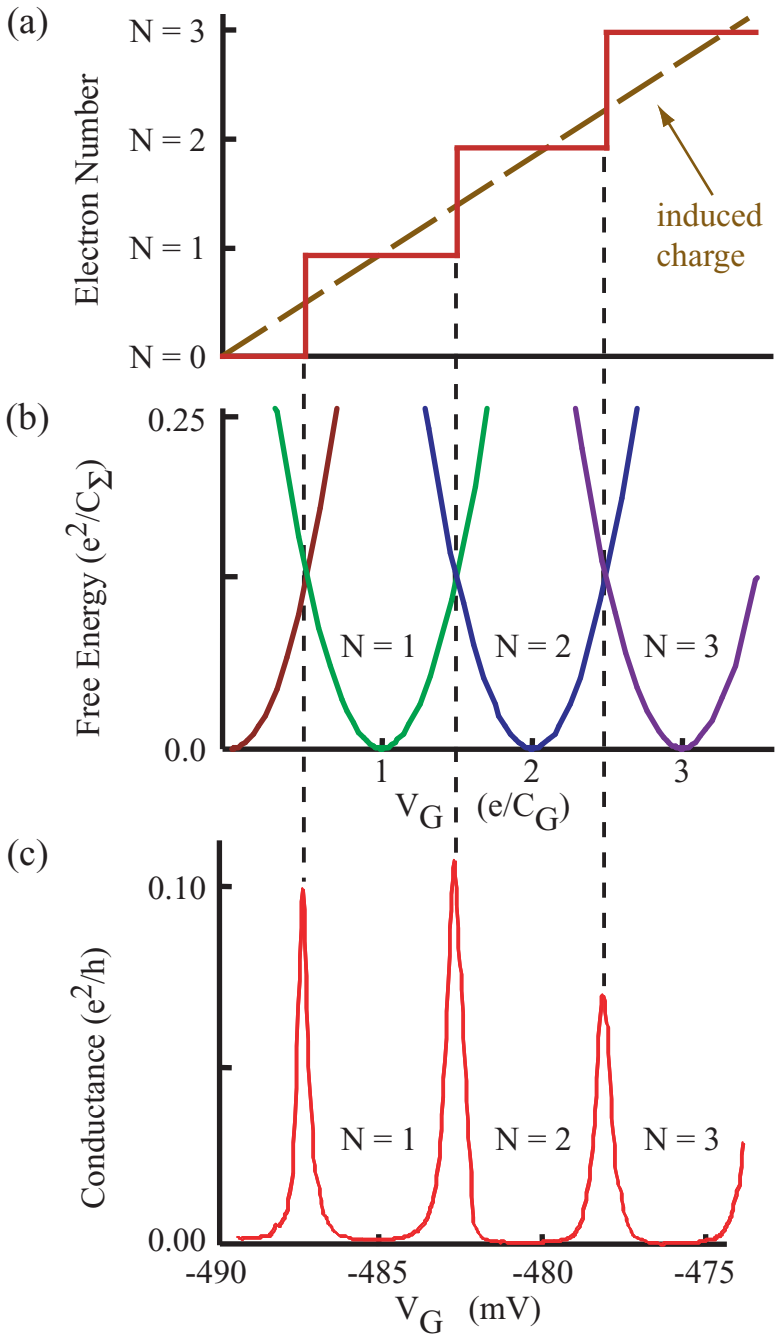

Figure 2.5 (a) Charge as a function of gate voltage V_G in a quantum dot. The actual charge state of a quantum dot is quantized, and increases in a step-wise manner with V_G. Normally, for a large conductor, the quantization of charge can be ignored and the charge induced by the capacitively coupled side gate displays a smooth, linear increase. (b) Free energy as a function of side gate voltage. Each charge state (difference between the actual and induced charge) results in a different energy parabola. It is energetically favorable for the number of electrons on the dot to change by one only at the points where these parabolas intersect. (c) Measured conductance oscillations as a function of the side gate voltage. A peak in conductance (non-zero current) is observed only when two dot charge states are degenerate in energy, and electrons tunnel on and off the dot.

increases in steps, as opposed to a linear increase in charge that is expected to occur due to the induced charge of $C_G V_G$. Figure 2.5 (b) is a plot of the electrostatic energy, given by Equation (2.16), for different values of N, also as a function of the side gate voltage. Each charge state of the dot yields a parabola with a minimum defining a stable region. Within these stable regions, the charge on the quantum dot does not change, and the dot is in the Coulomb blockade regime. When V_G is tuned to a position where two different parabolas intersect, these two charge states are degenerate in energy, and therefore the charge of the quantum dot fluctuates between N*e* and (N + 1)*e*. Only when this condition is met [Equation (2.20)], can an electron tunnel on or off the dot, resulting in a non-zero conductance through the quantum dot. The actual measured conductance of a single quantum dot is shown in Figure 2.5 (c), clearly illustrating the Coulomb blockade peaks.

In the *classical* Coulomb blockade regime where the thermal energy $k_B T$ is larger than the level spacing, the Coulomb blockade conductance peak lineshape is given by

$$G(V_G) = G_0 \cosh^{-2}\left(\frac{eC_G(V_G - V_{G0})}{2.5C_\Sigma k_B T}\right) \tag{2.22}$$

Here, G_0 is the peak height, and V_{G0} is the location of the peak. In the *quantum* Coulomb blockade regime, where the level spacing is larger than the thermal energy, and transport occurs only through a single state, the conductance peak lineshape is given by

$$G(V_G) = G_0 \cosh^{-2}\left(\frac{eC_G(V_G - V_{G0})}{2.0C_\Sigma k_B T}\right) \tag{2.23}$$

Up to now, we have only discussed the linear response regime. When a finite voltage bias V_{SD} is applied across the dot, it opens up a transport window of eV_{SD} for tunneling through the quantum dot. The complete energy profile of the quantum dot is shown in Figure 2.6 (a). The dot is coupled to two electron reservoirs, the source and

drain, by two tunnel barriers. The Coulomb blockade can be lifted either by changing the bottom of the conduction band with V_G or by applying a source-drain voltage V_{SD}. The voltage bias changes the electrochemical potential in the leads, such that if the Fermi level in the source is larger than the Coulomb blockade gap, electrons can tunnel into the dot. If V_{SD} is further increased, electrons may tunnel through excited states.

We can incorporate a source-drain voltage to the capacitive charging model discussed above as follows [29]. Let the voltage bias V_{SD} be applied on the left lead (source) of the dot, with the tunnel junction capacitance C_S. For zero source-drain voltage we assumed C_S was a capacitance to ground (a stray capacitance) that was included in C_Σ. Now, we must include the work done by the source-drain voltage, $C_S V_{SD}$, in the sum of Equation (2.15). The electrostatic energy is therefore

$$U(N) = \frac{\left(C_G V_G + C_S V_{SD} - Ne\right)^2}{2C_\Sigma} \tag{2.24}$$

Electrons can tunnel on or off the dot at either the source or the drain, giving four different tunneling events. For any tunneling event to occur, the energy difference between the initial state and the final state must be less than zero. This gives four inequalities

$$\begin{aligned} N + \frac{1}{2} > \frac{C_G V_G}{e} - \frac{(C_\Sigma - C_S)V_{SD}}{e} > N - \frac{1}{2} \\ N + \frac{1}{2} > \frac{C_G V_G}{e} + \frac{C_S V_{SD}}{e} > N - \frac{1}{2} \end{aligned} \tag{2.25}$$

which map out diamond regions in V_{SD}-V_G space where the conductance is zero (tunneling is blocked) and the dot is in the Coulomb blockade. These regions, shown in Figure 2.6 (b) are known as the Coulomb blockade diamonds. The diamond shapes arise because of the capacitive coupling between the lead capacitance C_L and the dot. The

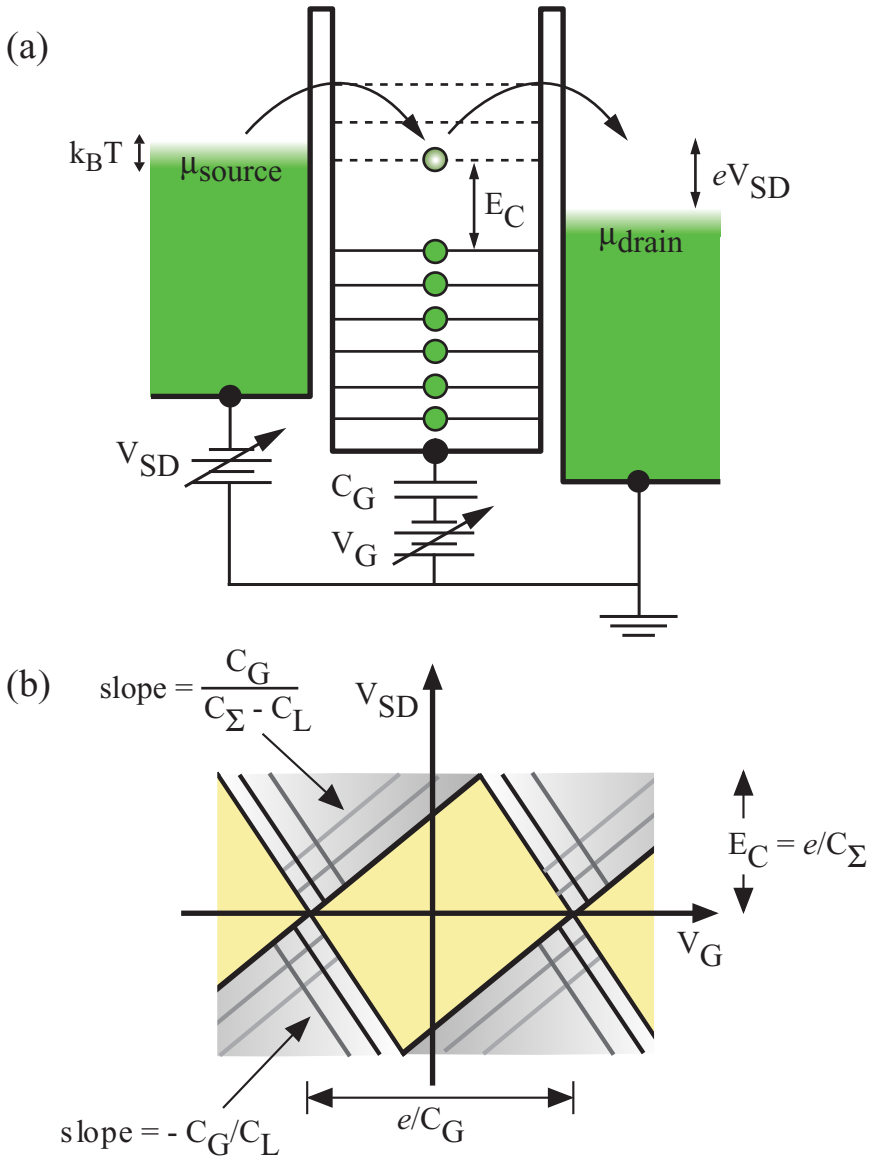

Figure 2.6 (a) Energy profile of a quantum dot. The quantum dot has a discrete energy spectrum, with electrons filling up the discrete levels up to $\mu_{dot}(N)$. The charging energy is given as $E_C = \mu_{dot}(N+1) - \mu_{dot}(N)$. Two tunnel barriers separate the quantum dot from the electron reservoirs. The Coulomb blockade can be lifted either by raising μ_{source} relative to μ_{drain} using a voltage bias V_{SD} applied across the dot or by raising the bottom of the dot conduction band using the side gate voltage V_G. (b) A measurement of the conductance as a function of both V_{SD} and V_G results in Coulomb blockade diamonds, periodic in V_G. The boundaries of the diamonds are defined by four inequalities (see text) and can be used as a measure of the dot parameters. Inside the diamond region, conductance is zero due to Coulomb blockade. As V_{SD} is increased, electrons can begin tunneling through the dot via discrete energy levels, giving rise to conductance peaks running parallel to the diamond edges.

diamond dimensions reveal several key device parameters, including the charging energy and gate capacitance. Furthermore, the excited states will give rise to conductance peaks running parallel to the diamond edges. Plots of the Coulomb diamonds can be thought of either as the addition spectrum of a quantum dot, because each diamond corresponds to an additional electron added to the dot, or the excitation spectrum, because the discrete level spectrum can be directly measured from the location of the conductance peaks.

Figure 2.7 (a) shows a finite bias Coulomb blockade measurement of a single quantum dot in the few-electron regime taken at 60 mK. Details of the fabrication process and measurement techniques are described in Chapter 3. The differential conductance dI/dV_{SD} is plotted as a function of the side gate voltage V_G and the source drain voltage V_{SD}. For large dots, one normally finds adjacent Coulomb diamonds of identical dimensions. Here, because the dot contains just a few electrons, the constant interaction model assumed above fails and Coulomb interactions cannot be simply parameterized. In fact, the area of each Coulomb blockade diamond is directly proportional to the energy of the corresponding charge state, and differences in the diamond areas observed in Figure 2.7 (a) is indicative of a shell structure for the quantum dot. Figure 2.7 (b) is the differential conductance of the same dot when tuned to the one-electron regime. The large charging energy is an indication of the small size of the dot and the absence of diamonds for more negative side gate voltage or large source-drain voltage confirms that the dot contains either zero or one electron. Excited states can clearly be seen as conductance peaks parallel to the diamond edges.

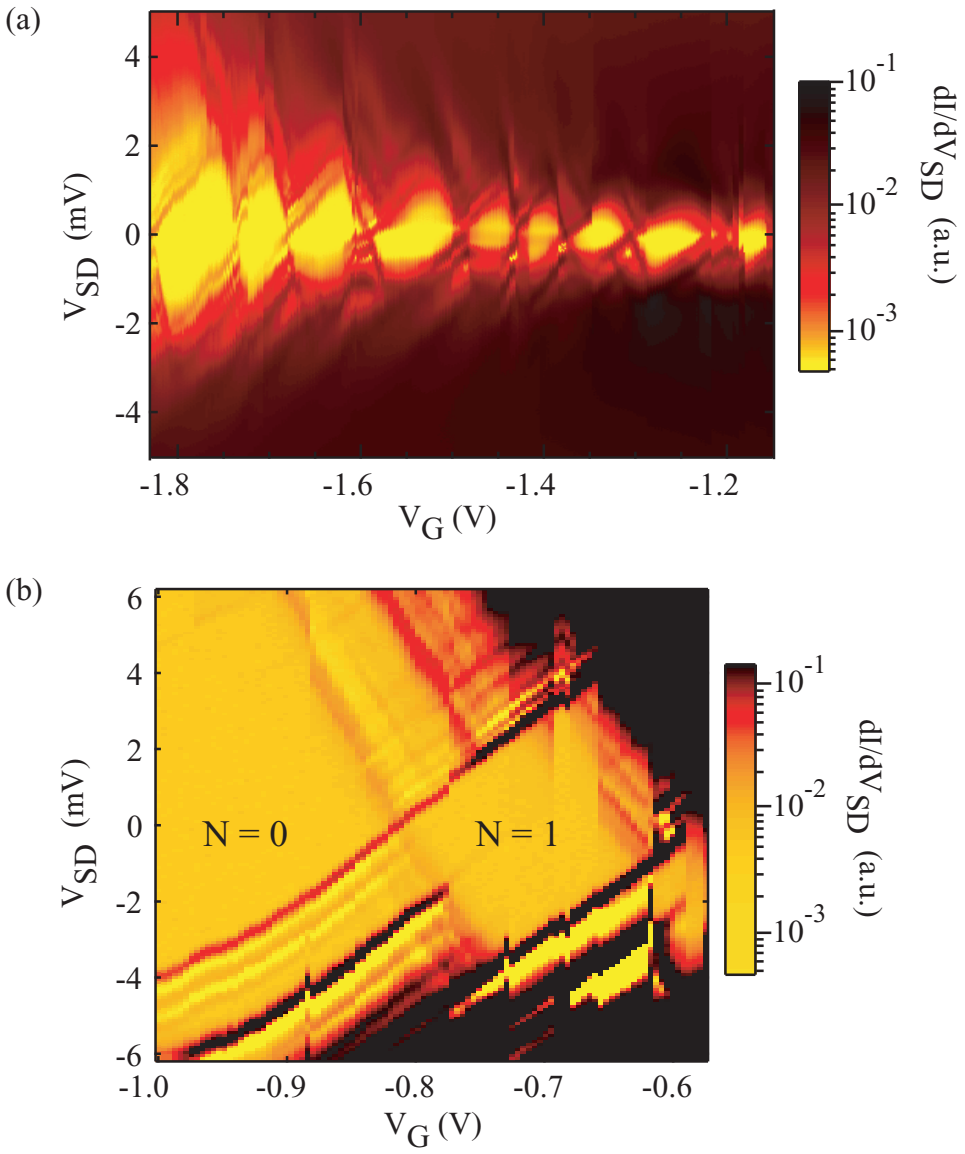

Figure 2.7 (a) Differential conductance of a few-electron quantum dot as a function of its side gate voltage and the source-drain bias, measured at T = 60 mK. (b) Differential conductance of the same dot as in (a) when tuned to the one-electron regime. Clear excited state features are observed.

2.5 Double Quantum Dots

We can investigate the coupling between quantum dots by forming an artificial molecule consisting of two quantum dots tunnel-coupled to each other, as shown in Figure 2.8 (a). Figure 2.8 (b) shows the circuit equivalent of the double quantum dot artificial molecule. This is a simple generalization of the circuit diagram of a single quantum dot to that of a double dot with two independent side gates and an inter-dot tunnel junction parameterized by a capacitance C_{12}. The side gate voltages are V_{G1} and V_{G2}. Dot 1 has a total capacitance C_1 and dot 2 has total capacitance C_2. We can analyze this device as we did for the single dot, calculating the electrostatic energy using Equation (2.13). This model is a classical capacitive circuit model and does *not* include effects of inter-dot tunneling [30]. It is assumed that the electrons are localized on one dot at a time, with the charge on each dot being an integer number. Following the derivation presented in Ref. [31], we sum over all the capacitors present in the system and obtain, for $V_{SD} = 0$,

$$U(N_1, N_2) = \frac{1}{2}E_{C1}N_1^2 + \frac{1}{2}E_{C2}N_2^2 + N_1N_2E_{C12} + f(V_{G1},\ V_{G2}) \tag{2.26}$$

where

$$E_{C1} = \frac{e^2}{C_1}\left(\frac{1}{1-\frac{C_{12}^2}{C_1C_2}}\right), E_{C2} = \frac{e^2}{C_2}\left(\frac{1}{1-\frac{C_{12}^2}{C_1C_2}}\right), E_{C12} = \frac{e^2}{C_{12}}\left(\frac{1}{\frac{C_1C_2}{C_{12}^2}-1}\right), \tag{2.27}$$

and

$$\begin{aligned} f(V_{G1},V_{G2}) &= \frac{1}{2e^2}\left(C_{G1}^2V_{G1}^2E_{C1} + C_{G2}^2V_{G2}^2E_{C2}\right) + \frac{1}{e^2}(C_{G1}V_{G1}C_{G2}V_{G2}E_{C12}) \\ &-\frac{1}{e}C_{G1}V_{G1}(N_1E_{C1} + N_2E_{C12}) - \frac{1}{e}C_{G2}V_{G2}(N_1E_{C12} + N_2E_{C2}) \end{aligned} \tag{2.28}$$

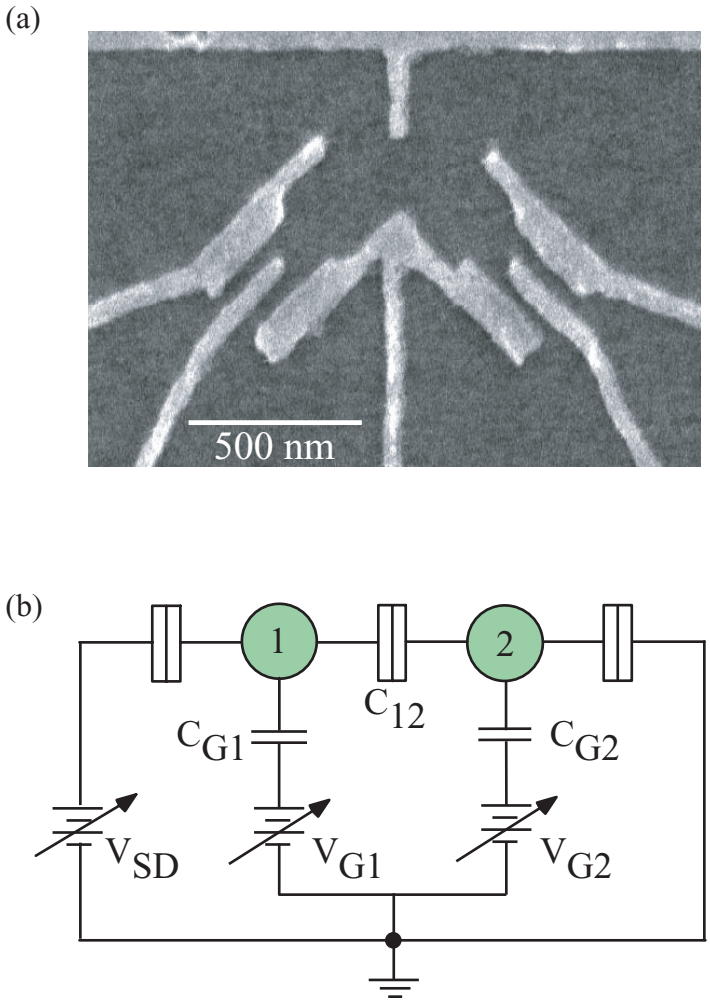

Figure 2.8 (a) Scanning electron micrograph of a few-electron double quantum dot fabricated on a GaAs/$Al_{0.3}Ga_{0.7}As$ heterostructure containing a two-dimensional electron gas 52 nm below the surface. (b) Circuit diagram of a double quantum dot. The dots are coupled together by a tunnel junction, parameterized by a capacitance C_{12}.

If the two dots are identical, with $C_1 = C_2 = C_\Sigma$, Equation (2.26) simplifies to [30]

$$U(N_1,N_2)=\frac{1}{2C_\Sigma(1-\alpha^2)}\Big[\big(C_{G1}V_{G1}-N_1e\big)^2+\big(C_{G2}V_{G2}-N_2e\big)^2 + 2\alpha\big(C_{G1}V_{G1}-N_1e\big)\big(C_{G2}V_{G2}-N_2e\big)\Big] \tag{2.29}$$

where $\alpha = C_{12}/C_\Sigma$. The electrostatic energy of the double quantum dot defines a set of paraboloids in V_{G1}-V_{G2} space where, similar to the single dot case, the minima represent points of charge stability, i.e., a stable configuration of N_1 electrons on dot 1 and N_2 electrons on dot 2. Only at the intersections of these paraboloids, will electrons tunnel through the double dot to yield a current. At these intersections, the Coulomb blockade is lifted and the measured conductance is non-zero.

Figures 2.9 and 2.10 show schematics of the conductance versus the two side gate voltages V_{G1} and V_{G2} for different coupling regimes. These plots are called stability diagrams because in the regions where the Coulomb blockade stops electron transport, the double dot is in a well-defined (stable) charge state given by (N_1,N_2). For two independent dots, $\alpha = 0$ and the stability diagram is just a series of squares with non-zero conductance only at the intersections, as shown in Figure 2.9 (a). These are basically a series of Coulomb blockade peaks for each dot acting independently. For such decoupled dots, the side gate voltage of, say, dot 1 changes the charge of dot 1 only, without affecting the charge on dot 2. If inter-dot coupling is very strong, the double dot becomes just one large composite dot. In this configuration, both side gates couple to the single large dot with total charge $N_T = N_1 + N_2$. Each of the two gates couples to this large composite dot, and can tune the charge state N_T. The stability diagram, shown in Figure 2.9 (b), is therefore just a series of diagonal Coulomb blockade peaks.

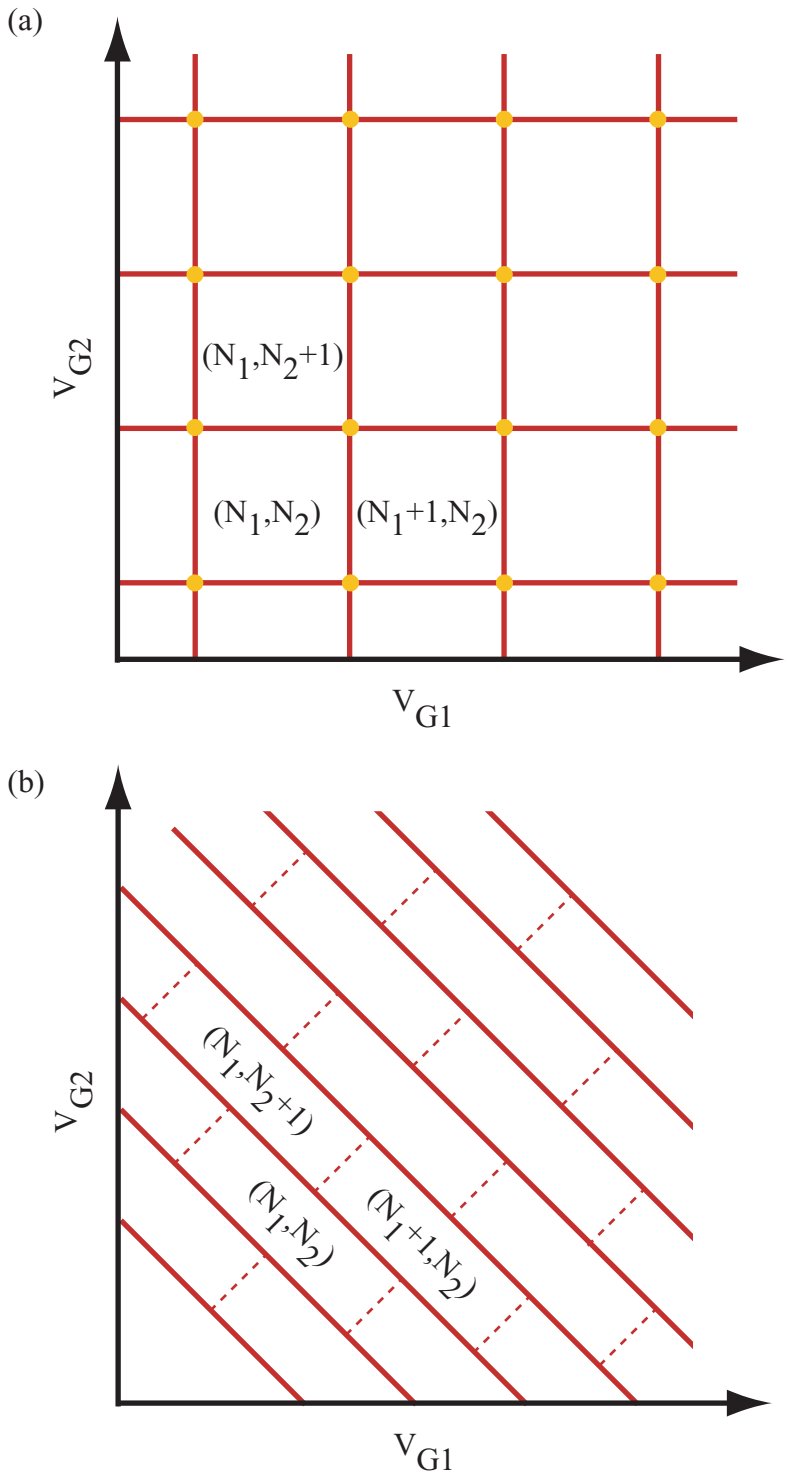

Figure 2.9 Stability diagrams of a double quantum dot showing the boundaries of the stable states. (a) When the coupling C_{12} is zero, the stability diagram is given by a series of squares where the intersections correspond to a conductance peak. (b) When coupling is strong, the double dot becomes one large dot and both side gates couple to the single dot equally, results in a series of diagonal Coulomb blockade peaks.

The regime of finite inter-dot tunneling cannot be described by the electrostatic model discussed above. When tunnel-coupling is allowed, the assumption of charge being quantized in each dot is not applicable. Inter-dot tunnel-coupling removes the excess energy of the system that would otherwise arise from frustrated polarized configurations of the double dot if each dot would be forced to maintain an integer number of electrons. It is the inter-dot tunneling, and not the inter-dot capacitive coupling, that is the dominant effect.

In Figure 2.10, the tunnel-coupled double dot stability diagram is shown. We also plot a one-dimensional slice along $V_{G1} = V_{G2}$ which helps to demonstrate the effect of the tunneling. For the charge configuration of (0,0) and (1,1), the energy surface is given by the two parabolas, as derived above, that intersect at a single point with a higher parabola corresponding to the more energetic polarized charge states (0,1) and (1,0). For two dots that are not coupled, a single conductance peak is observed at this intersection. When tunneling is introduced, electrons are shared between the two dots which lower the ground state energy of the polarized charge states, shown by the red curve. There now exist two intersections, and the single conductance peak is split into two peaks. The peak splitting forms a honeycomb pattern in the stability diagram. The peaks correspond to "triple points" where the three distinct charge configurations are degenerate in energy.

In tunnel-coupled double dots, electrons are shared between the two dots and form an analog of a covalent bond, with a binding energy $E_{int} = Fe^2/4C_\Sigma$. Here, $F = 2\Delta V_S/ \Delta V_P$ is the fractional peak splitting, as defined in Figure 2.10. This was first shown experimentally by Livermore *et al.* [30]. Theoretical calculations were performed by Golden and Halperin [32,33] and Matveev *et al.* [34,35].

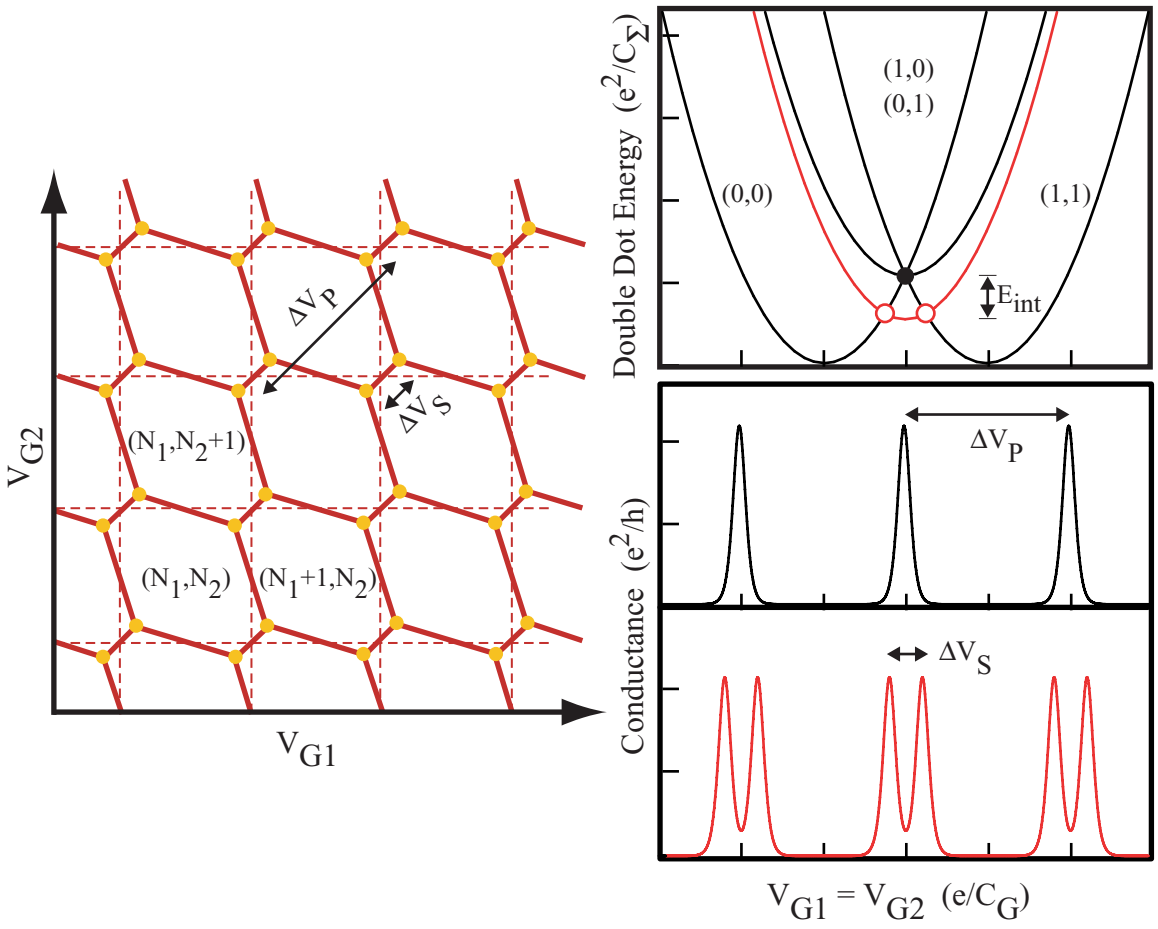

Figure 2.10 When inter-dot tunneling is included, the original vertices of the stability diagram in Figure 2.9 (a) split into two peaks, resulting in a honeycomb stability pattern. The right panel shows a slice at $V_{G1} = V_{G2}$ for the first unit cell. Tunneling lowers the energy of the polarized (1,0) and (0,1) states (red curve) by an amount E_{int}, resulting in a splitting of the conductance peaks.

Figure 2.11 shows the measured stability diagrams of a few-electron double quantum dot device that we fabricated and measured [36]. From finite-bias Coulomb blockade measurements of each dot independently (for example, see Figure 2.7), we are able to confirm that these quantum dots are indeed few-electron quantum dots. We can couple the two quantum dots to form a double dot and measure the stability diagram for weak and strong coupling. Tunnel-coupled few-electron quantum dots can serve as spin qubits for quantum information processing, as proposed by Loss and DiVincenzo [37].

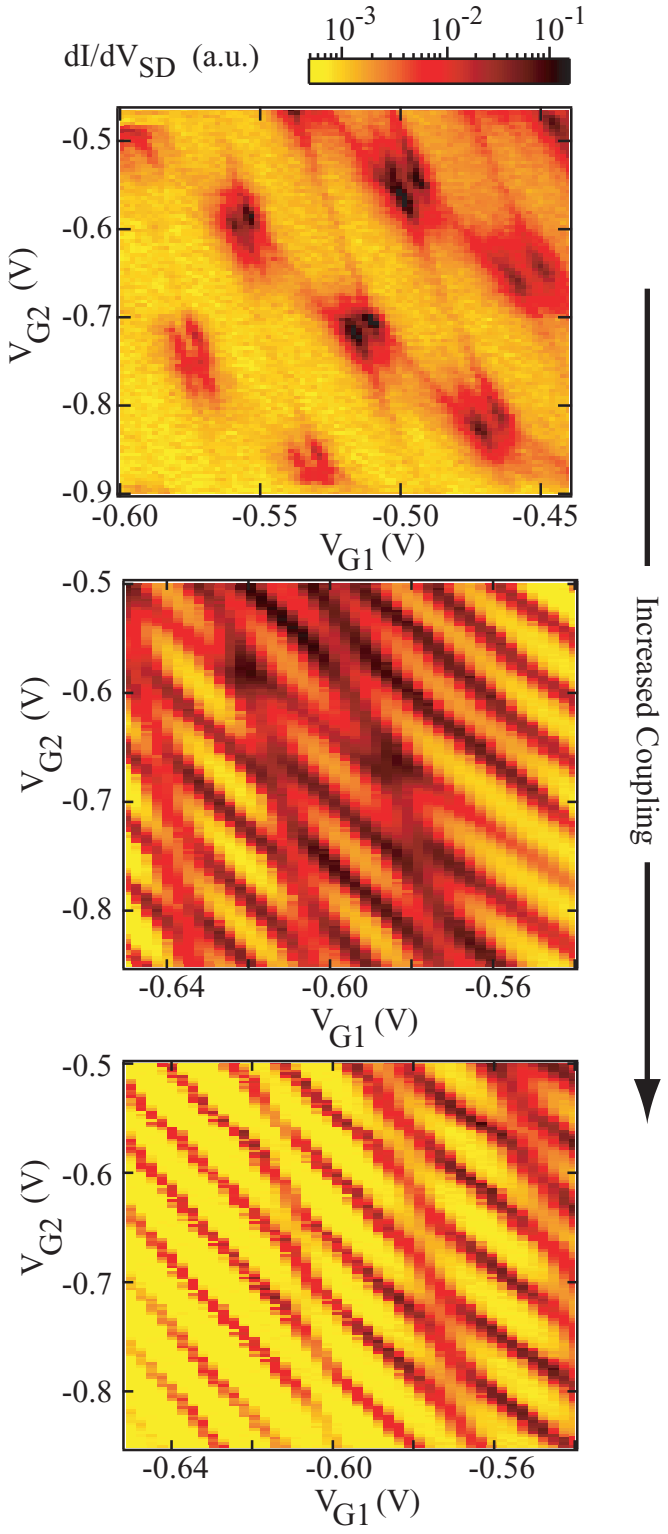

Figure 2.11 Measured stability diagrams of the few-electron double quantum dot shown in Figure 2.8 (a). Three different regimes, from weak to strong coupling, is observed, corresponding to the schematics shown in Figures 2.9 and 2.10. Measurements were performed at T = 60 mK.

III

EXPERIMENTAL METHODS

3.1 Overview

The experiments presented in this thesis require successful fabrication of nanoscale devices and a thorough understanding of low-noise electronic measurement techniques and cryogenic techniques. This chapter covers the experimental considerations and methods necessary to conduct low-temperature transport measurements. The major focus is on techniques related to the GaAs/AlGaAs system. Fabrication and experimental methods related to the Ge/Si nanowire systems are described in Chapter 6 and Chapter 7.

Section 3.2 begins with a description of the GaAs/AlGaAs heterostructures from which split-gate devices are made, followed by an overview of the fabrication and lithography process. Section 3.3 describes the low-temperature systems used to cool down the devices. The electronic measurement circuits are described in Section 3.4, where the procedure on operating the superconducting solenoid to generate a magnetic field is also included. Finally, in Section 3.5, Shubnikov-de Haas measurements of the two-dimensional electron gas are presented.

3.2 GaAs/AlGaAs Split-Gate Device Fabrication

Molecular beam epitaxy [6,7] is the method of choice for growing heterostructures due to the highly detailed control available over the growth parameters. High quality structures in terms of purity, interface sharpness and crystalline perfection can be grown. The GaAs/AlGaAs heterostructures used in this thesis were grown by

Micah Hanson from the Gossard group at the University of California, Santa Barbara. Figure 3.1 shows a schematic of a typical molecular beam epitaxy ultra high vacuum chamber. Several sources, called Knudsen effusion-cells or K-cells, are circularly positioned around the sample holder. The temperature of each K-cell can be independently set and regulates the resulting flux of each element. To avoid any non-uniformity due to the different positions and tilts of the K-cells, the sample is rotated during growth. The substrate is also heated during growth so that defects can be overcome through annealing. Typically, the wafer is grown on a semi-insulating GaAs substrate with a [100] crystal orientation. If a back gate is desired, an n-doped substrate is used. A 100 nm GaAs buffer layer followed by a 20 period 2.5 nm $Al_{0.3}Ga_{0.7}As$ / 2.5 nm GaAs superlattice is deposited to provide an atomically smooth surface. This eliminates any effects from defects that may be present in the substrate. A 1000 nm GaAs layer is then deposited to further separate the heterojunction where the 2DEG will form from the substrate. A layer of $Al_{0.3}Ga_{0.7}As$ follows, interrupted by a monolayer of Si atoms (donors). The Si atoms are intentionally spaced away from the heterojunction to reduce ionized-impurity scattering. This is known as modulation doping [5], and allows for high electron mobility. Finally, a thin 5 nm GaAs cap layer is deposited to prevent the aluminum in $Al_{0.3}Ga_{0.7}As$ from oxidizing. A typical wafer profile is shown in Figure 3.2.

When selecting a wafer, typical parameters to consider are the carrier sheet density n_s, mobility μ, and the distance of the 2DEG below the surface.
There is a tradeoff between higher mobility and minimum feature size defined by electrostatic surface gates. Higher mobility samples require a larger $Al_{0.3}Ga_{0.7}As$ spacer layer and, in general, a deeper 2DEG. However, as the 2DEG is made deeper, the

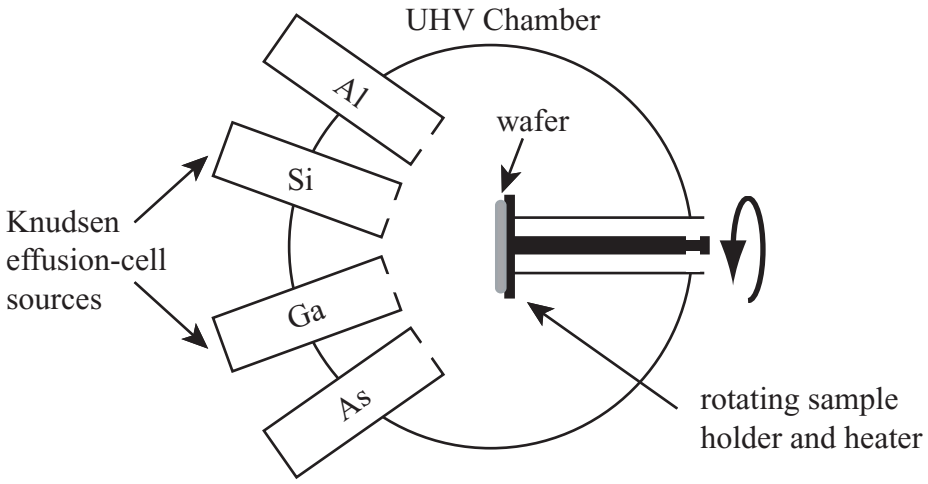

Figure 3.1 Schematic diagram of a molecular beam epitaxy ultra high vacuum (UHV) chamber. Each Knudsen effusion-cell contains an element that is needed to grow or dope the heterostructure. The wafer is heated and rotated during growth.

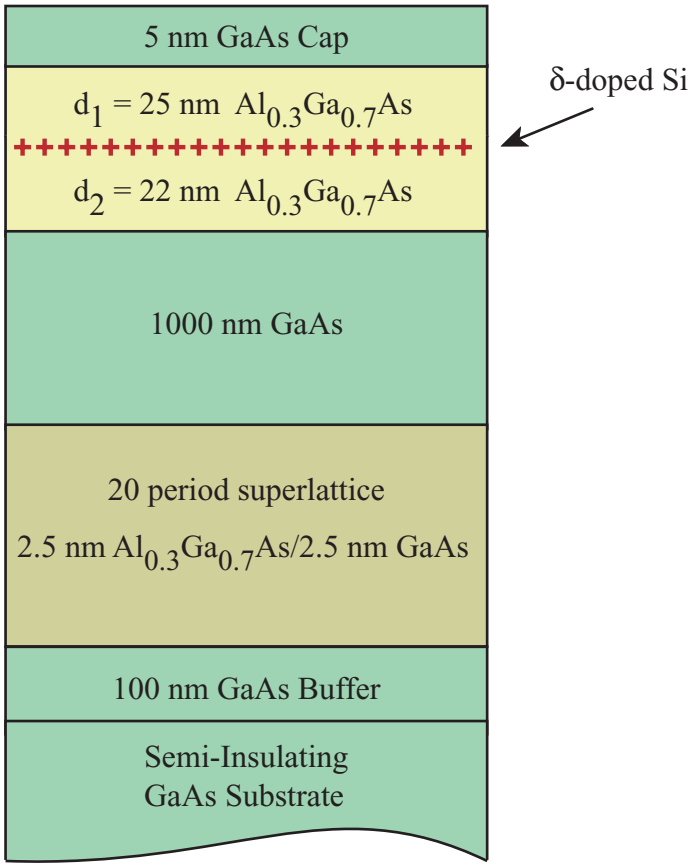

Figure 3.2 Wafer profile of a GaAs/AlGaAs heterostructure (wafer number 020227B-MH2) used in this thesis. For wafer 020227C-MH3, d_1 = 30 nm and d_2 = 22 nm.

resolution one can achieve with surface gates gets worst. Preference is given to shallower 2DEGs because of interest in smaller quantum dots in the few-electron regime, where mobility is not of concern.

The following steps are taken in order to successfully fabricate split-gate devices starting from the unprocessed wafer grown at Santa Barbara:

(1) Cleave the wafer

Fabrication starts with cleaving small chips, approximately 2 mm by 3 mm in size, out of the 3 inch GaAs/AlGaAs wafers. The wafer is cleaved, by hand, with a diamond scribe and a ruler covered with Teflon tape. The wafer is first cleaved into 4 quarters, and then into 3 mm strips. The 3 mm strips are further cleaved into 2 mm by 3 mm chips.

(2) Clean the chips

Cleaning is performed in three steps. First, the chips are placed in hot trichloroethylene for 15 minutes in order to remove any grease or oil on the chip surface. Then, the chips are sonicated for 15 minutes in acetone to dislodge any dirt or particles stuck to the surface. Finally, the chips are sonicated in methanol for 10 minutes to remove any residue left by acetone. Once the chips are removed from methanol, they are blow-dried with ultra-pure nitrogen gas.

(3) Spin on PMMA

In order to prepare the samples for electron beam lithography, the chips are coated with a positive e-beam resist called polymethylmethacrylate (PMMA). Depending on the feature size and the thickness of the metal to be evaporated, one, two, or three layers of PMMA is used. One layer is generally not used because of possible defects the may arise in the PMMA layer. However, if extremely small features are desired, one layer of PMMA can

be used. Two layers of PMMA provide the best option in terms of high resolution and low probability of defects. If a thick metal layer is desired, for example, when making bonding pads and contacts, three PMMA layers are spun on the chip. After each PMMA layer is spun, the chip is placed on a hotplate set to 180°C. In order to allow for an undercut, which facilitates the process of lift-off after metallization, two different solutions of PMMA are used: 2% 950 K (950 kDa) PMMA in anisole by weight and 2% 495 K (495 kDa) PMMA in anisole by weight.

(4) Electron Beam Lithography

Once the chip has a PMMA coating, it is ready to be patterned using electron-beam lithography. The electron beam severs the bonds in the PMMA macromolecule allowing the smaller molecules that are formed to be removed by a chemical developer at a later stage. The electron microscope used was a JEOL 6400 scanning electron microscope controlled by the Nabity Pattern Generation System.

(5) PMMA Developing

To develop the exposed areas of the PMMA, the chips are first rinsed with isopropyl alcohol, then placed in a chemical developer for one minute, and again rinsed with isopropyl alcohol. The chemical developer is a solution consisting of 375 ml isopropyl alcohol, 125 ml methyl-isobutyl ketone, and 6.5 ml methyl-ethyl ketone. Finally, the chips are blow-dried with ultra-pure nitrogen gas.

(6a) Metallization

A thermal evaporator is used to deposit the metal gates or ohmic contacts. Below is a table showing the usual layers used for metallization.

For metal gates:

Layer	Metal	Thickness
1	Chrome (Cr)	5 nm
2	Gold (Au)	20 nm

For ohmic contacts:

Layer	Metal	Thickness
1	Nickel (Ni)	5 nm
2	Gold (Au)	20 nm
3	Germanium (Ge)	25 nm
4	Gold (Au)	10 nm
5	Nickel (Ni)	5 nm
6	Gold (Au)	40 nm

(6b) Etching

If a trench is desired instead of a metal gate, either the home-built ion miller (dry etch) or a quick chemical procedure (wet etch) can be used to etch out the patterns made with electron beam lithography. An etch permanently removes the patterned region of the 2DEG. The ion miller uses an argon plasma, and mills the heterostructure at a rate of approximately 1 nm/s. The advantage of using an argon plasma is that the argon ions do not dope the GaAs heterostructure. Using a focused ion beam of Ga^+ ions tends to embed Ga in the heterostructure and destroys the sample. It is usually sufficient to mill as deep as the Si doped layer, and not any deeper, to remove the 2DEG.

If resolution is not of concern, it is quicker to use a chemical etch. The procedure for the wet etch is as follows:

1. Place a beaker with 10 ml citrus feed stock (Citric Acid:Water in 1:1 by weight) on a hotplate set to 50°C. This is the etch solution.
2. Dip the sample in H_2O (Beaker 1)

3. Dip the sample for 5 seconds in 1:5 $HCl:H_2O$
4. Dip the sample for 5 seconds in 1:5 $NH_4OH:H_2O$
5. Dip the sample in H_2O (Beaker 1)
6. Dip the sample in the etch solution. Etch rate is 2 nm/s for AlGaAs and 10 nm/s for GaAs
7. Dip the sample in H_2O (Beaker 2)
8. Dip the sample in H_2O (Beaker 3). Only at this point does the etch stop.

It is generally required to cover any chip that was etched with PMMA so that the aluminum in the now exposed AlGaAs layer does not oxidize.

(7) Lift-Off

To lift off the PMMA, the chips are placed in acetone for several hours. Ultrasounding the chips in acetone is not recommended because it tends to lift-off metal even from the desired metallization locations.

Figure 3.3 shows the lithography process from spinning until lift-off.

(8) Annealing

If ohmic contacts were deposited, an annealing step is required to allow the metal to diffuse through the wafer and make contact with the 2DEG. The annealing steps are:

Step	Duration	Temperature	Purpose
1	1 minute	110°C	Drive off moisture
2	10 seconds	260°C	Prime the sample
3	20 seconds	410°C	Anneal the sample

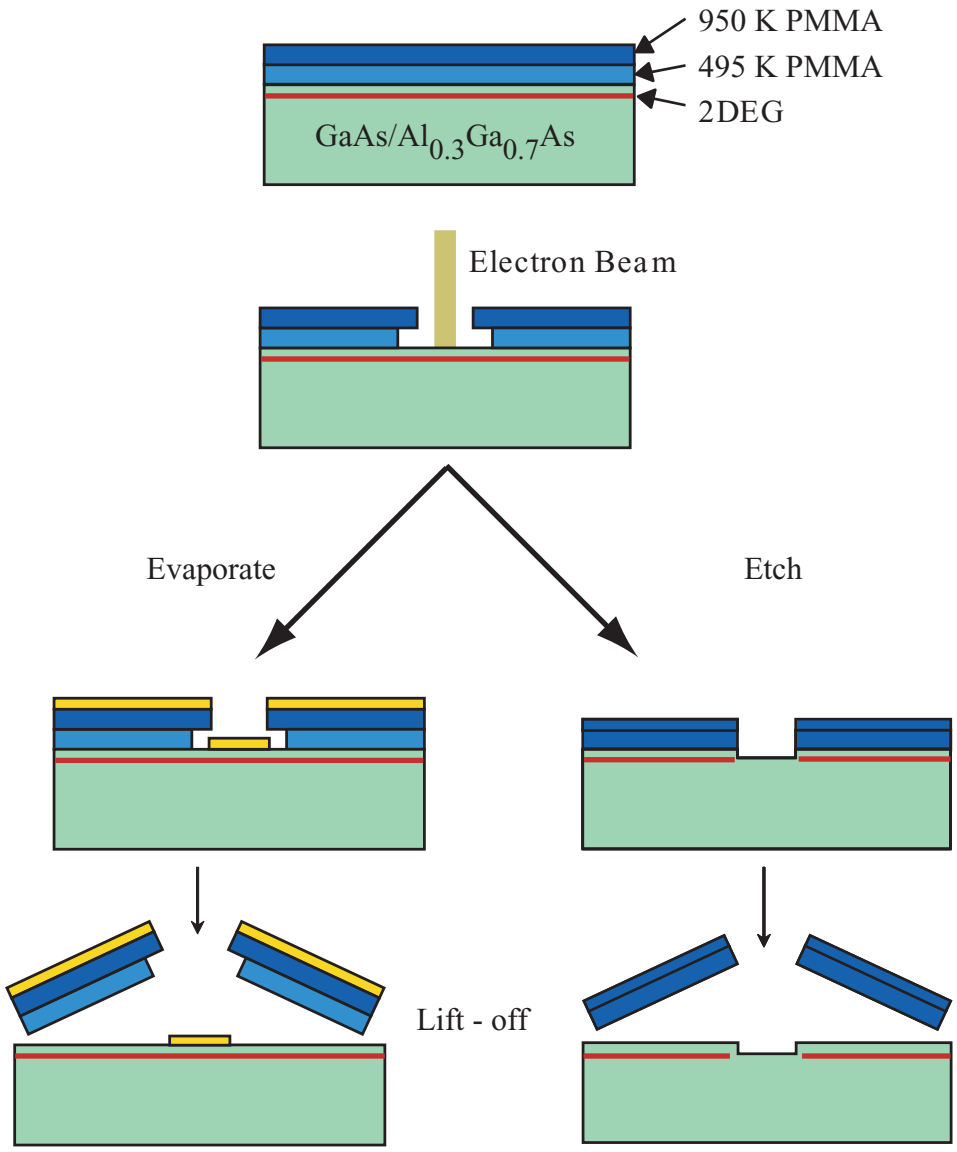

Figure 3.3 The electron-beam lithography process begins by spinning on two layers of 950 K PMMA and 495 K PMMA. After being exposed to an electron beam, the sample is developed, and the area that was exposed to the electron beam is washed away. At this point, the sample is ready for metallization or for etching. An undercut is formed due to the lower molecular weight of the PMMA in the lower layer. When etching, no undercut is needed, and two layers of 950 K PMMA can be used. After lift-off, the sample is left with either a surface metal gate or a trench in the area that was exposed to the electron-beam.

Ohmic contacts are fabricated before any other metal gates are deposited because of this annealing step. Once the contacts are annealed, the fabrication process is repeated starting at step (2) above.

(9) Packaging

The last step in the fabrication process is packaging the chip. This includes placing the chip on a chip carrier and wirebonding the contacts. The cryosystems are equipped with PLCC (ceramic) sockets (AMP Corp., Part # 641444-2), that take the 28 pin JEDEC-standard PLCC chip carriers (Jade Corp., Part # 28M270-J-060-U-06-4). These are non-magnetic carriers. The sample is glued on the chip carrier with GE varnish, and then placed in an oven at 100°C overnight. Gold wire is then used to wirebond all the gates and contacts.

Figure 3.4 shows a photograph of a complete, packaged device. Further details concerning device fabrication can be found in Ref. [38].

3.3 Cryogenic Systems

The constraint of $k_B T \ll E$ needs to be met in order to be able to investigate charge and spin effects in the semiconductor quantum dots and nanowires studied in this thesis. Here, E is some relevant energy scale such as the charging energy E_C for a quantum dot (see Chapter 2) or the Josephson energy E_J for a S-N-S junction (see Chapter 7). Therefore, we are required to perform experiments at low temperatures. Starting at room temperature (300 K), we can work our way down to low temperatures using liquid nitrogen (77 K), liquid helium (4.2 K), evaporatively-cooled helium (~ 1.4 K), ^{3}He systems (~ 300 mK) and ^{3}He/^{4}He dilution refrigerators (~ 30 mK).

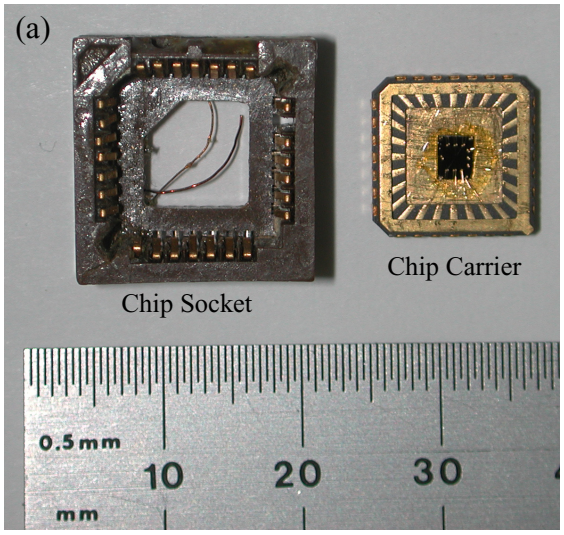

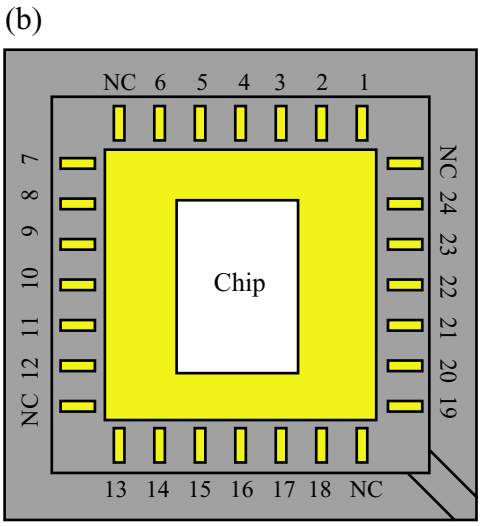

Figure 3.4 (a) Photograph of the ceramic chip socket and a sample mounted on a chip carrier. (b) Schematic showing the 28-pin PLCC chip carrier and the pin numbering employed in all of the cryostats. Only 24 of the 28 pins are connected, leaving 4 pins that are not connected (NC).

3.3.1 4.2 K Insert

For a quick test of the samples, 4.2 K suffices, and this can be easily achieved by dipping the sample into a Helium storage dewar. If a magnetic field is required, for example, when performing Hall measurements (Section 3.5), the dewar for the ^{3}He system can be used. A new 4.2 K insert was built because older inserts were not reliable and had broken electrical leads and several shorts. The 4.2 K insert is one of the most useful pieces of equipment in the laboratory. Therefore, details regarding the construction of the 4.2 K insert are provided below. Furthermore, because the 4.2 K insert is rather simple, compared to the dilution refrigerator insert, we can use this opportunity to analyze the heat conduction of this simple insert to gain a better understanding of heat conduction in more complicated systems. It should be noted that the ^{3}He insert is very similar in design to the 4.2 K insert described below, with the major difference being the diameter of the insert: the ^{3}He insert needs to be especially thin so that in can be placed inside the vacuum insert for ^{3}He operation.

Figure 3.5 shows the 4.2 K insert design. This insert is placed inside a stainless steel tube (not shown in the figure) and then placed into the dewar. It is important to minimize the heat flow, both in the form of conduction and radiation, that occurs through the insert from the outside environment into the cryostat. For this insert, thermal conduction can take place in the inner tube, the electrical wires and the outer tube. Therefore, the insert is made of a long, thin stainless steel rod with manganin wires (Lake Shore Cryotronics, Inc., Part # MW-36) running from the top connector box all the way down to 1 kΩ resistors at the bottom of the insert. At the top of the insert there is a 24 pin

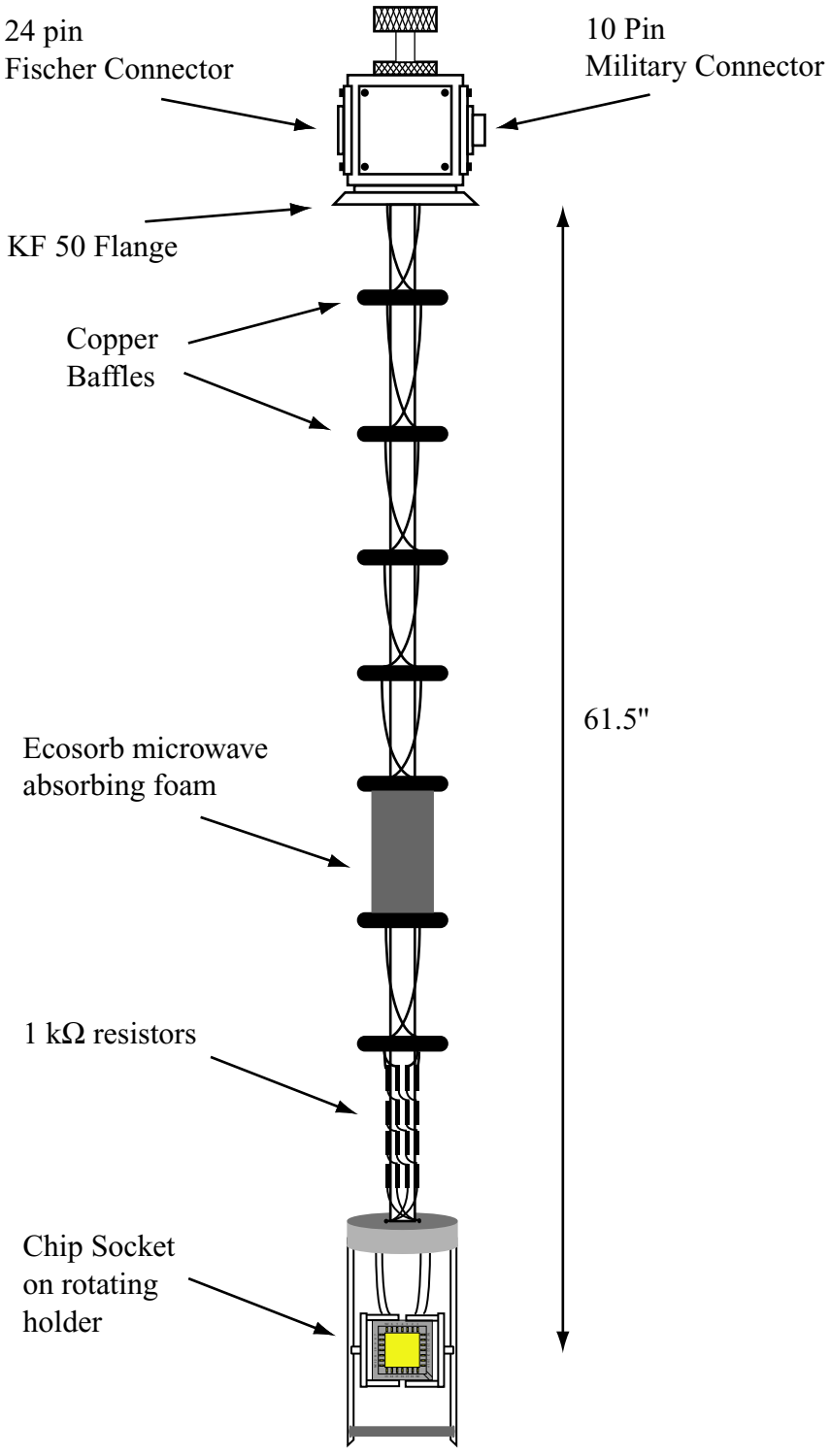

Figure 3.5 Schematic of the 4.2 K insert. The top of the insert has both a 10-pin military connector and a 24-pin Fischer connector. Manganin wires from the top connectors are twisted along the insert, and are soldered onto 1kΩ resistors at the bottom of the insert. Phosphor bronze wires are used from the resistors down to the sample. The chip socket is mounted on a holder that can be rotated. Copper baffles and microwave frequency radiation-absorbing foam are placed along the insert.

Fischer connector and a 10 pin military connector. These connectors are hermetically sealed. The 1 kΩ resistors at the bottom of the insert, together with the capacitance of the wires, behave like low pass filters, and therefore reduce the high frequency noise traveling down the wires. After the 1 kΩ resistors, phosphor bronze wires (Lake Shore Cryotronics, Inc., Part # QL-36) were used to connect to the chip socket. This is the same chip socket used in the ^{3}He insert and the ^{3}He/^{4}He dilution refrigerators and allows samples to be easily tested on the 4.2 K insert and later moved to the other systems. The chip socket sits between two holders that can rotate 90 degrees, allowing for the sample to be aligned in either a parallel or perpendicular position relative to the magnetic field. The 10 wires from the military connector are provided for any additional features that one may need, such as an LED, a thermometer, or a Hall probe.

Thermal radiation occurs down the inter-tube spacing by blackbody radiation. From the Stephan-Boltzmann Law, the rate of radiation $\dot{Q}$ is

$$\dot{Q} = \sigma A T^4 \tag{3.1}$$

where A is the cross sectional area, T is the temperature, and $\sigma = 5.67 \times 10^{-8} W/m^2 K^4$ is the Stefan-Boltzmann constant. Blackbody radiation from 300 K to 4 K is approximately 50 mW/cm^2. To minimize blackbody radiation, 7 copper baffles are evenly spaced along the rod. Moreover, Ecosorb microwave frequency radiation-absorbing foam is wrapped around the insert to further minimize thermal radiation. The baffles and foam help reduce the evaporation rate of the liquid helium inside the dewar by minimizing the amount of thermal radiation from the outside environment.

The rate of heat flow or, more appropriately, heat leak $\dot{Q}$, due to thermal conduction in the insert can be calculated from [39,40]

$$\dot{Q} = -G\bar{K}(T_2 - T_1) \tag{3.2}$$

where G is a factor depending on the shape of the thermal conductor and

$$\bar{K} = \frac{1}{T_2 - T_1}\int_{T_1}^{T_2} k(T)dT \tag{3.3}$$

Here, k(T) is the thermal conductivity. To determine G, we use the relation

$$\dot{Q} = -A(r)k(T)\nabla T \tag{3.4}$$

where A(r) is the cross sectional area and ∇T represents the temperature gradient. The insert and wires can be considered as long cylindrical conductors, placed along the z axis, with constant cross sections A and temperature gradient ∇T = dT/dz. Therefore, Equation (3.4) becomes

$$\int_{z_1}^{z_2} dz\frac{\dot{Q}}{A} = -\int_{T_1}^{T_2} k(T)dT \tag{3.5}$$

or, since $\dot{Q}$ and A are constant,

$$\dot{Q} = \frac{-A\int_{T_1}^{T_2} k(T)dT}{\int_{z_1}^{z_2} dz} = -(T_2 - T_1)\bar{K}\frac{A}{\int_{z_1}^{z_2} dz} = -(T_2 - T_1)\bar{K}\frac{A}{z_2 - z_1} \tag{3.6}$$

This gives us an expression for G in Equation (3.2).

The latent heat of liquid helium at 4.2 K is L = 2.7 kJ per liter. For an insert that is immersed in liquid helium, the heat leak $\dot{Q}$ that is generated by the insert boils off the liquid and does not warm up the resulting helium gas. This leads to a large helium boil-off rate because *cold* helium gas exits the dewar. The rate of evaporation is $\dot{Q}$/L or approximately 1.4 liters of liquid helium per hour for one watt. If there is (perfect) heat exchange between the insert and the helium gas, the gas that exits the dewar is already at

room temperature. For this situation, the rate of evaporation of liquid helium is $\dot{Q}$/(L+H), where the enthalpy H is the energy need to increase 1 liter of helium from 4.2 K to room temperature. This reduces the rate of evaporation to approximately 20 ml of liquid helium per hour for one watt.

For the 4.2 K insert, $\dot{Q}$ is the sum of the heat flow in the outer tube, the inner tube, and the 34 wires. We assume that the lengths of the tubes and wires are $z_2 - z_1 = 151$ cm and that $T_1 = 300$ K and $T_2 = 4$ K. Stainless steel has $\overline{K} = 0.10$ W/cm-K. The outer tube (outer radius R = 0.95 cm and an inner radius r = 0.90 cm) has an area $A = \pi(R^2 - r^2) = 0.30$ cm^2 and $\dot{Q}_{Outer} = 58$ mW. The inner tube (outer diameter of 0.95 cm and wall thickness of 0.5 mm) area is 0.14 cm^2 and $\dot{Q}_{Inner} = 28$ mW. For the manganin wires, we first need to determine $\overline{K}$. The manufacturer provides a table of the thermal conductivity of the manganin wire versus temperature, from which we can obtain k(T). Using Equation (3.3), we determine $\overline{K} = 0.157$ W/cm-K. The cross sectional area of the wire is A = 0.013 mm^2, and therefore, $\dot{Q}_{wire} = 0.04$ mW per wire, or $\dot{Q}_{wires} = 1.3$ mW for all 34 wires. The total heat leak of the insert is $\dot{Q}_{Total} = 87$ mW of heat flow from the outside environment to the liquid helium. It should be remembered that this is the maximum rate of heat transfer possible. We expect a lower value for $\dot{Q}_{Total}$ since the wires are wrapped around the metal insert and lose heat to it. Furthermore, heat is lost in the radial direction, through the walls of the tubes. The radial heat loss is proportional to the difference of the temperature outside the tube to the temperature inside the tube.

3.3.2 ^{3}He/^{4}He Dilution Refrigerators

The first suggestions of dilution refrigeration were made by H. London in 1951 [41]. A brief overview of the principle of dilution refrigeration follows. A more complete description can be found in the excellent text regarding dilution refrigerators and general low-temperature techniques by O.V. Lounasmaa [42].

To understand the underlying principle of dilution refrigeration, it is instructive to examine the phase diagram of ^{3}He/^{4}He mixtures, shown in Figure 3.6. Below the coexistence curve, two phases, one rich in ^{3}He and one rich in ^{4}He, exist. Due to its lower density, the ^{3}He-rich phase resides above the ^{4}He-rich phase. If the mixture is cooled below the coexistence curve, the concentration of ^{3}He in the ^{3}He-rich phase increases and the concentration of ^{4}He in the ^{4}He-rich phase increases. However, even at T = 0 K, the concentration of ^{3}He in the ^{4}He-rich phase is not zero.

Figure 3.7 shows a schematic of a dilution unit. Pumping on the ^{4}He-rich phase preferentially removes the ^{3}He, which has a higher vapor pressure than ^{4}He. In order for ^{3}He to cross the phase boundary from the ^{3}He-rich phase to the ^{4}He-rich phase and restore the equilibrium condition, energy, in the form of heat from the walls of the mixing chamber, is extracted. This acts to cool the sample, which is placed at the end of the cold finger that is in thermal contact with the mixing chamber. The ^{3}He that was lost to the ^{4}He-rich phase by this process is constantly replenished by the circulating flow of ^{3}He.

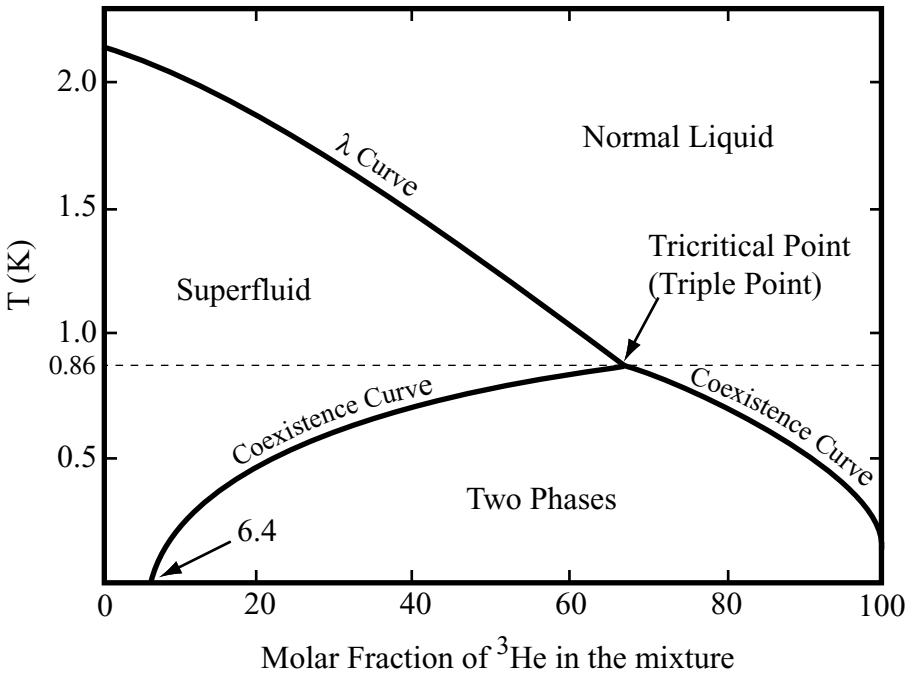

Figure 3.6 Phase diagram of $^3He/^4He$ mixture.

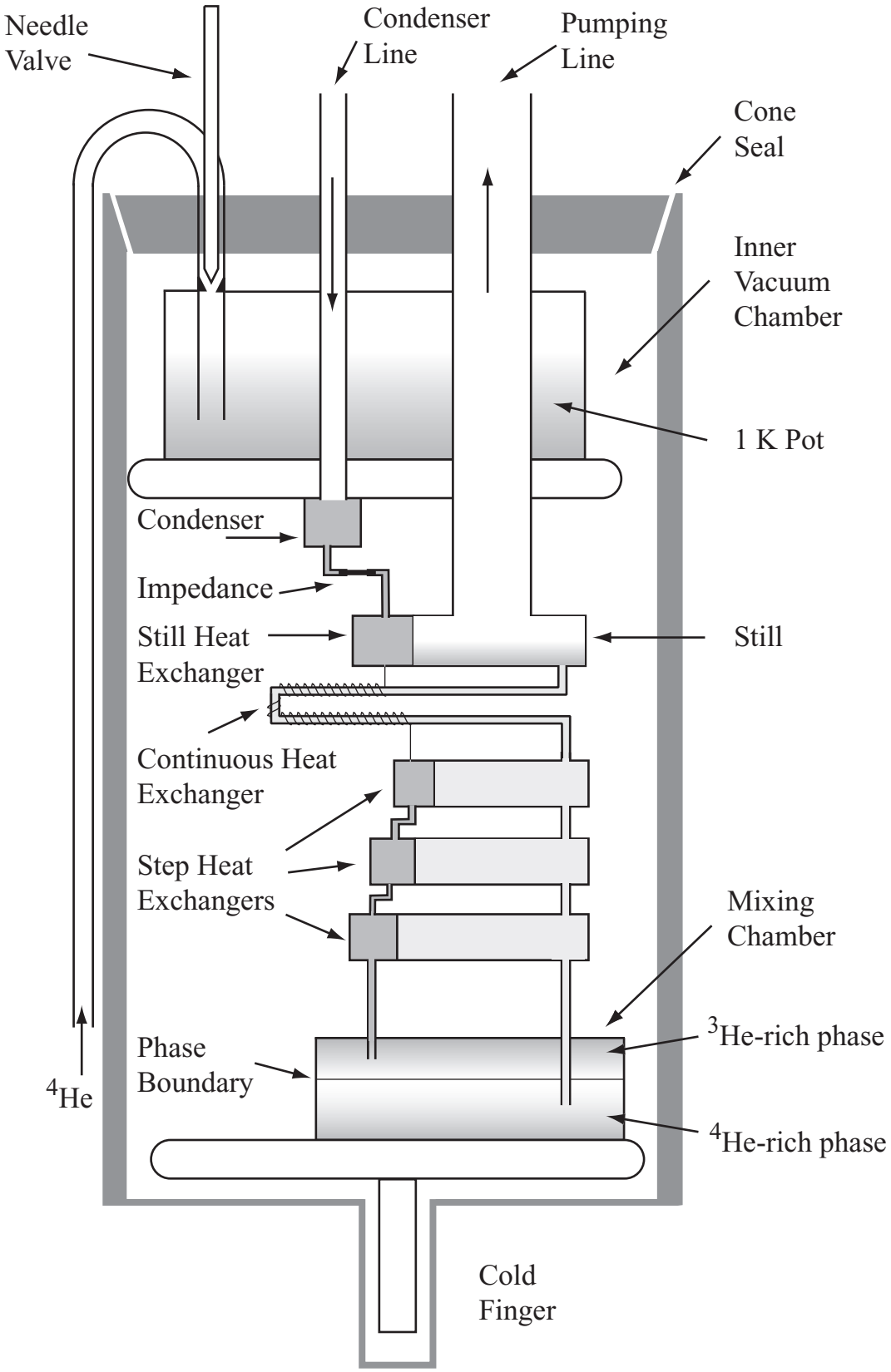

Figure 3.7 Schematic of a closed-loop dilution refrigerator unit, modeled after the Kelvinox 100 used for experiments performed in this thesis.

3.4 Low Temperature Measurements

3.4.1 Electronics

A voltage-bias measurement is the usual type of measurement performed on Coulomb blockaded nanostructures. In the Coulomb blockade regime, the resistance of the nanostructure changes by several orders of magnitude as it passes from a conductance peak to trough. A voltage-bias setup allows for a fixed voltage drop across the nanostructure at all times. The most common setup is a two-probe measurement, shown in Figure 3.8 (a). Using a lock-in detector (PAR 124A), a small a.c. excitation voltage is added to a variable d.c. offset V_{SD} and is applied to the nanostructure. The current is measured using a current preamplifier (Ithaco 1211). The resulting signal is the differential conductance dI/dV_{SD}. For zero d.c. offset (zero-bias measurement), the signal measured is simply the linear conductance $G = I/V_{SD} = dI/dV_{SD}\big|_{V_{SD}=0}$.

It is sometimes necessary to perform a four-probe voltage bias measurement. Four-probe measurements eliminate the resistances of the leads from the measured signal and allows for a direct measurement of the voltage drop across the sample. This is crucial if large resistors are placed in series with the sample (as was done when measuring the nanowires; see Chapter 7). The setup is shown in Figure 3.8 (b). Two phase-locked lock-in detectors (PAR 124A), a current amplifier (Ithaco 1211), and voltage amplifier (PAR 113) are used to measure dI, dV, and the voltage drop V_{dc}.

A current-bias measurement is sometimes used when the resistance of a nanostructure is large and somewhat constant. The setup is almost identical to a voltage-bias setup, except for a large resistor that is placed in series on the input line to generate the bias current.

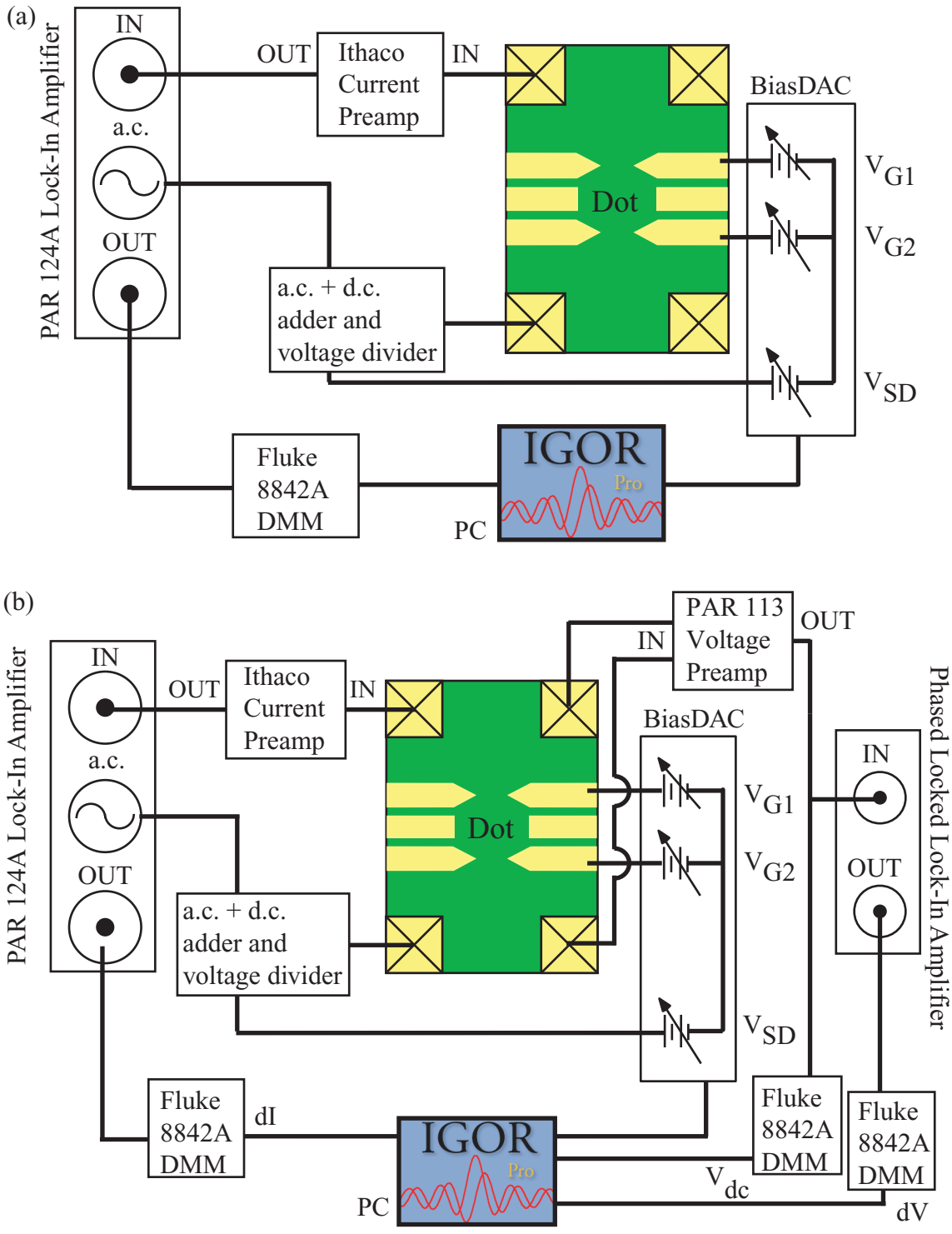

Figure 3.8 Circuit diagrams of (a) two-probe and (b) four-probe voltage bias measurements. A small a.c. excitation voltage from a lock-in amplifier added to a d.c. offset V_{SD} is passed to the ohmic contact of the quantum dot. In (b) two phased-locked lock-in amplifiers are used. Measurements are recorded using Fluke digital multimeters communicating via GPIB to a PC running IgorPro. The gate voltages and V_{SD} are computer-controlled, using the BiasDAC.

In all these setups, the measured voltage or current from the sample is first amplified, either with a PAR 113 voltage amplifier or Ithaco 1211 current amplifier, and then transmitted to a PAR 124A lock-in amplifier. The output from the PAR 124A is recorded by a Fluke 8842A digital multimeter and communicates with a PC through GPIB. IgorPro is used as the data acquisition software. The BiasDAC, used for computer-controlled voltage output, is described in detail in Ref. [38].

3.4.2 Magnetic Field Measurements

It is sometimes desirable to apply an external magnetic field when performing transport experiments. The dilution refrigerator is equipped with a 7 T superconducting solenoid and persistent current switch (American Magnetics Inc., Oak Ridge, TN). To operate the magnet, we connect it in series with a Dale 1% 0.1 Ω power resistor to a bipolar power supply (Kepco BOP 20-20, Flushing, NY). The current-to-magnetic field conversion factor was measured to be 0.2609 T/A. A schematic of the setup is shown in Figure 3.9. During an experiment, we monitor the voltage drop across the Dale power resistor to obtain an accurate measure of the magnetic field.

The following steps are used when operating the magnet persistent switch (MPS), [see Figure 3.9]:

Ramp up the magnetic field:

1. If a current is applied immediately, the MPS resistor R is superconducting, with R ~ 0, and current just flows through loop (a) without generating any magnetic field.

2. To generate a magnetic field, heat the MPS using I_{MPS} = 45 mA. This turns the superconducting MPS to normal, and therefore, increases its resistance to a non-zero value.

3. Apply a current I with the Kepco to generate the desired magnetic field (known from the conversion factor 0.2609 T/A). Because R is not zero, current is forced to flow through the superconducting solenoid, loop (b), and generates a magnetic field.

Set in persistent mode:

1. Cool down the MPS by setting I_{MPS} to zero. This returns R to the superconducting state, and the current I now flows through loop (c).

2. Ramp the Kepco to zero, however I still circulates in loop (c).

3. Turn off and disconnect the Kepco.

To turn off the magnetic field:

1. Connect the Kepco and turn on I to the *same* value used previously.

2. Heat the MPS using I_{MPS} = 45 mA.

3. Slowly ramp I to zero.

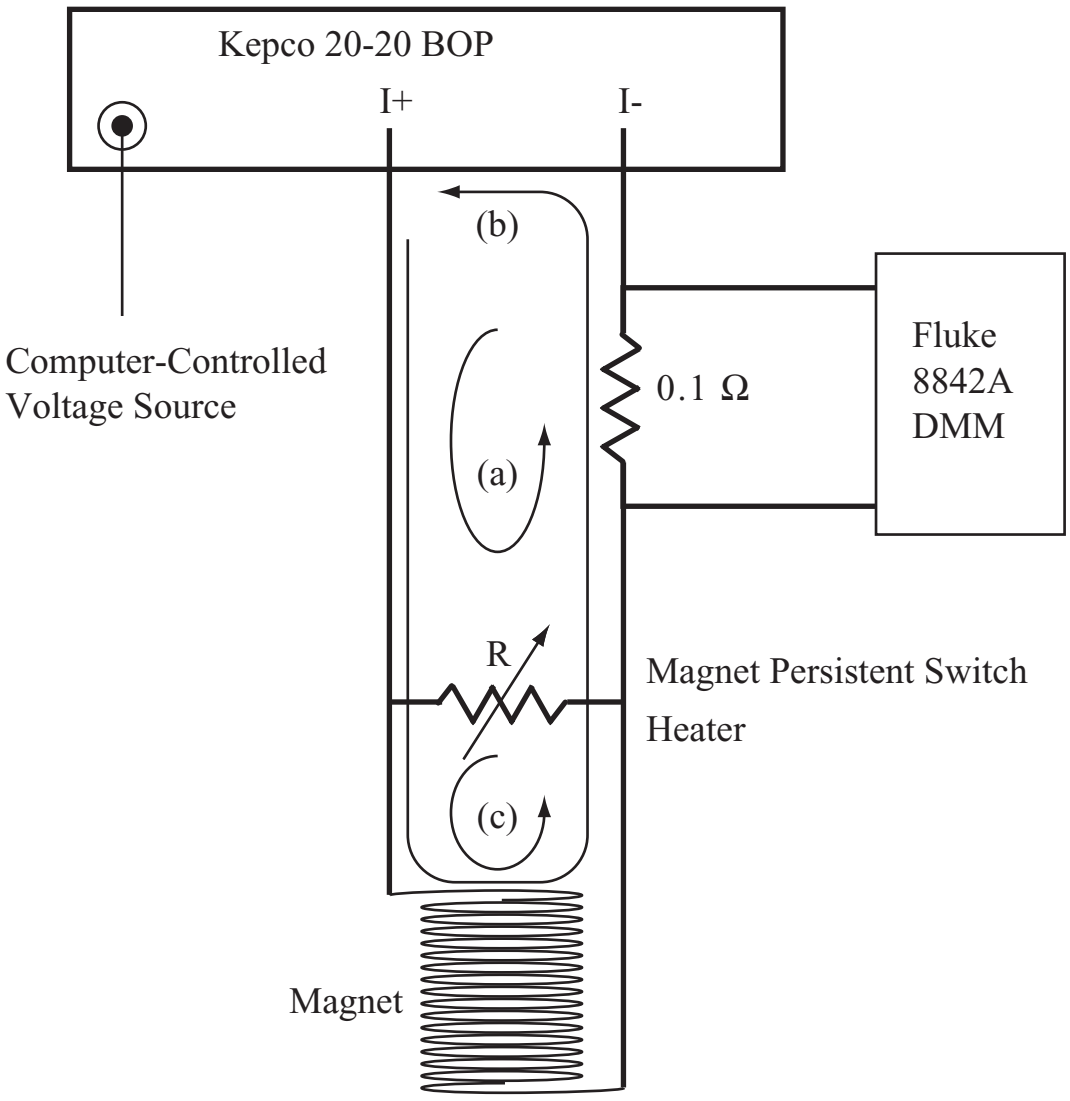

Figure 3.9 A programmable (computer-controlled) Kepco 20-20 BOP power supply delivers up to 20 Amps to the 7 T superconducting solenoid. In order to generate a magnetic field, the Magnet Persistent Switch must be operated (see text). For larger magnetic fields, two Kepco power supplies can be used, in a parallel configuration, to deliver 40 Amps (not shown).

3.5 Shubnikov-de Haas Measurements

After receiving the wafers from the Gossard group, low-temperature Hall measurements are usually performed in order to determine the electron sheet density and mobility at 4 K, and also to establish that the heterostructures were grown without any contaminants. A Hall bar is patterned on the sample using electron-beam lithography, with typical dimensions shown in the inset to Figure 3.10 (a), and the Hall resistance and magnetoresistance of the sample is measured.

The equation of motion for an electron in an applied electric and magnetic field is

$$\frac{m\vec{v}_d}{\tau_m} = e\vec{E} + e\vec{v}_d \times \vec{B} \tag{3.7}$$

where v_d is the drift velocity and τ_m is the momentum relaxation time. In matrix notation, this is

$$\begin{bmatrix} m/e\tau_m & -B \\ B & m/e\tau_m \end{bmatrix} \begin{bmatrix} v_x \\ v_y \end{bmatrix} = \begin{bmatrix} E_x \\ E_y \end{bmatrix} \tag{3.8}$$

Written in terms of the current density $\vec{J} = e\vec{v}_d n_s$ where n_s is the electron sheet density, we have

$$\begin{bmatrix} m/e\tau_m & -B \\ B & m/e\tau_m \end{bmatrix} \begin{bmatrix} J_x/en_s \\ J_y/en_s \end{bmatrix} = \begin{bmatrix} E_x \\ E_y \end{bmatrix} \tag{3.9}$$

or

$$\begin{bmatrix} E_x \\ E_y \end{bmatrix} = \sigma^{-1} \begin{bmatrix} 1 & -\mu B \\ \mu B & 1 \end{bmatrix} \begin{bmatrix} J_x \\ J_y \end{bmatrix} = \begin{bmatrix} \rho_{xx} & \rho_{xy} \\ \rho_{yx} & \rho_{yy} \end{bmatrix} \begin{bmatrix} J_x \\ J_y \end{bmatrix} \tag{3.10}$$

with $\sigma = en_s\mu$, $\mu = e\tau_m / m$, and the last equality defines the resistivity tensor.

We can measure the resistivity by using the Hall bar geometry shown in Figure 3.10 (a). The analysis for low magnetic fields is as follows. Since there is no current flowing in the y direction ($J_y = 0$), the components of the electric field are

$$E_x = \rho_{xx} J_x, E_y = \rho_{yx} J_x \tag{3.11}$$

Also, from $I = J_x W$, $V_x = V_1 - V_2 = E_x L$ and $V_H = V_2 - V_3 = E_y W$, where W and L are the dimensions of the Hall bar, we get

$$\rho_{xx} = \frac{V_x W}{IL}, \ \rho_{yx} = \frac{V_H}{I} \tag{3.12}$$

Using Equations (3.9) and (3.10), we find that

$$n_s = \frac{1}{e\frac{d\rho_{yx}}{dB}} = \frac{I}{e\frac{dV_H}{dB}} \tag{3.13}$$

$$\mu = \frac{1}{en_s\rho_{xx}} = \frac{IL}{en_s V_x W} \tag{3.14}$$

At high magnetic fields we find that the longitudinal resistivity ρ_{xx} oscillates with minimums corresponding to plateaus in the Hall resistivity ρ_{yx}. The magnetoresistance oscillations can be explained as follows. The density of states of the 2DEG becomes a sequence of delta functions. As the magnetic field rises, the Fermi energy moves from the center of one state to the center of the next state, giving rise to the oscillations in ρ_{xx}.

When a strong magnetic field is applied perpendicularly to a 2DEG, quantized energy states known as Landau levels are formed, with

$$E_n = (n - \frac{1}{2})\hbar\omega_c, \ \omega_c = \frac{eB}{m^*} \tag{3.15}$$

where ω_c is the cyclotron frequency, B is the applied magnetic field, and m^* is the effective mass of the electron. Furthermore, the area of the electron orbits

$$S_n = 4\pi^2 \frac{eB}{h}(n - \frac{1}{2}) \tag{3.16}$$

are quantized in k-space. As the magnetic field is increased, S_n expands, and we find an associated periodicity in the inverse magnetic field:

$$\Delta\left(\frac{1}{B}\right) = \frac{4\pi^2 e}{hS_n} \tag{3.17}$$

Using the density of states for zero magnetic field, we can write

$$S(B=0) = 2\pi^2 n_s \tag{3.18}$$

Therefore, we have

$$\Delta\left(\frac{1}{B}\right) = \frac{2e}{hn_s} \tag{3.19}$$

With the sheet density n_s of the 2DEG being dependent on the Fermi energy through the zero-field density of states, the change in the Fermi energy, and therefore also the magnetoresistance, with magnetic field will have a periodicity given by Equation (3.19). These are the Shubnikov-de Haas oscillations.

The preferred method to calculate the sheet density is to plot the maxima of the longitudinal resistivity as a function of 1/B. This will give a straight line with a slope proportional to the sheet density:

$$n_s = \frac{2e}{h}\frac{\Delta n}{\Delta(1/B)} \tag{3.20}$$

with n being the peak index.

Figure 3.10 (a) shows both the longitudinal and transverse (Hall) resistivity for a typical measurement performed at 4.2 K. As expected, the minimums in the oscillations correspond to plateaus in the transverse resistivity. Figure 3.10 (b) is a plot of the

longitudinal resistivity versus 1/B, showing the periodic oscillations. The inset shows a straight line fit of the peak index versus 1/B that allows for the determination of the sheet density using Equation (3.20). The mobility of the sample can be determined from Equation (3.14).

The table below lists the measured mobility and sheet density for the two wafers that were used for experiments in this thesis:

Wafer	Depth of 2DEG	Mobility at 4.2 K	Carrier Density at 4.2 K
020227B (MH2)	52 nm	464 000 cm^2/Vs	3.86×10^{11} cm^{-2}
020227C (MH3)	57 nm	396 000 cm^2/Vs	4.53×10^{11} cm^{-2}

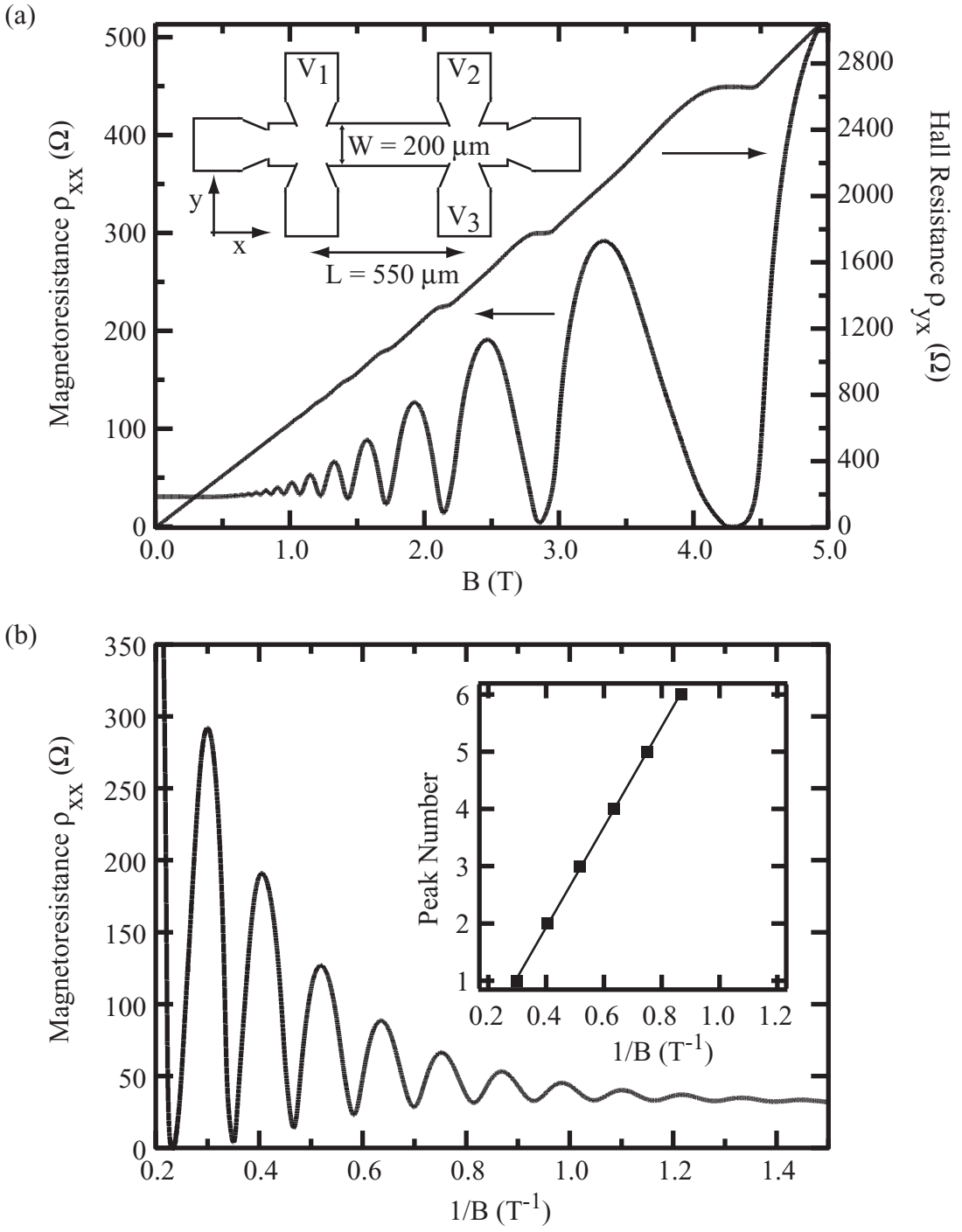

Figure 3.10 (a) Longitudinal magnetoresistance and Hall (transverse) resistance as a function of magnetic field B for wafer 020227B-MH2, measured at 4.2 K. *Inset*: Hall bar geometry used in these measurements. (b) Magnetoresistance oscillations as a function of 1/B. *Inset*: A straight line fit to the peak positions in 1/B and peak number (squares) from which the sheet density can be calculated (see text).

IV

Triple Quantum Dots

4.1 Overview

Semiconductor quantum dots are commonly referred to as artificial atoms: nanostructured devices where electrons are spatially confined and occupy discrete energy levels [43]. These artificial atoms are tunable, in that their shape, size, and electron density can be modified [44]. When two or more artificial atoms are allowed to interact, either by allowing electrons to tunnel between them or by a capacitive effect, artificial molecules are formed. For example, a system of two coupled quantum dots can be used to study how a molecular bond is formed as a function of electron tunneling between the individual artificial atoms, and an analog of the molecular binding energy can be measured [30,45].

Semiconductor quantum dots are also proving to be promising systems for nanometer scale single-electron circuits [46]. One advantage of using semiconductor quantum dots is scalability: making quantum dots smaller only enhances their properties and reduces their, already low, power consumption. Numerous quantum dot single-electron devices have already been demonstrated. Recent examples include a quantum dot electrometer [47] and a double quantum dot single-electron switch [48]. Quantum dots can be used as classical logic bits in future efficient, highly parallel nanoelectronic circuits. Furthermore, spins of localized electrons in quantum dots can serve as qubits for quantum information storage and processing [37]. In Section 2.5, we presented results on a double quantum dot device that can be tuned to the few-electron regime. Coupling two

quantum dots that contain just one electron each is the first step towards realizing coupled spin qubits.

There is great interest in investigating interactions between electrons in coupled dot systems. From a technological perspective, understanding and controlling electron interactions among multiple quantum dots is of fundamental importance and is required if a multiple quantum dot circuit element is to be built. In addition, electron-electron interaction is a central topic in condensed matter physics and can be explored with quantum dot systems. Over the last few years, coupled quantum dots in a *linear* arrangement have been studied thoroughly [31]. In this chapter, we present our research on triple quantum dots coupled in a (non-linear) ring geometry. Triple quantum dots are interesting in that they can be used as single-electron parametrons [49] or single-electron rectifiers [50,51] in nanometer scale electronic circuits, and are also important in quantum computing schemes, where they can be used as spin entanglers [52].

The outline of this chapter is as follows. In Section 4.2, we derive the stability diagram of a triple dot system, showing the existence of quadruple points. In Section 4.3, we describe the charge rectification behavior of a triple dot when tuned to the Coulomb blockade regime. Finally, in Section 4.4, we present a symmetric, tunnel-coupled triple dot device and describe the device characteristics. We also present exact diagonalization results on a triple dot system containing just two electrons.

4.2 Stability Diagram

It is useful to consider the stability, or charging, diagram of a triple quantum dot. In this section, we derive the stability diagram for a triple quantum dot using a classical capacitive charging model, where it is assumed that the number of electrons on each dot is an integer. As we saw in Section 2.5 for the double dot case, inter-dot tunneling is the dominant effect and not inter-dot capacitive coupling. Coupled quantum dots prefer to share electrons where, even though the total number of electrons in the coupled dot system as a whole is quantized, the number of electrons on each dot individually is not an integer. Electron sharing tends to lower the ground state energy of the coupled dot system. However, a capacitive charging model still provides a useful description of the triple quantum dot, and allows the stability diagram to be mapped. We follow the derivation presented in Chapter 2 and Ref. [31]. The triple quantum dot system is shown in Figure 4.1. All three dots are tunnel-coupled and transport is measured through the left and right leads connected to dot 1 and dot 2. Each dot has its own capacitively coupled side gate.

From Chapter 2, Equation (2.13), the electrostatic energy for a discrete system of n conductors is

$$U = \frac{1}{2}\sum_{i=1}^{n} Q_i V_i = \frac{1}{2}\sum_{i=1}^{n}\sum_{j=1}^{n} V_i C_{ij} V_j = \frac{1}{2}\sum_{i=1}^{n}\sum_{j=1}^{n} Q_i C_{ij}^{-1} Q_j \tag{4.1}$$

Using Figure 4.1, we can determine the total charge on each dot by summing up the charge stored on the capacitors to obtain

$$\begin{aligned} Q_1 &= C_R(V_1 - V_R) + C_{G1}(V_1 - V_{G1}) + C_{12}(V_1 - V_2) + C_{13}(V_1 - V_3) \\ Q_2 &= C_L(V_2 - V_L) + C_{G2}(V_2 - V_{G2}) + C_{12}(V_2 - V_1) + C_{23}(V_2 - V_3) \\ Q_3 &= C_{G3}(V_3 - V_{G3}) + C_{13}(V_3 - V_1) + C_{23}(V_3 - V_2) \end{aligned} \tag{4.2}$$

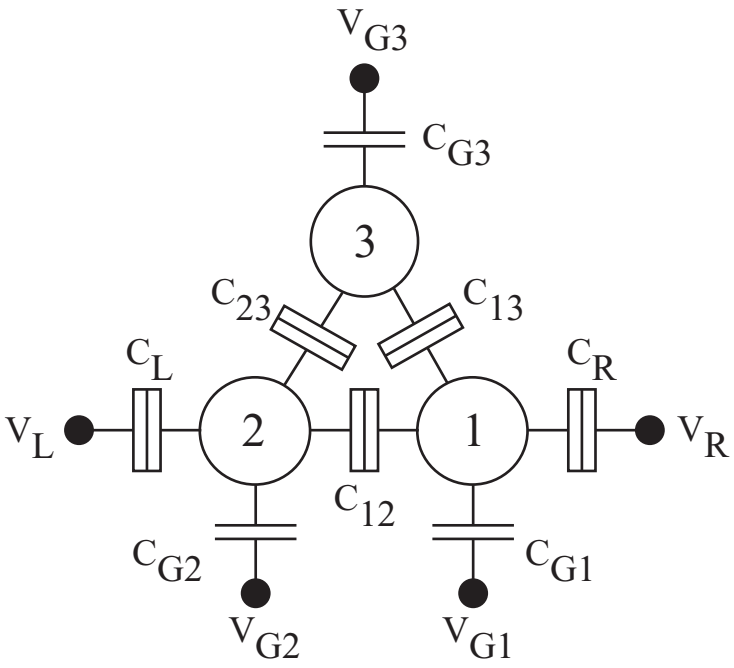

Figure 4.1 Circuit model of a triple quantum dot. Split boxes represent tunnel junctions. Each quantum dot (i = 1, 2, 3), with total capacitance C_i, has its own independent capacitively-coupled side gate, with gate voltage V_{Gi} and capacitance C_{Gi}. Cross-capacitances are neglected. For the triple dot rectifier, C_{23} is a pure capacitor.

where V_i is the electrostatic potential of dot i and all other variables are defined in Figure 4.1. Letting C_1, C_2, and C_3 be the total capacitance of dot 1, 2 and 3, respectively,

$$\begin{aligned} C_1 &= C_R + C_{G1} + C_{12} + C_{13} \\ C_2 &= C_L + C_{G2} + C_{12} + C_{23} \\ C_3 &= C_{G3} + C_{13} + C_{23} \end{aligned} \tag{4.3}$$

Equation (4.2) can be written as

$$\begin{bmatrix} Q_1 + V_R C_R + C_{G1} V_{G1} \\ Q_2 + V_L C_L + C_{G2} V_{G2} \\ Q_3 + C_{G3} V_{G3} \end{bmatrix} = \begin{bmatrix} C_1 & -C_{12} & -C_{13} \\ -C_{12} & C_2 & -C_{23} \\ -C_{13} & -C_{23} & C_3 \end{bmatrix} \begin{bmatrix} V_1 \\ V_2 \\ V_3 \end{bmatrix} \tag{4.4}$$

Now, we are interested only in the linear transport regime, where $V_L = V_R = 0$. Solving for **V**:

$$\begin{bmatrix} V_1 \\ V_2 \\ V_3 \end{bmatrix} = \begin{bmatrix} \dfrac{(C_2C_3 - C_{23}^2)(Q_1 + C_{G1}V_{G1}) + (C_{12}C_3 + C_{13}C_{23})(Q_2 + C_{G2}V_{G2}) + (C_{12}C_{23} + C_{13}C_2)(Q_3 + C_{G3}V_{G3})}{C_1C_2C_3 - 2C_{12}C_{13}C_{23} - C_1C_{23}^2 - C_2C_{13}^2 - C_3C_{12}^2} \\ \dfrac{(C_{12}C_3 + C_{13}C_{23})(Q_1 + C_{G1}V_{G1}) + (C_1C_3 - C_{13}^2)(Q_2 + C_{G2}V_{G2}) + (C_1C_{23} + C_{13}C_{12})(Q_3 + C_{G3}V_{G3})}{C_1C_2C_3 - 2C_{12}C_{13}C_{23} - C_1C_{23}^2 - C_2C_{13}^2 - C_3C_{12}^2} \\ \dfrac{(C_{12}C_{23} + C_{13}C_2)(Q_1 + C_{G1}V_{G1}) + (C_1C_{23} + C_{13}C_{12})(Q_2 + C_{G2}V_{G2}) + (C_1C_2 - C_{12}^2)(Q_3 + C_{G3}V_{G3})}{C_1C_2C_3 - 2C_{12}C_{13}C_{23} - C_1C_{23}^2 - C_2C_{13}^2 - C_3C_{12}^2} \end{bmatrix} \tag{4.5}$$

Setting $Q_1 = -eN_1$, $Q_2 = -eN_2$, and $Q_3 = -eN_3$, where N_i is the number of electrons on dot i, we can solve for the electrostatic potential energy of the triple dot using Equation (4.1). We find that:

$$U = \frac{1}{2}E_{C1}N_1^2 + \frac{1}{2}E_{C2}N_2^2 + \frac{1}{2}E_{C3}N_3^2 + N_1N_2E_{C12} + N_1N_3E_{C13} + N_2N_3E_{C23} + f(V_{G1}, V_{G2}, V_{G3}) \tag{4.6}$$

or, more compactly,

$$U(N_1, N_2, N_3) = \sum_{i=1}^{3} \frac{1}{2}E_{Ci}N_i^2 + \sum_{i<j,\, j=2}^{3} N_iN_jE_{Cij} + f(V_{G1}, V_{G2}, V_{G3}) \tag{4.7}$$

where N_i is the number of electrons in dot i. The first term represents the charging energy of the three individual dots, with

$$E_{Ci} = \frac{e^2}{C_i}\left(1 - \frac{2C_{12}C_{13}C_{23} + C_j C_{ik}^2 + C_k C_{ij}^2}{C_1 C_2 C_3 - C_i C_{jk}^2}\right)^{-1} \tag{4.8}$$

Note that this is the usual charging energy for the uncoupled dot i, multiplied by a factor due to the coupling caused by dot j and dot k. The second term in Equation (4.7) represents the electrostatic coupling energy between dot i and dot j, in the presence of dot k, for the three pairs, given by

$$E_{Cij} = \frac{e^2(C_{ij}C_k + C_{ik}C_{jk})}{C_1 C_2 C_3 - 2C_{12}C_{13}C_{23} - C_1 C_{23}^2 - C_2 C_{13}^2 - C_3 C_{12}^2} \tag{4.9}$$

Finally, $f(V_{G1},V_{G2},V_{G3})$ is the electrostatic energy due to the induced charge by the capacitively-coupled side gates and is given by

$$\begin{aligned} f(V_{G1},V_{G2},V_{G3}) &= \frac{1}{2e^2}\left(C_{G1}^2 V_{G1}^2 E_{C1} + C_{G2}^2 V_{G2}^2 E_{C2} + C_{G3}^2 V_{G3}^2 E_{C3}\right) \\ &+ \frac{1}{e^2}(C_{G1}V_{G1}C_{G2}V_{G2}E_{C12} + C_{G1}V_{G1}C_{G3}V_{G3}E_{C13} + C_{G2}V_{G2}C_{G3}V_{G3}E_{C23}) \\ &- \frac{1}{e}\left[\begin{array}{c} C_{G1}V_{G1}(N_1E_{C1} + N_2E_{C12} + N_3E_{C13}) + C_{G2}V_{G2}(N_1E_{C12} + N_2E_{C2} + N_3E_{C23}) \\ + C_{G3}V_{G3}(N_1E_{C13} + N_2E_{C23} + N_3E_{C3}) \end{array}\right] \end{aligned} \tag{4.10}$$

The electrochemical potential of a single dot equals the energy needed to add one electron to the dot, while keeping the number of electrons on the other dots constant:

$$\begin{aligned} \mu_1(N_1,N_2,N_3) &\equiv U(N_1,N_2,N_3) - U(N_1-1,N_2,N_3) \\ \mu_2(N_1,N_2,N_3) &\equiv U(N_1,N_2,N_3) - U(N_1,N_2-1,N_3) \\ \mu_3(N_1,N_2,N_3) &\equiv U(N_1,N_2,N_3) - U(N_1,N_2,N_3-1) \end{aligned} \tag{4.11}$$

This gives us:

$$\begin{aligned} \mu_1(N_1,N_2,N_3) &\equiv (N_1 - \frac{1}{2})E_{C1} + N_2E_{C12} + N_3E_{C13} - \frac{1}{e}\left(C_{G1}V_{G1}E_{C1} + C_{G2}V_{G2}E_{C12} + C_{G3}V_{G3}E_{C13}\right) \\ \mu_2(N_1,N_2,N_3) &\equiv (N_2 - \frac{1}{2})E_{C2} + N_1E_{C12} + N_3E_{C23} - \frac{1}{e}\left(C_{G1}V_{G1}E_{C12} + C_{G2}V_{G2}E_{C2} + C_{G3}V_{G3}E_{C23}\right) \\ \mu_3(N_1,N_2,N_3) &\equiv (N_3 - \frac{1}{2})E_{C3} + N_1E_{C13} + N_2E_{C23} - \frac{1}{e}\left(C_{G1}V_{G1}E_{C13} + C_{G2}V_{G2}E_{C23} + C_{G3}V_{G3}E_{C3}\right) \end{aligned} \tag{4.12}$$

The addition energy of a quantum dot is the energy required to add a single electron, $\mu_{dot}(N+1)-\mu_{dot}(N)$, and is the same as the charging energy. From the equations above, we find that

$$\begin{aligned}\mu_1(N_1+1,N_2,N_3)-\mu_1(N_1,N_2,N_3)&=E_{C1}\\ \mu_2(N_1,N_2+1,N_3)-\mu_2(N_1,N_2,N_3)&=E_{C2}\\ \mu_3(N_1,N_2,N_3+1)-\mu_3(N_1,N_2,N_3)&=E_{C3}\end{aligned} \tag{4.13}$$

as expected.

As a simple test of our results, we can remove the inter-dot coupling from the system by setting $C_{12} = C_{13} = C_{23} = 0$. We find that

$$E_{C1}=\frac{e^2}{C_1}, E_{C2}=\frac{e^2}{C_2}, E_{C3}=\frac{e^2}{C_3}, E_{C12}=E_{C13}=E_{C23}=0 \tag{4.14}$$

and

$$\begin{aligned}f(V_{G1},V_{G2},V_{G3})=&\frac{C_2C_3C_{G1}^2V_{G1}^2-2C_2C_3C_{G1}V_{G1}eN_1}{2C_1C_2C_3}\\ &+\frac{C_1C_3C_{G2}^2V_{G2}^2-2C_1C_3C_{G2}V_{G2}eN_2}{2C_1C_2C_3}+\frac{C_1C_2C_{G3}^2V_{G3}^2-2C_1C_2C_{G3}V_{G3}eN_3}{2C_1C_2C_3}\end{aligned} \tag{4.15}$$

Substituting these values into Equation (4.6), we obtain

$$U=\frac{\left(C_{G1}V_{G1}-eN_1\right)^2}{2C_1}+\frac{\left(C_{G2}V_{G2}-eN_2\right)^2}{2C_2}+\frac{\left(C_{G3}V_{G3}-eN_3\right)^2}{2C_3} \tag{4.16}$$

which is the electrostatic energy of three independent dots, as expected.

For zero source-drain voltage across the triple dot, the electrochemical potential of the leads is pinned to the Fermi energy E_F. Stable states of the triple quantum dot occur when the charge state (N_1, N_2, N_3) takes on the largest possible *integer* values while maintaining an electrochemical potential less than E_F for each dot. In these stable regions, the triple dot is in the Coulomb blockade and the charge state does not change. The triple

quantum dot stability diagram, which is a map of these stable states versus the three independent side gate voltages, is shown in Figure 4.2. Only where the stable states intersect can electrons tunnel between the dots, thereby changing the charge state. There exists a "quadruple point" where the four states (N_1, N_2, N_3), $(N_1 + 1, N_2, N_3)$, $(N_1, N_2 + 1, N_3)$, and $(N_1, N_2, N_3 + 1)$ are degenerate. This is similar to a double dot system, which exhibits a triple point. Finally, we note that our circuit model approach was recently used by Gaudreau *et al.* to successful explain their results [53].

4.3 Triple Dot Charge Rectifier

Interactions between dots, caused by inter-dot tunneling or capacitive-coupling, give rise to changes in the conductance spectra and current-voltage characteristics of the system. It has been shown that Coulomb interaction between dots can give rise to ratchet effects [50]. The Coulomb blockade formalism [54], used to describe single-electron charging and transport through a multiple quantum dot system, can be used to predict these ratchet effects. Work with quantum dots displaying ratchet behavior has been explored both experimentally and theoretically [55,56]. In this section, we present an experimental realization of a triple quantum dot rectifier, or Coulomb blockade charging ratchet, as proposed in Ref. [50]. Here, three quantum dots are arranged in an *asymmetric* configuration such that a rectifying effect, characteristic of ratchet behavior [57], is observed.

The ratchet mechanism observed in this triple quantum dot is a bias-dependent current rectification [50], similar to the effect seen with a hybrid molecular electronic device [58]. As is typical for a ratchet, breaking of symmetry under inversion must be

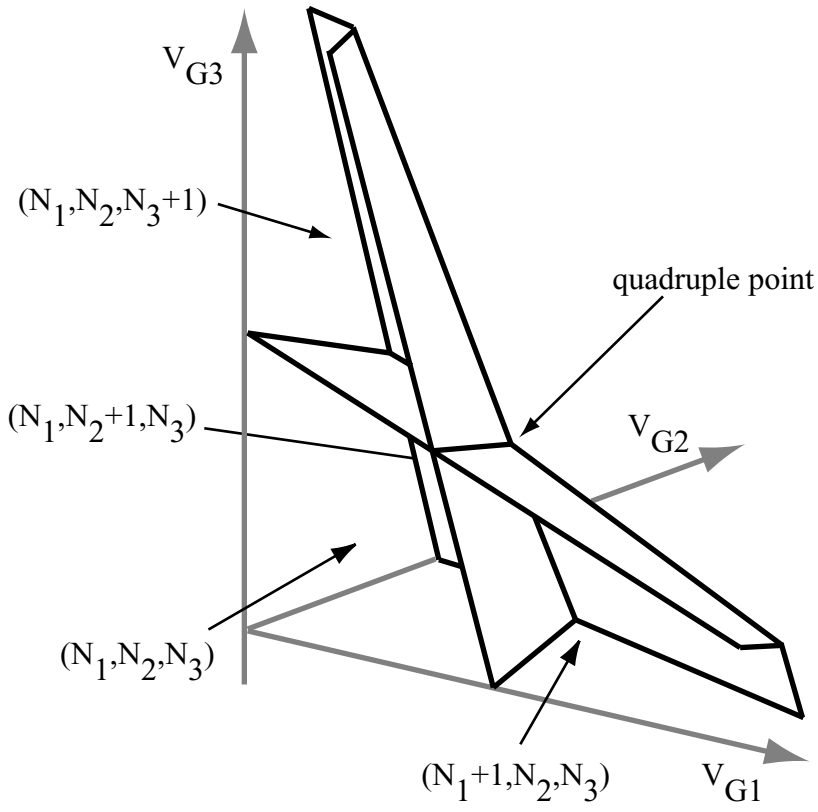

Figure 4.2 First cell of the stability (charging) diagram of a triple quantum dot with nonzero inter-dot coupling. A hexagonal pattern for each pair of dots leads to a quadruple point in the 3-dimensional (V_{G1},V_{G2},V_{G3}) space.

present, and is introduced here by placing an infinite barrier between dots 2 and 3. Because no tunneling takes place between dots 2 and 3, dot 3 is a quantum box that is tunnel-coupled with dot 1. Dot 2 and dot 3 are now only capacitively-coupled. That is, C_{23} in the circuit model of the triple dot presented in Figure 4.1 is now just a pure capacitor, and tunneling can only occur between dots 1 and 2 and dots 1 and 3. However, dots 2 and 3 interact capacitively. As we derived in Section 4.2, the stability diagram displays a quadruple point, analogous to the triple point of a double dot system, where four states are degenerate. These four states correspond to no *excess* electrons in the system or one *excess* electron on one of the three dots. Therefore, the triple dot can be tuned such that *zero* or *only one* excess electron is allowed in the device. This is crucial for the operation of a triple dot as a charging ratchet. At the quadruple point, a current can flow if an electron tunnels through the device, *one at a time*. For small source-drain voltage, while operating the device at the quadruple point, the energy of all four states is degenerate, and an electron can tunnel from the source to the drain through multiple tunneling events between all three dots. However, as the source-drain voltage is increased, the degeneracy of the quadruple point is broken, and if an electron tunnels into the quantum box, dot 3, it gets trapped there, and prohibits the flow of current. For reverse bias no trapping occurs. A schematic of this process is shown in Figure 4.3. The current through the triple dot is inversely proportional to the trapping ratio $\gamma_{3\leftarrow 1}/\gamma_{1\leftarrow 3}$, where $\gamma_{j\leftarrow i}$ is the rate of tunneling from *dot i* to *dot j* [50]. Using the orthodox theory of the Coulomb blockade, it can be shown that

$$\gamma_{3\leftarrow 1}/\gamma_{1\leftarrow 3} = e^{\Delta U_{13}/k_B T} \tag{4.17}$$

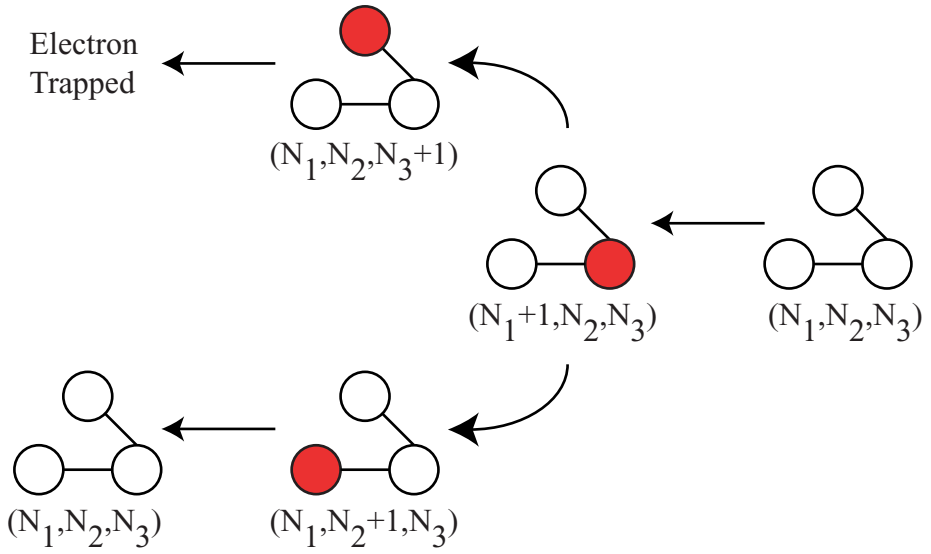

Figure 4.3 Schematic diagram showing the jamming process for the triple quantum dot charging ratchet. At the quadruple point, only these four degenerate states are accessible. A small forward bias breaks this degeneracy, and allows for an electron to be trapped in dot 3. Current can flow only if the electron follows the lower path. For reverse bias no trapping occurs.

Here, ΔU_{13} is the change in global free energy of the system when a tunneling event between dot 1 and dot 3 occurs, and is linearly proportional to the source-drain voltage V_{SD}. We then have that for increased V_{SD}, trapping dominates, and the current is rectified. For reverse biasing, no trapping occurs, and the current is not suppressed. The charge rectification in the triple dot system is analogous to a spin-Coulomb blockade rectifier using a double quantum dot [59]. Both of these devices act as molecular rectifiers for electrons, furthering the analogy between coupled quantum dots and artificial molecules.

4.3.1 Monte Carlo Simulations

In section 4.2, we derived the electrostatic energy of a triple dot system from an equivalent circuit model, and used it to plot the stability diagram. By including a non-zero voltage bias (i.e., $V_L, V_R \neq 0$), this model can also be used in a Monte Carlo simulation. We are interested in calculating the current-voltage characteristics of the triple dot to reveal the rectification caused by the asymmetric tunneling configuration.

The Monte Carlo simulation begins with the initializing of the charge state of the triple dot to (N_1, N_2, N_3), depending on the side gate voltages. Then, a new charge state is determined after a single tunneling event occurs, and the charge state is updated. This process is repeated over a very large number of transitions. By keeping track of the number of electrons entering or leaving the leads, the current can be calculated.

Single-electron tunneling is allowed between neighboring dots (and leads). For example, an electron may tunnel to dot 1 from the left lead, or from dot 1 to dot 2. For a fully coupled triple dot, 10 such transitions are allowed. However, because we are

modeling the triple dot rectifier, we do not allow tunneling between dots 2 and 3, and therefore, there are only 8 transitions to take into account. Each transition will have associated with it a change in energy ΔU. The tunneling rate $\gamma_{j\leftarrow i}$ from dot (or lead) i to dot (or lead) j is

$$\gamma_{j\leftarrow i} = -\left(\frac{1}{e^2 R_t}\right)\frac{\Delta U_{j\leftarrow i}}{1-\exp(\Delta U_{j\leftarrow i}/k_B T)} \tag{4.18}$$

where R_t is the tunnel junction resistance (assumed to be equal for all junctions) and $\Delta U_{j\leftarrow i}$ is the associated change in energy for the transition. Using these tunneling rates, we can determine the most probable transition to occur, given the current charge state of (N_1, N_2, N_3). A simple method to do this is to calculate, using Equation (4.18), all 8 tunneling rates for the 8 possible tunneling events that may occur. We then divide the interval [0,1] into 8 subintervals, each proportional to one of the calculated rates, and finding in which subinterval a random number, uniformly distributed over [0,1], falls.

The Monte Carlo simulation is based on a classical charging model of electron transport in quantum dots. Several assumptions were made, including: (i) a continuous energy spectrum; (ii) a tunnel barrier traversal time of tunneling electrons that is negligible, or at least much less than the time between consecutive tunneling events; (iii) a well-defined integer number of electrons localized on each of the dots.

Results of the simulations are shown in Figure 4.4. Asymmetric I-V characteristics are obtained, with current rectification and negative differential resistance for positive V_{SD}. A further discussion of these curves is given in the next section.

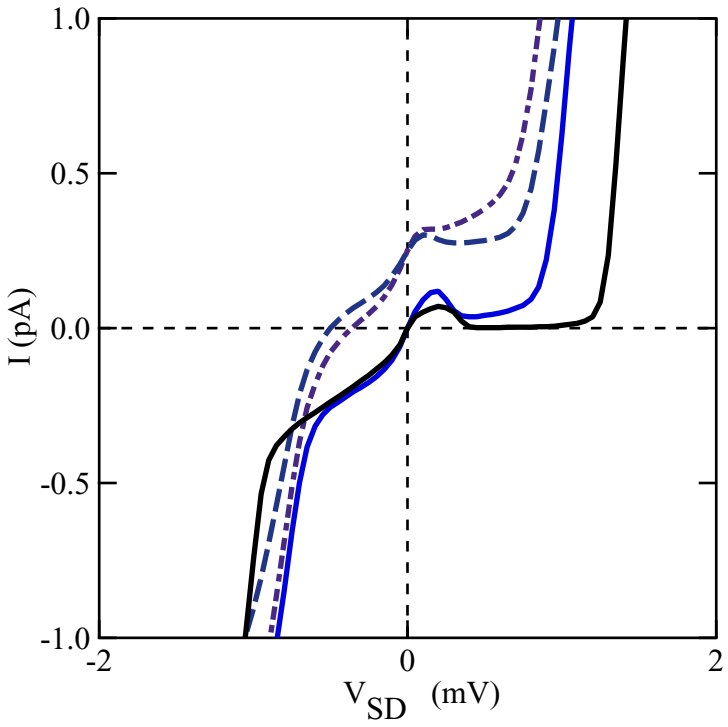

Figure 4.4 Monte Carlo simulations of the triple quantum dot I-V characteristics. Dot 3 is isolated from lead III, and a current is measured versus applied voltage $V_{SD} = V_R - V_L$. Current suppression and negative differential resistance for $V_{SD} > 0$ is found. Parameters used in the simulation are calculated from a self-consistent simulation of the full 3D structure of the device. Dashed lines are simulated at T = 450 mK and solid lines at T = 350 mK. From bottom for $V_{SD} > 0$: $C_1 = C_2 = 210$ aF, $C_3 = 50$ aF; $C_1 = C_2 = 280$ aF, $C_3 = 50$ aF; $C_1 = C_2 = 280$ aF, $C_3 = 105$ aF, $C_{23} = 50$ aF; $C_1 = C_2 = 280$ aF, $C_3 = 105$ aF, $C_{23} = 33$ aF; Upper two curves are offset vertically by 0.25 pA for clarity.

4.3.2 Experimental Results

In this section, we present an experimental realization of a triple quantum dot charging ratchet. Figure 4.5 shows a scanning electron micrograph of the triple quantum dot charging ratchet. Fifteen independently tunable Cr:Au gates are used to define three coupled quantum dots in a GaAs/$Al_{0.3}Ga_{0.7}As$ heterostructure containing a two-dimensional electron gas located 57 nm below the surface. At 4K, the 2DEG sheet carrier density and mobility are $n_s = 4.5 \times 10^{11}$ cm^{-2} and $\mu = 400\,000$ $cm^2\,V^{-1}s^{-1}$. The three dots are arranged in a ring structure, with tunneling possible between dots 1 and 2 and dots 1 and 3. No exchange of electrons is allowed between dots 2 and 3 because of the infinite barrier resulting from the center metal gate. A finite-bias Coulomb blockade measurement of dot 2 is shown in Figure 4.6, from which we can deduce the total dot capacitance to be $C_2 \sim 310$ aF. All measurements were performed in a ^{3}He-system at the base temperature of 380 mK and measured electron temperature of 440 mK.

We operate the triple dot device in the Coulomb blockade regime. We are able to tune the device to the quadruple point by (i) energizing all the gates to deplete the electron gas underneath to form three open quantum dots; (ii) independently tuning each dot to the tunneling regime and then to a Coulomb blockade peak; (iii) returning all fifteen gates to the values found in the previous step; (iv) pinching off the lead to dot 3, thereby forming a quantum box. We measure a dc current I from an applied source-drain voltage V_{SD} across dots 1 and 2.

Current-voltage (I-V) characteristics of the triple dot charging rectifier are shown in Figure 4.7, including polynomial interpolation of the data. The I-V characteristics show the rectification effect due to the charging of the quantum box, i.e. trapping an

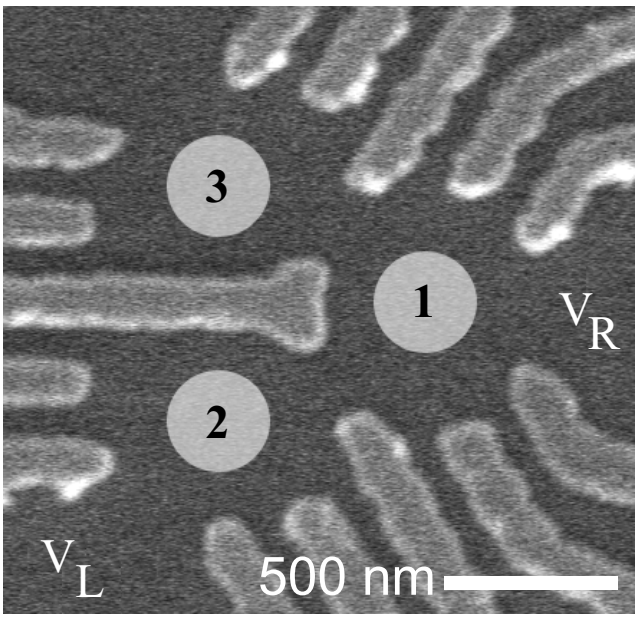

Figure 4.5 Scanning electron micrograph of the triple quantum dot rectifier. The light areas are Cr:Au gates used to define the quantum dots. The locations of the dots are highlighted by circles. This geometry allows for tunneling between dots 1 and 2, and between dots 1 and 3. Dots 2 and 3 are capacitively-coupled, but no electrons may tunnel between these dots.

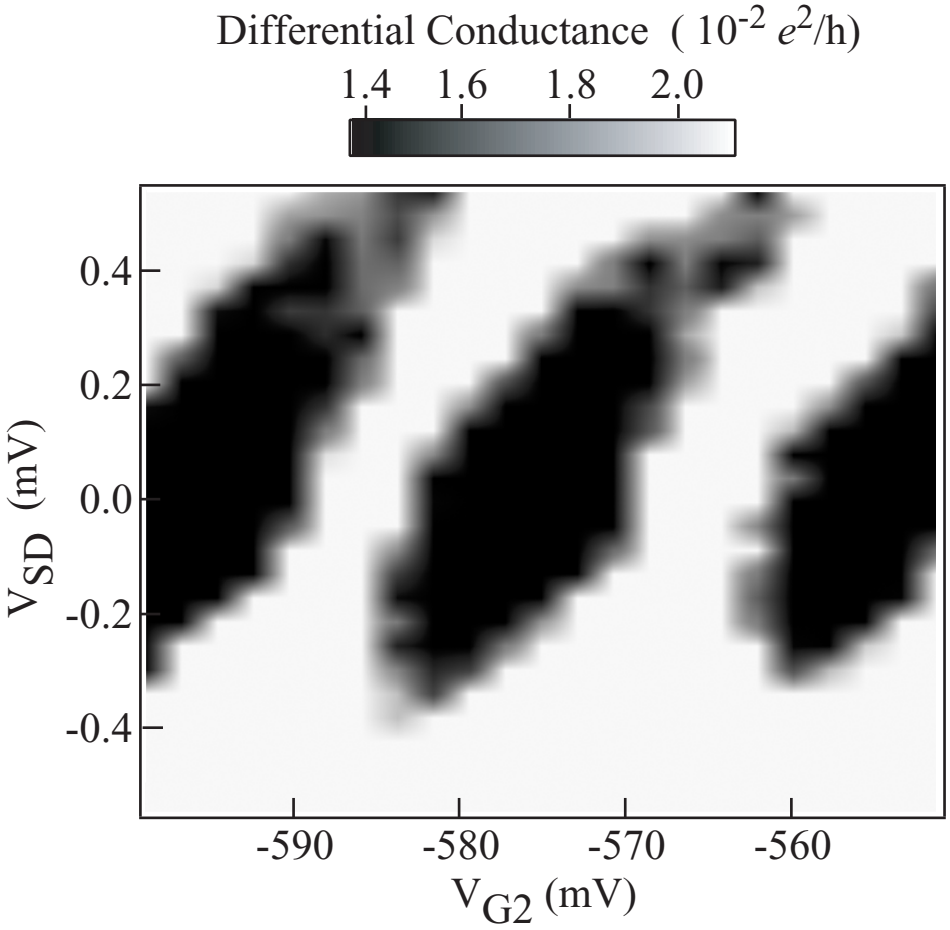

Figure 4.6 Differential conductance of dot 2 as a function of its side gate voltage and the dc bias. The diamonds are Coulomb blockaded regions from which we measure the total dot capacitance $C_2 \sim 310$ aF.

electron in dot 3. The ratchet behavior expected is clearly observed: (i) for $V_{SD} < 0$, current flows through the device; (ii) for V_{SD} near zero, the current is symmetric; (iii) as V_{SD} is made more positive, trapping in dot 3 dominates, and the current is rectified; (iv) as V_{SD} is further increased, the rectification effect is overcome. Properties (i) and (iii) follow from Equation (4.17) directly. Property (ii) is a direct consequence of operating the triple dot at the quadruple point where the four allowed states of the system are degenerate. Property (iv) is a result of the high source-drain voltage pushing the system away from the quadruple point and allowing for more than one electron in the system at a given time. Negative resistance is also observed in the I-V characteristics, and is seen clearly in Figure 4.7 (b).

Monte-Carlo simulations of the I-V characteristics of our device are shown in Figure 4.4. Junction resistances were used to fit the overall current range in the ohmic regime for negative bias. The parameters used in the Monte-Carlo simulations (the various dot capacitances) were derived from self-consistent simulations of the full three-dimensional structure [60], which includes the wafer profile and the device surface gate pattern. These self-consistent simulations show that the capacitance of a single dot is approximately 280 aF, similar to the value of 310 aF extracted from the Coulomb blockade diamond of Figure 4.6. The resumption of current at the edge of the suppression region for positive V_{SD} requires the addition of a second excess electron to the dot system. Analytically, the condition for this second electron entry gives a source-drain voltage threshold

$$V_{SD} = \frac{e[C_a^{-1}]_{13}}{1+[C_a^{-1}]_{11}C_L} \tag{4.19}$$

where C_a is the capacitance sub-matrix between the three dots and C_L is the capacitance between the left lead and the dot 1. This requires that we assume a smaller trapping dot in order to obtain a suppression region comparable to the experimental results. This is reasonable considering that the trapping dot is acting as a quantum box with only one lead.

The measured I-V characteristics in Figure 4.7 and the simulations in Figure 4.4 show that the rectification effect is tunable, depending on the capacitive-coupling C_{23} between dots 2 and 3. We are able to decrease C_{23} while maintaining approximately constant junction resistances by applying a more negative voltage on the center gate, while raising the voltage on the two opposite inter-dot quantum point contact gates. Figure 4.7 shows two I-V curves for our device under weak and strong capacitive-coupling of dots 2 and 3. For larger C_{23}, stronger rectification is observed, as predicted by the Monte-Carlo simulations. The simulations verify the features seen in the data, including the crossing of the two curves at $V_{SD} = 0$.

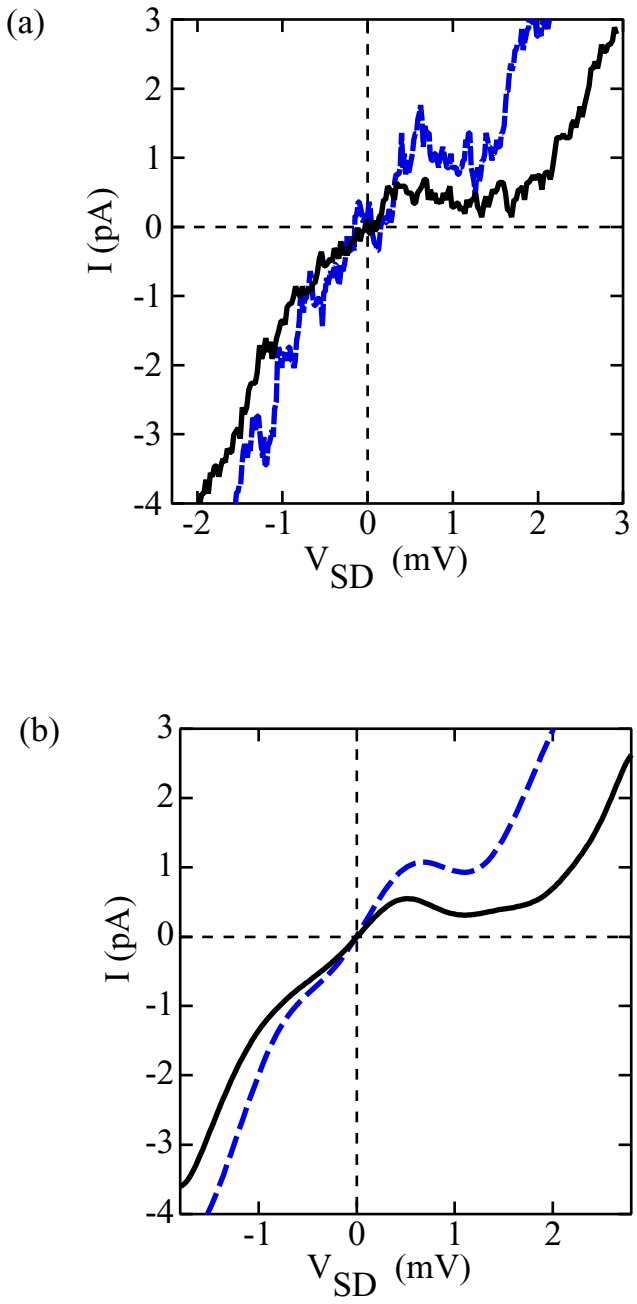

Figure 4.7 (a) I-V characteristics of the triple quantum dot. The dotted (solid) line corresponds to weaker (stronger) coupling between dots 2 and 3, which gives rise to weaker (stronger) current suppression for forward bias. (b) Polynomial interpolation of the data in (a). I(V) is symmetric around $V_{SD} = 0$ for both curves, which is a distinct feature of operating at the quadruple point. The region of negative differential resistance for $V_{SD} > 0$ is clearly observed.

4.4 Three Quantum Dots in a Ring

In this section, we consider a fully symmetric tunnel-coupled triple quantum dot system. We are especially interested in triple quantum dots for quantum information processing. The exchange interaction, which is able to be tuned by controlling the tunnel-coupling between a pair of quantum dots, has been suggested as a way to control qubit-qubit interactions (two-qubit operations) in a quantum dot spin-qubit circuit [37]. To this end, double quantum dots, in both serial and parallel configurations [30,31,36,45,47,48], have been studied extensively. However, in a practical quantum computing architecture, there will be more than just two qubits present, and the effect a third qubit, for example, would have on a two-qubit system should be considered. A fully symmetric triple quantum dot allows such a system to be studied. By only energizing certain gates, a double dot system can be defined and studied. Then, the third dot can be turned on, and its effect on the double dot can be observed. In Section 4.4.1 a fully symmetric triple dot that we have fabricated is presented, along with several measurements in the Coulomb blockade regime. In Section 4.4.2, numerical techniques are used to study a two-electron triple dot. We find that in the triple dot, exchange coupling is far more complex than in the double dot case.

4.4.1 Device Design and Characterization

Figure 4.8 shows a scanning electron micrograph of a symmetric triple quantum dot. Lithographically patterned Cr:Au gates are used to define three quantum dots in a GaAs/$Al_{0.3}Ga_{0.7}As$ heterostructure containing a 2DEG located 52 nm below the surface. An ion-etched trench, 30 nm deep, is used to deplete the 2DEG in the center region. At

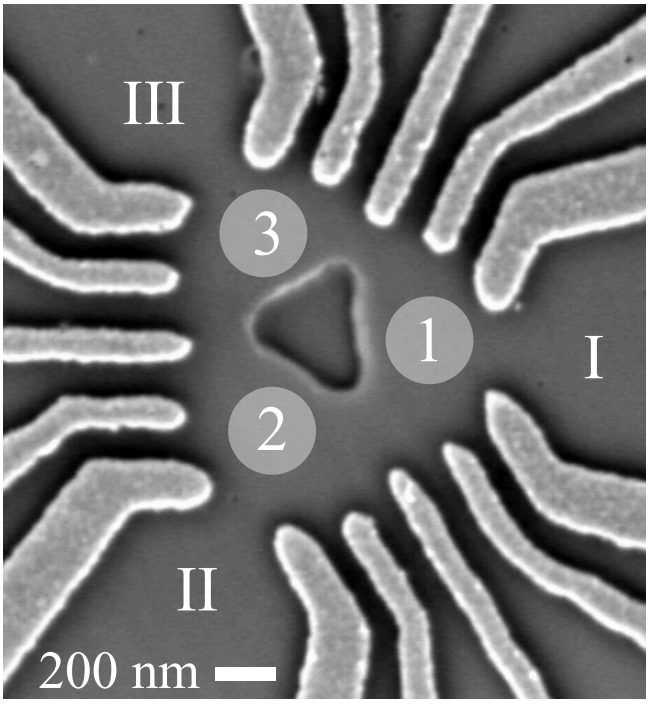

Figure 4.8 Scanning electron micrograph of a triple quantum dot. Light gray areas are tunable metal gates. Dark center region is a 30 nm deep ion-etched trench. Dot locations are marked by the circles.

4K, the 2DEG sheet carrier density and mobility are $n_s = 3.8 \times 10^{11}$ cm^{-2} and $\mu = 460\,000$ cm^2 V^{-1}s^{-1}. The main difference between this device and the triple dot used as a rectifier [Figure 4.5], is that this geometry allows for tunnel-coupling between any two dots.

We operate the triple quantum dot device in the Coulomb blockade regime. Figure 4.9 shows the addition spectrum for the triple quantum dot measured through leads I and II while completely isolating dot 3 from lead III. All three inter-dot quantum point contacts are set to ~ $2e^2/h$, thereby having the triple dot act as one big dot, with the usual finite-bias Coulomb blockade diamonds observed. From the data, we find that the total capacitance of the single large composite dot is ~ 615 aF, corresponding to a charging energy of 0.26 meV. From separate measurements, we find the total capacitance for a single dot to be ~ 256 aF, corresponding to a charging energy of 0.625 meV. The total dot capacitance of a single dot of the triple dot rectifier, determined from finite-bias Coulomb blockade measurements shown in Figure 4.6, is 310 aF, corresponding to a charging energy of 0.515 meV. We note that due to lateral depletion of the ion-etched trench, the actual dot sizes in this triple dot are smaller than the lithographic sizes expected, resulting in smaller dots and larger charging energies. In fact, these dots can be tuned to the few-electron regime and in Chapter 5 we present experiments on a single dot tuned to the one- and two-electron regime.

Figure 4.10 (a) shows a scanning electron micrograph of the triple dot, where we have highlighted 11 out of the 15 gates that are energized in order to define a double quantum dot. In Figure 4.10 (b) we show the measured stability plot of this double quantum dot. Clear Coulomb blockade peaks are observed. As the double dot transitions

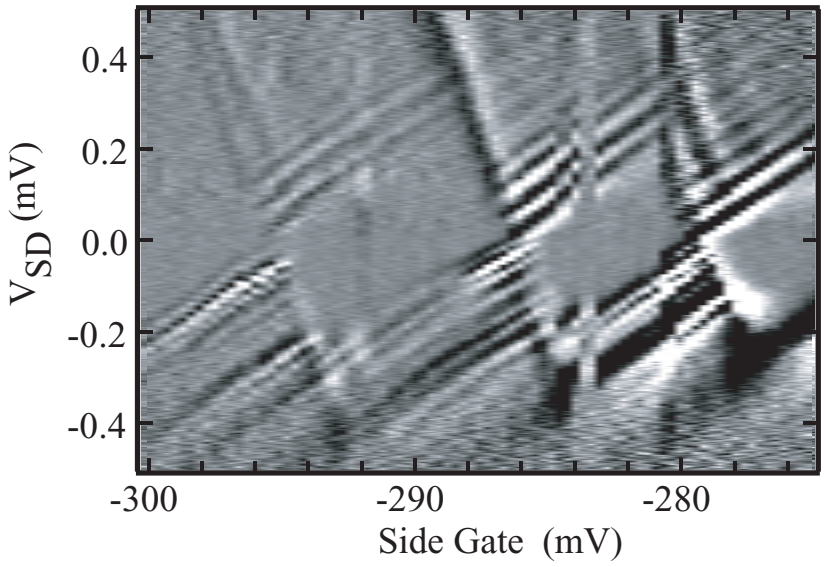

Figure 4.9 Numerical derivative (with respect to the horizontal axis) of the differential conductance of the triple dot acting as one large composite dot. All inter-dot quantum point contacts are set to ~ $2e^2$/h. Dot 3 is completely isolated from lead III. Differential conductance is measured as a function of all six side gates and the dc bias, $V_{SD} = V_I - V_{II}$. The diamonds are Coulomb blockaded regions where current through the triple dot is zero. Lines parallel to the diamonds are excited states of the triple quantum dot.

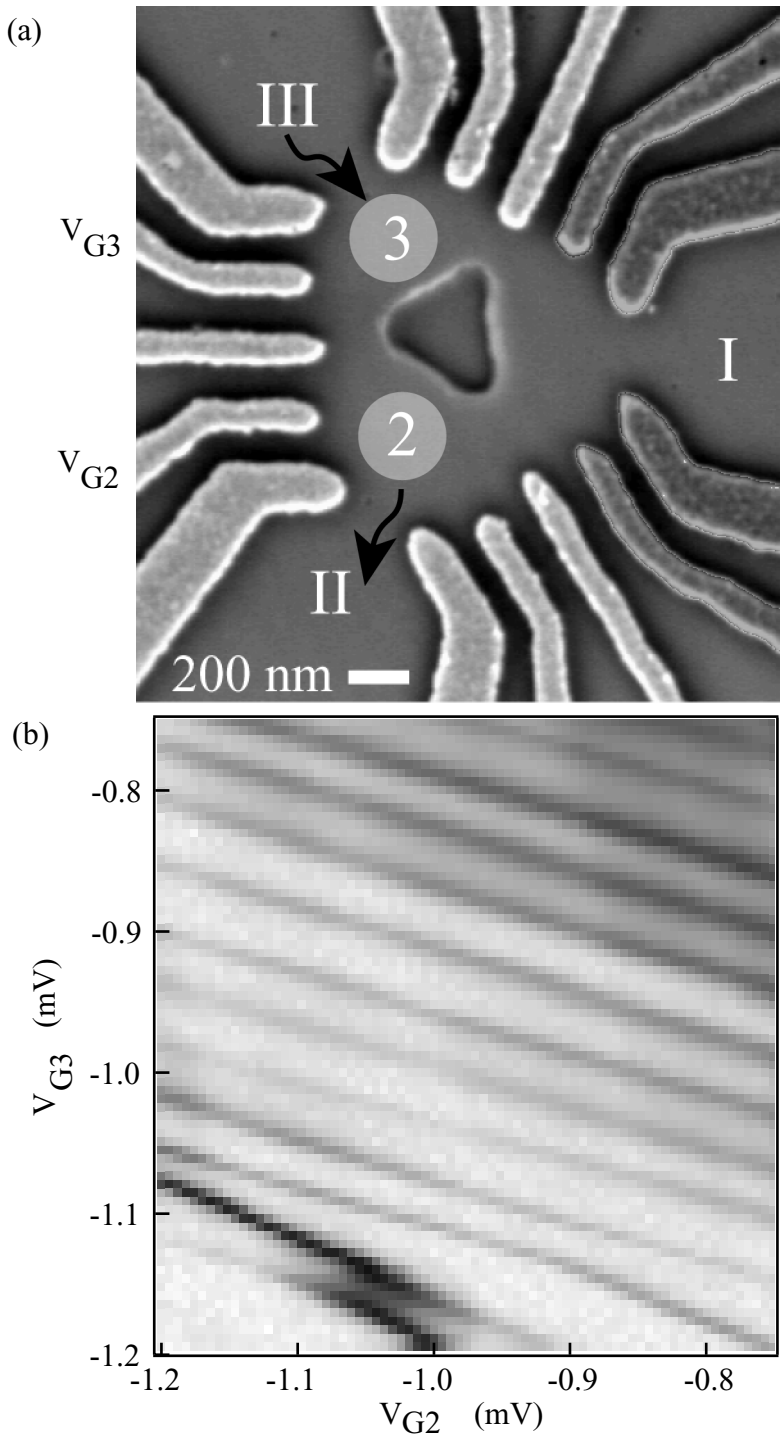

Figure 4.10 (a) Scanning electron micrograph showing the 11 gates (highlighted) that are energized in order to define a double quantum dot. The side gate voltages used in measuring the stability diagram are labeled as V_{G2} and V_{G3}. (b) Stability diagram of the double dot shown in part (a). In the lower left region, weaker coupling due to more negative voltages placed on V_{G2} and V_{G3} results in peak splitting and the appearance of triple points. In the upper right region, the side gate voltages are less negative, allowing for stronger coupling between the two dots and straight diagonal Coulomb blockade lines are observed. In this region, the double dot has merged into one large composite dot.

from weak coupling to strong coupling, the Coulomb blockade peaks transition from curved lines displaying triple points to straight diagonal lines.

4.4.2 Density Functional and Exact Diagonalization Calculations

In this section, we present numerical calculations of the singlet-triplet splitting for a two electron triple quantum dot. This work was performed with Dr. Michael Stopa at Harvard University, using the SETE software package that he developed [60,61].

The spin state of electrons in multiple quantum dot assemblies formed in two dimensional electron gas semiconductor heterostructures is determined by exchange interactions between the electrons and not, generally, by the much smaller magnetic dipole interactions between the spins. In the simplest case of two electrons in two dots (artificial molecular hydrogen) competition between exchange, which favors spin alignment (spin triplet), and tunneling, which delocalizes the electrons and tends [62] to favor spin anti-alignment (spin singlet) can be modulated by a magnetic field and is sensitive to the precise geometric nature of the tunnel barrier separating the two dots [63]. The exchange splitting J is defined as the energy difference between the ground state triplet and the ground state singlet and is crucial to the implementation of various schemes of quantum computation [37].

Numerous recent calculations, motivated by the quantum computation implications of manipulating the exchange interaction, have demonstrated that for double dots, the exchange splitting J(B) as a function of magnetic field is positive for B = 0 but can cross to negative (triplet ground state) as B increases before finally saturating to zero as the magnetic field effectively isolates the two dots [61,62,64]. For the triple dot we

show below that J(B) oscillates between positive and negative several times before decaying to zero. This suggests a competition between the exchange integral and the tunnel coupling that is mediated by the evolving single particle states which are in turn influenced by the magnetic flux that threads the triple dot device.

We study the spin state of the symmetric, tunnel-coupled triple quantum dot presented in the previous section as a function of electron number N, magnetic field B, and the various gate voltages and gate geometries controlling the height and shape of the barriers between the dots. We are particularly interested in the two-electron (N = 2) triple dot system because of its relevance to quantum computation [37]. We study the triple quantum dot in two regimes with two different methods. First, we consider the case of a large number of electrons using a mean-field, density functional theory calculation [60]. This calculation allows for a self-consistent solution that incorporates the realistic device parameters. The triple dot stability diagram, derived in Section 4.2, identifies, in particular, the N = 20 case as similar to the N = 2 case. Specifically, since 18 electrons constitute a filled shell for the triple dot, N = 20 has two valence electrons. We first examine the structure of the magneto-spectrum for the "filled-shell" N = 18 case. It is then of interest to study how the 18 core electrons influence the electronic structure of two valence electrons when we increase N to 20.

The mean-field, density functional theory approach breaks down in the few-electron regime (small electron number N), where electron-electron correlation is significant. Therefore, to investigate the N = 2 triple quantum dot, we extend the exact diagonalization method used to study N = 2 double quantum dots [61] to the three dot case. The exact diagonalization calculation employs the density functional theory results

(the Kohn-Sham states) as a basis only. This method incorporates the full geometric fidelity of the structure while also including the full effects of many-body correlation.

We begin with a calculation of the electronic structure of the triple dot device. Figure 4.11 shows a self-consistent potential profile of the triple dot device performed with density functional theory [60]. We consider the case where the three dots are as nearly "balanced" as possible. This is straightforward for N = 18, where 6 electrons occupy each dot and a spectral gap exists to the next (empty) state. For N = 20, however, it is necessary to set the gate voltages carefully so as to maintain a charge of 20/3 in each dot.

In Figure 4.12 we show the calculated Kohn-Sham energy levels for a single spin species ("spin up") for a triple dot with N = 18 and N = 20 as a function of magnetic field. Note that the dot is strongly isolated from the leads and that the Fermi surface E_F of the N = 18 (N = 20) triple dot lies between the 9^{th} (10^{th}) and the 10^{th} (11^{th}) levels. The resemblance to the Fock-Darwin spectrum [65] is evident. The spectrum is predominantly that of three isolated dots, each approximately parabolic, nearly degenerate except for a tunnel splitting. The tunnel coupling between the dots is small and is of the order of the splitting between the sets of three states at B = 0. It is interesting that there is no evident effect of the flux threading the dot ring in these results. For N = 20 the spectrum is quite different due to the location of the dot Fermi level within a group of three (six, including spin) levels. The nearly degenerate levels are influenced by small changes in B which further affects the occupancies. These shifts in occupancy thereupon change the self-consistent potential. So, while the gates are set at B = 0 to "balance" the three dots, the magnetic field breaks this symmetry and produces charge redistribution. An additional

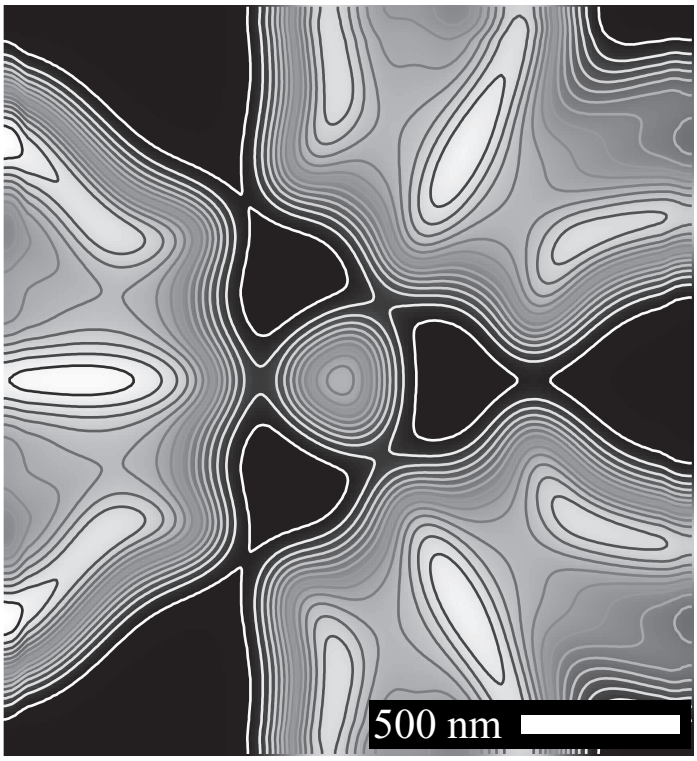

Figure 4.11 Potential contours of the triple quantum dot calculated from a self-consistent simulation of the full 3D structure of the device shown in Figure 4.8.

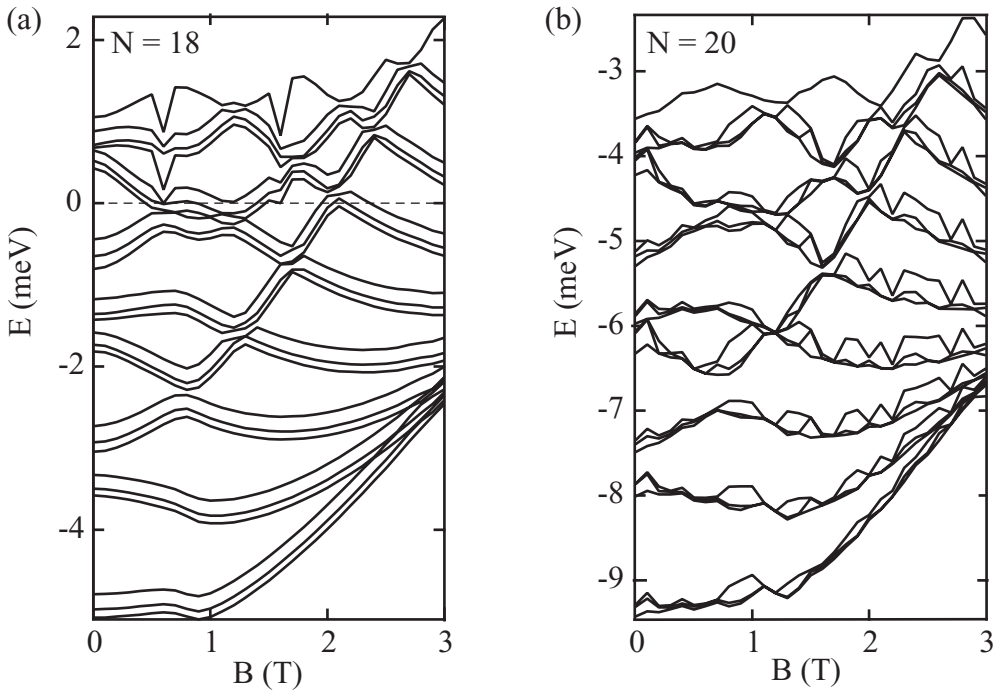

Figure 4.12 Kohn-Sham energy levels for triple dot (spin up) with (a) N = 18 electrons and (b) N = 20 electrons. For N = 18, each electron has a filled Fock-Darwin "shell" of 6 electrons and so the Fermi level is in a gap. For N = 20, fluctuations of the self-consistent structure occur as B slightly modifies the Fermi surface states. Points calculated every 0.1 T.

effect, which is an anomaly of mean field theory, is that levels tend to stick together (unless there is a gap at the Fermi surface) so that fractional occupancy can produce a charge distribution that best minimizes the electrostatic energy.

We now focus on the N = 2 triple dot and examine the exchange energies as a function of magnetic field B. We maintain the gate voltages such that the triple dot is balanced and 2/3 of an electron is resident in each dot. In order to reduce the electron number to N = 2 it is necessary to make the surface gate voltages considerably more negative and shrink the area of the dots. The Kohn-Sham level structure for the N = 2 triple dot, shown in Figure 4.13 (a), reflects this smaller size, as is evident by the spacing between the lowest three states and the next six states (s and p, respectively, in the Fock-Darwin spectrum) being greater than in the larger N cases.

In order to understand the level structure, it is instructive to diagonalize the single particle Hamiltonian for the triple dot in the tight-binding basis. We assume that the dots are identical with energy ε_0 and connected with tunneling coefficient t, as shown in Figure 4.13 (b). The Hamiltonian is

$$H = \begin{bmatrix} \varepsilon_0 & -t & -t \\ -t & \varepsilon_0 & -t \\ -t & -t & \varepsilon_0 \end{bmatrix} \tag{4.20}$$

The eigenvalues of H are $E_0 = \varepsilon_0 - 2t$ and $E_1 = \varepsilon_0 + t$, the latter of which is doubly degenerate. The (un-normalized) eigenfunctions, shown in Figure 4.13 (b), are: (1,1,1), (1,-1/2,-1/2) and (0,1,-1). The splitting between the lowest level in Figure 4.13 (a) and the ensuing degenerate pair is 3t and is approximately 0.4 meV.

As the magnetic field is turned on, level oscillations that are not apparent in the large N cases [Figure 4.12] begin to occur. We attribute these fluctuations, most notably

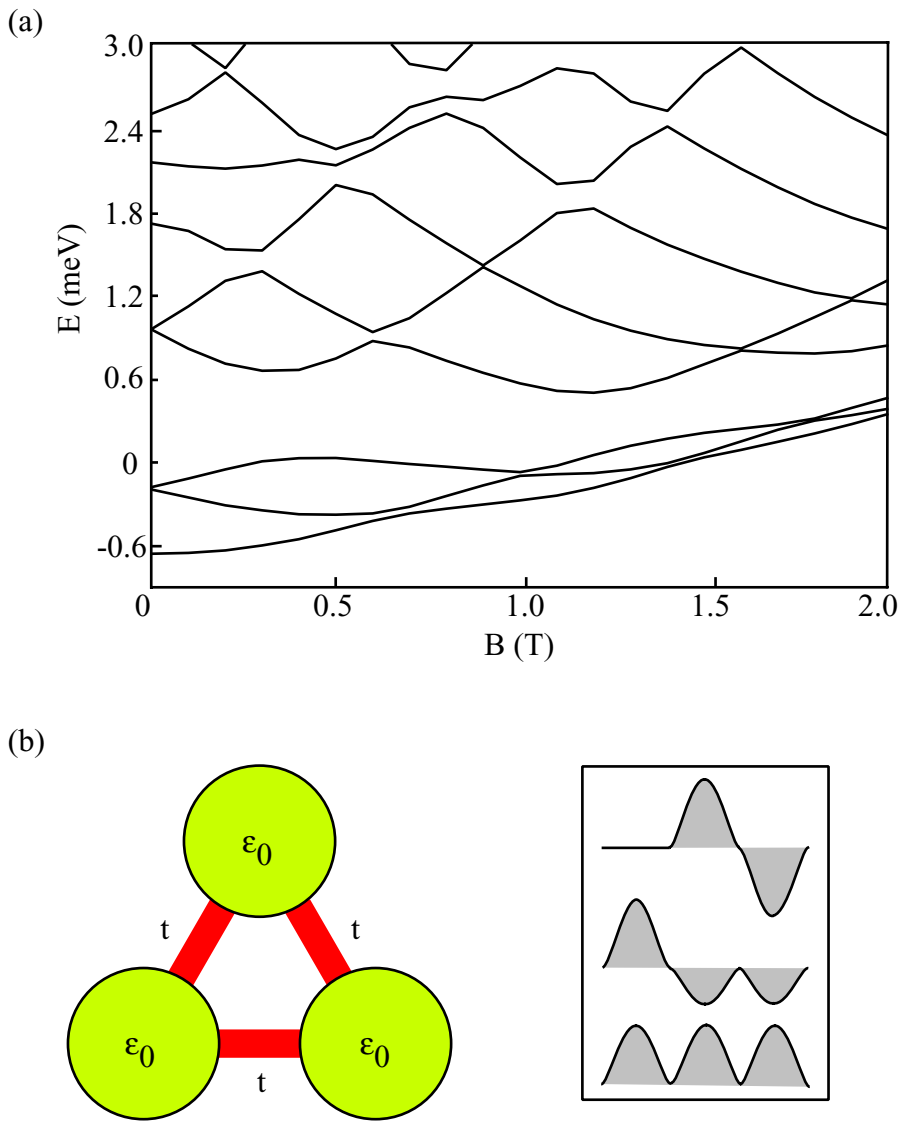

Figure 4.13 (a) Kohn-Sham energy levels for the N = 2 triple dot. Splitting, at B = 0, between first level and second pair is 3t. Note that level 2 oscillates between levels 1 and 3 with the same behavior as the oscillation of J(B) seen in Figure 4.14 (a). (b) Schematic of tight-binding model of three dots in a ring with eigenfunctions (1,1,1), (1,-1/2,-1/2) and (0,1,-1).

the oscillation of level 2 back and forth between levels 1 and 3, to the addition of flux quanta through the ring formed by the three dots. A major consequence of this variation is the behavior of the singlet-triplet splitting J(B) for the N = 2 triple dot. The singlet-triplet splitting J(B) is calculated from an exact diagonalization calculation which uses the Kohn-Sham states of Figure 4.13 (a) as a basis. Figure 4.14 (a) shows that J(B) begins positive and then changes back and forth between positive and negative several times. This is strikingly different from the double dot case, whose representative calculations of J(B) are illustrated in Fig. 4.14 (b). For N = 2 double dots, the singlet nature of the B = 0 ground state gives way to a transition to a triplet ground state at finite B [61,62,64]. Physically, spin-alignment (triplet) is favored by the exchange integral, as in the case of Hund's rules for atoms, and spin anti-alignment (singlet) is favored by tunneling which permits double-occupancy through delocalization. The action of the magnetic field is to compress the wavefunction overlap in the saddle point between the two dots. This enhanced overlap increases exchange (integral) while leaving the tunneling coefficient essentially unaffected. This therefore constitutes an explanation of the double dot B-dependent crossover of J. For triple dots, the behavior of J(B) is more complicated.

A basic explanation of the fluctuating triple dot J(B) is as follows. The lowest state in Figure 4.13 (a) can contain two electrons, due to spin degeneracy. When the second orbital descends to near degeneracy with the first (at B ~ 0.6 T, for example), the additional orbital degeneracy allows spin alignment, in the form of Hund's rule. Therefore in these regimes the triplet is favored. While a more thorough explanation in terms of the competition between delocalization and exchange is desired, it is clear that the driving mechanism for J(B) oscillation is the influence that the threaded magnetic

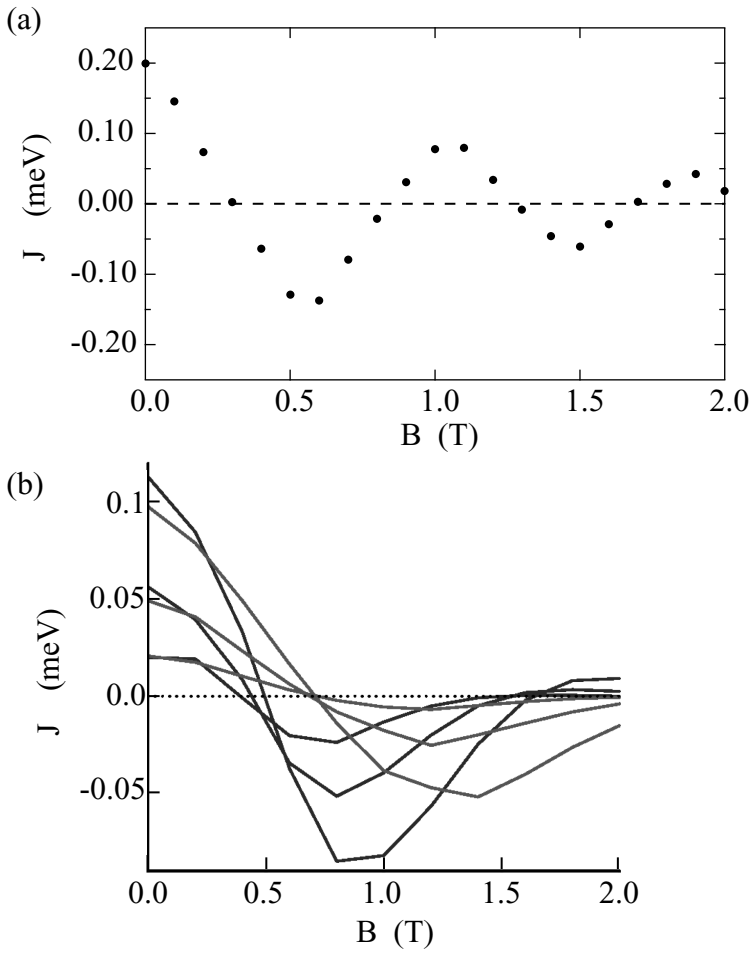

Figure 4.14 Singlet-triplet splitting J(B) as a function of magnetic field for (a) triple and (b) double dot calculated from full exact diagonalization method for N = 2. Note that, in contrast to the double dot case (plotted here for a typical variety of gate patterns and tunnel coupling strengths) J(B) for the triple dot exhibits several oscillations while it is damped by increasing localization of the eigenstates within the individual dots by the magnetic field.

field exerts on the evolving basis states.

In conclusion, we have used density functional theory and exact diagonalization, formulated on a density functional basis, to investigate the exchange energy in a triple quantum dot. We show that the effective single particle spectrum (the Kohn-Sham levels) for many electrons (~20) evolves, as a function of applied magnetic field B, in the form of a triply degenerate (six-fold degenerate if spin is included) Fock-Darwin spectrum. The single particle spectrum is not influenced by the threading magnetic field. We have also shown an oscillatory structure to J(B) for the N = 2 triple quantum dot which contrasts strikingly with that of the double dot case.

4.5 Conclusions

Triple quantum dots are new types of artificial molecules, compared to the previously studied linear coupled quantum dots. In this chapter, we have presented two different configurations of a triple quantum dot system. We have shown that an asymmetric configuration results in a bias-dependent current suppression, making a triple dot a promising candidate as a single-electron rectifier in future single-electron tunneling device circuits. Furthermore, triple dots can be used as building blocks of a two dimensional triangular array of qubits for solid state quantum computation. We have also presented numerical calculations that show that the triple dot exchange interaction gives rise to a quasi-periodic fluctuation of J with magnetic field, which we attribute to periodic variations of the basis states in response to changing flux quanta threading the triple dot.

An interesting topic that may be explored in future experiments on triple quantum dots is that of geometric spin frustration [66]. Certain lattice geometries may result in

frustration of the spin-spin interactions. For nearest neighbor antiferromagnetic coupling of spins in the triple dot molecule, the system is unable to satisfy all pairwise interactions. The ground state energy of the triple dot molecule is the same for six different spin configurations, where two of the three spins must point in the same direction, resulting in geometric spin frustration. Typically, it is difficult to study geometric spin frustration because defects and three-dimensional inter-coupling normally act to relieve the frustration in real materials.

Artificially engineered two-dimensional structures, such as the triple dot of Figure 4.8, will provide ideal systems in which to study geometric spin frustration. In the triple dot system, exchange interactions can be described by an effective spin Hamiltonian $H = -\left(J_{12}\mathbf{S_1}\cdot\mathbf{S_2} + J_{13}\mathbf{S_1}\cdot\mathbf{S_3} + J_{23}\mathbf{S_2}\cdot\mathbf{S_3} \right)$. $\mathbf{S_i}$ is the spin on dot i and J_{12}, J_{13}, and J_{23} are negative. The Cr:Au gates of the three inter-dot quantum point contacts are fully tunable, and allow control over each individual exchange coupling J_{ij}. Therefore, we can perform transport measurements of a frustrated triple dot ($J_{12} = J_{13} = J_{23}$) and then relieve the frustration by tuning one exchange coupling to zero. Aside from conventional conductance measurements, including spin blockade spectroscopy using spin polarized leads [67], we believe measurements of the thermopower of the triple dot molecule may reveal spin frustration characteristics [68]. Thermopower of quantum dots in the Coulomb blockade regime has been studied theoretically [69] and has already been used as an effective spectroscopic tool [70].

V

MULTI-PEAK KONDO EFFECT

5.1 Overview

Semiconductor quantum dots are tunable systems and can serve as probes of strongly correlated electron behavior. In this chapter, we use a few-electron quantum dot to study the Kondo Effect [71]. The Kondo effect is one of the most fascinating many-body problems in condensed matter physics [72]. We present results of transport measurements through a single quantum dot occupied by one or two electrons (N = 1 or N = 2) which, in both cases, exhibit sharp peaks in the differential conductance beyond the linear regime. Non-linear measurements of transport through Coulomb blockaded quantum dots have become a standard method for investigating the excited states of dot electrons. Frequently-observed inelastic co-tunneling lines in Coulomb diamonds [73] are a signature of a virtual exchange of electrons with two Fermi surfaces (the leads) which produce a preferential electron flow from source to drain. This phenomenon is, at least, the lowest order fundamental process from which arises the Kondo effect.

Analysis of the temperature dependence and the peak splitting due to a magnetic field indicate that the observed co-tunneling lines in our measurements represent the fully coherent Kondo effect. We analyze the revealed level spacing in terms of a disordered, quasi-1D structure of the dot and indicate that the unusually low-energy excitations are an expected characteristic of such systems. Similar features in transport through 1D nanotube devices have already been observed [74].

In Section 5.2 we give a brief review of the Kondo effect in quantum dots. In Section 5.3 we describe the few-electron quantum dot device, including the integrated quantum point contact charge sensor. The charge sensor allows us to determine the absolute charge state (N = 1 or N = 2) of the quantum dot. Section 5.4 presents the non-linear transport measurements showing the Kondo resonances.

5.2 The Kondo Effect

The Kondo effect arises when the degenerate or nearly degenerate states of an isolated electron system, which are not coupled through any direct interaction, acquire an effective coupling, and thereby hybridize, via the virtual exchange of electrons with one or more neighboring Fermi surfaces [72]. The simplicity of the conditions demanded by the Kondo effect contributes to its ubiquity in electron systems as well as to the variety of phenomena that are distinct manifestations of Kondo physics. The initial experimental puzzle which required the Kondo effect for its elucidation concerned the diverging low temperature resistivity of metals doped, intentionally or otherwise, with 3d transition metal impurities possessing a local magnetic moment [75]. The physics of the Kondo effect was also able to be applied to resonant transport through tunnel barriers with magnetic impurities [76-78]. A quantum dot, with non-zero spin, behaves essentially as a localized magnetic impurity coupling two Fermi seas (the source and drain leads). By contrast to the case of impurities in metal, however, the observation of Kondo physics in semiconductor quantum dots, which are artificial atoms whose coupling, spin and energy parameters are subject to delicate control [44], dramatically widened the classes of Kondo behavior which could be observed and explained [79-86].

The Anderson model [87] can be used to describe the quantum dot as a single magnetic impurity, and is schematically shown in Figure 5.1. The quantum dot has a single spin-degenerate state with energy ε_0 that is less than the Fermi energy E_F of the leads. This state is occupied by a single electron with tunneling rate Γ/h. The large charging energy E_C prevents a second electron from entering the dot. Typically, the quantum dot is in Coulomb blockade and no transfer of electrons can occur. However, if coupling to the leads is large, higher-order co-tunneling events can take place. Such virtual tunneling events may lead to a spin flip, as shown in Figure 5.1. The coherent superposition of these tunneling events results in an average quantum dot spin of zero, even though the quantum dot contains a single electron. The spin of the single localized electron in the quantum dot is effectively screened by the electrons in the leads. Stated differently, the electron in the quantum dot and the electrons in the leads form a many-body spin-singlet state. This spin-singlet couples the source to the drain and gives rise to a narrow peak at E_F in the density of states of the quantum dot. This leads to a conductance resonance for the quantum dot, which is observed as a peak in the differential conductance dI/dV_{SD} and as enhanced conductance within a Coulomb blockade valley. Note that, in contrast to the increased *resistivity* due to the Kondo effect for impurities in metals, the Kondo effect in quantum dots leads to an increase in *conductance*.

The characteristic energy scale of the Kondo effect k_BT_K is the binding energy of the many-body spin-singlet state that is formed [72]. Written in terms of the parameters introduced in the Anderson model, the Kondo temperature T_K is [88,89]

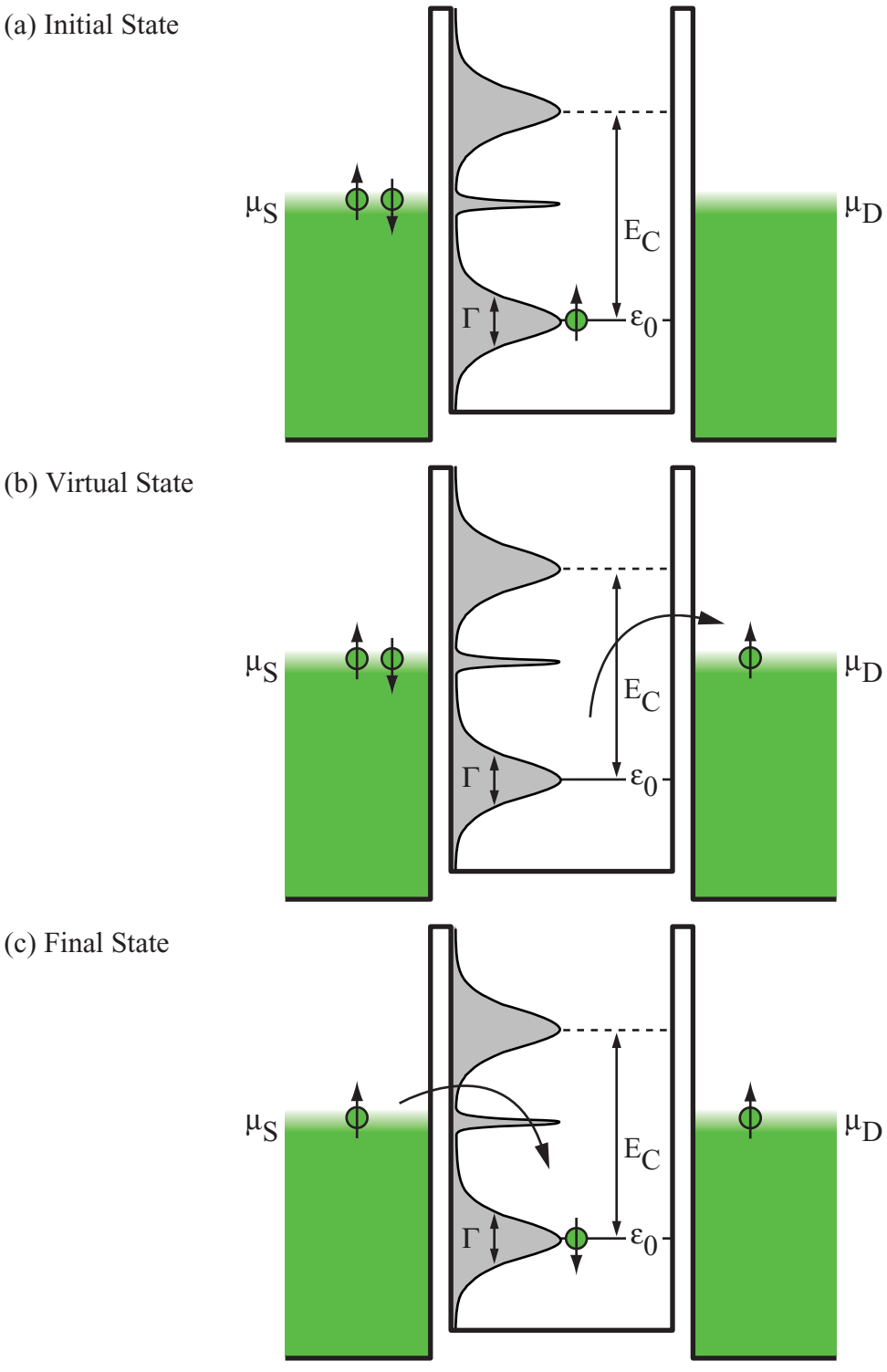

Figure 5.1 Schematic diagram of the Anderson impurity model showing the energy profile of a quantum dot connected to source and drain leads. The quantum dot has a single spin-degenerate state with energy ε_0 that is less than the Fermi energy E_F of the leads. The charging energy is E_C. The quantum dot density of states is shown in gray. Resonances at the discrete energy states are broadened by Γ. A narrow peak at E_F develops due to the Kondo effect. A virtual spin-flip tunnel process is shown: (a) (initial state) the quantum dot contains a spin up electron; (b) (virtual state) the electron may tunnel out to the drain within a time $\Delta t \sim h/E_C$; (c) (final state) a spin down electron tunnels in from the source.

$$T_K = \frac{\sqrt{\Gamma E_C}}{2k_B} \exp\left[\frac{\pi\varepsilon_0\left(\varepsilon_0 + E_C\right)}{\Gamma E_C}\right] \tag{5.1}$$

The Kondo temperature varies across the Coulomb valley. At the center of the valley, with $\varepsilon_0 = -E_C/2$, the Kondo temperature is a minimum, given by

$$T_{K,0} = \frac{\sqrt{\Gamma E_C}}{2k_B} \exp\left[-\frac{\pi E_C}{4\Gamma}\right] \tag{5.2}$$

Equation (5.1) can be rewritten as [90]

$$T_K = T_{K,0} \exp\left[\frac{\pi\Delta\varepsilon_0^{\,2}}{\Gamma E_C}\right] \tag{5.3}$$

where $\Delta\varepsilon_0 = \varepsilon_0 + E_C/2$ is the energy difference from the center of the valley. In terms of gate voltage V_G, $\Delta\varepsilon_0 = \alpha e(V_G - V_{G0})$, where $\alpha = C_G/C_\Sigma$ is the "capacitive lever arm" (see Section 2.4) and V_{G0} is the value of the gate voltage at the center of the valley. Therefore, the Kondo temperature T_K varies as $\exp(V_G^2)$.

In a parallel magnetic field $B_{\|}$, the spin degeneracy of the single-particle state is lifted by Zeeman splitting, and the single state at ε_0 splits into two states separated by the Zeeman energy $g\mu_B B_{\|}$, where g is the Lande g factor and μ_B is the Bohr magneton. The Kondo peak in the density of states also splits, and can be observed as two peaks in dI/dV_{SD} located at $eV_{SD} = \pm g\mu_B B_{\|}$ [91,92].

5.3 Realization of a One and Two Electron Quantum Dot

Figure 5.2 (a) is a scanning electron micrograph of the quantum dot device. A single quantum dot is defined using six Cr:Au surface gates (highlighted in the figure) and a 30 nm deep ion-etched trench on a modulation doped GaAs/$Al_{0.3}Ga_{0.7}As$

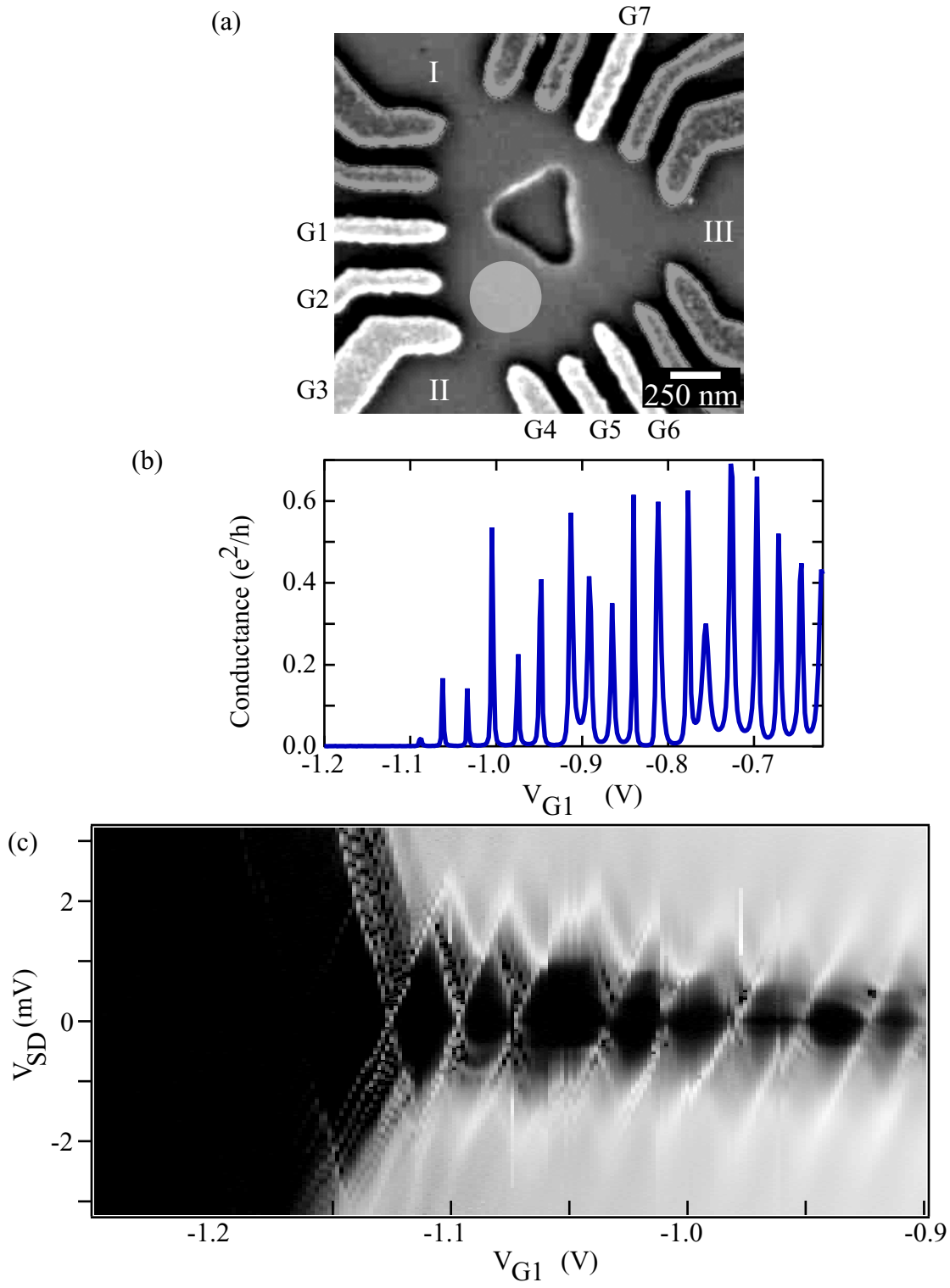

Figure 5.2 (a) Scanning electron micrograph of the quantum dot device. Light gray regions are Cr:Au surface gates. Only the highlighted gates are used in these measurements. The center region is a 30 nm deep ion-etched trench. (b) Coulomb blockade oscillations as a function of side gate voltage V_{G1}. (c) Gray-scale plot of the differential conductance dI/dV_{SD}. Light regions correspond to enhanced conductance.

heterostructure containing a two-dimensional electron gas 52 nm below the surface. Low temperature Hall measurements determined the 2DEG sheet density $n_s = 3.8 \times 10^{11}$ cm^{-2} and mobility $\mu = 460\,000$ cm^{2}V^{-1}s^{-1}.

The device was cooled in a ^{3}He/^{4}He dilution refrigerator, and the differential conductance through the quantum dot was measured between leads I and II by adding a small a.c. excitation voltage to a d.c. source-drain bias V_{SD} and recording the current with a current preamplifier and lock-in amplifier. A large negative voltage was placed on gate G6 to suppress any tunneling through the third terminal. All measurements, except those in Figure 5.4 (a), were performed at the base temperature of 40 mK. Figures 5.2 (b) and 5.2 (c) show typical Coulomb blockade conductance oscillations and Coulomb diamonds for the quantum dot in the few-electron regime. Our geometry allows us to tune the number of electrons in the quantum dot from approximately 20 electrons down to zero electrons. Furthermore, we observe clear signatures of a shell structure [93] in the quantum dot, including an alternation in the Coulomb blockade peak heights for the first few electrons entering the dot, different areas for each Coulomb diamond, and odd-even signatures at zero source-drain bias.

By placing a large negative voltage on both gates G5 and G6, we can reduce the size of the quantum dot. Self-consistent electronic structure simulations [60] of the full three-dimensional structure of our dot, including wafer profile, donor layer disorder, and the device surface gate pattern, show that the potential profile for the 2DEG electrons can become long and narrow [Figure 5.3 (a)]. Our device has a nearby gate G7 that forms a quantum point contact against the center etched trench. Measuring the conductance through leads I and III, we find that the quantum point contact shows clear conductance

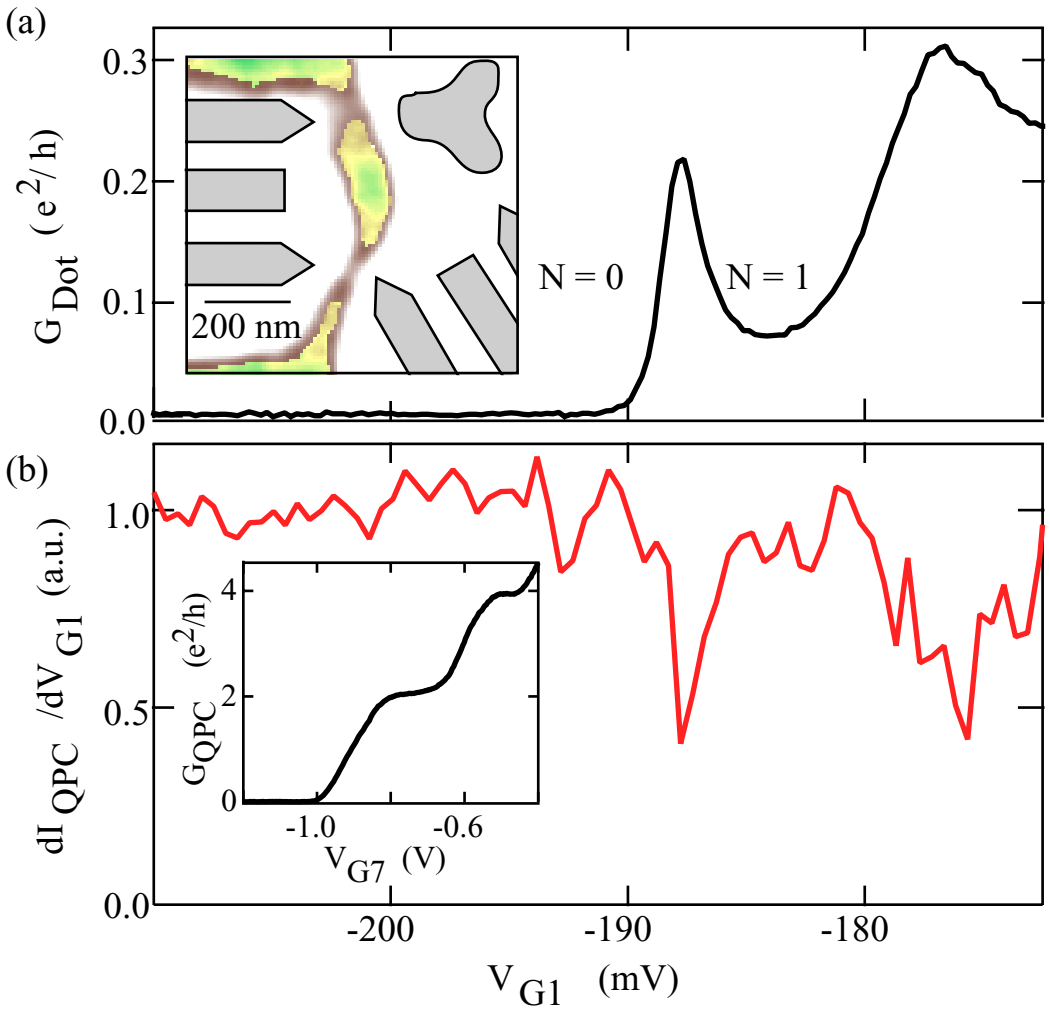

Figure 5.3 (a) Coulomb blockade conductance of the quantum dot, when tuned down to the one and two electron regime. *Inset*: Potential profile from a self-consistent electronic structure simulation showing the resulting quasi-1D shape of the quantum dot. The center of the dot is at ~ -4 meV relative to the Fermi level of the 2DEG, with QPC barrier heights of ~ 4 meV. (b) Simultaneously measured differential conductance dI_{QPC}/dV_{G1} through a nearby QPC biased below the first conductance plateau. The QPC acts as a charge sensor, showing a drop in dI_{QPC}/dV_{G1} as the number of electrons on the dot changes. Absence of additional dips reveals the absolute number of electrons on the dot, starting at N = 0. *Inset*: quantized conductance of the QPC.

plateaus, as shown in the inset to Figure 5.3 (b). Biasing the point contact below the first conductance plateau, where the slope is the steepest, allows it to act as a very sensitive charge sensor for the quantum dot [94]. As the quantum dot goes through a Coulomb blockade peak, a sharp decrease in the point contact conductance dI_{QPC}/dV_{G1} is observed. Figures 5.3 (a) and 5.3 (b) show the conductance through the quantum dot and dI_{QPC}/dV_{G1} measured simultaneously. The absence of further Coulomb blockade oscillations in the quantum dot conductance or dips in the point contact conductance as V_{G1} is made more negative indicates that the quantum dot is empty of electrons. Using the quantum point contact charge sensor, we are able to identify the N = 1 and N = 2 transport Coulomb diamonds in which we observe features that, as we shall show, are manifestations of the Kondo effect. In the rest of the measurements presented here, G7 is turned off and lead III is left floating.

In most quantum dots, as the size is reduced using the side gates, the large negative voltage applied to these gates makes the tunnel barriers to the source and drain more opaque. As a result, transport in the few-electron regime, in particular, is difficult to measure. Here, our quasi-1D dot geometry allows us to maintain strong coupling to the leads even in the one and two electron regime, as signified by the large (> 0.2 e^2/h) Coulomb blockade peaks. In addition, we employed the technique of cooling down the device with the gates at positive bias [95]. This effectively lowers the ionized donor concentration N_{ion} in the vicinity of the dot and our simulations show that the lowered N_{ion} enhances the spread and lead-connectivity of the low lying wave functions.

In Figure 5.4 we plot the temperature dependence and in-plane magnetic field dependence of the conductance for the one and two electron dot. Our N = 1 quantum dot

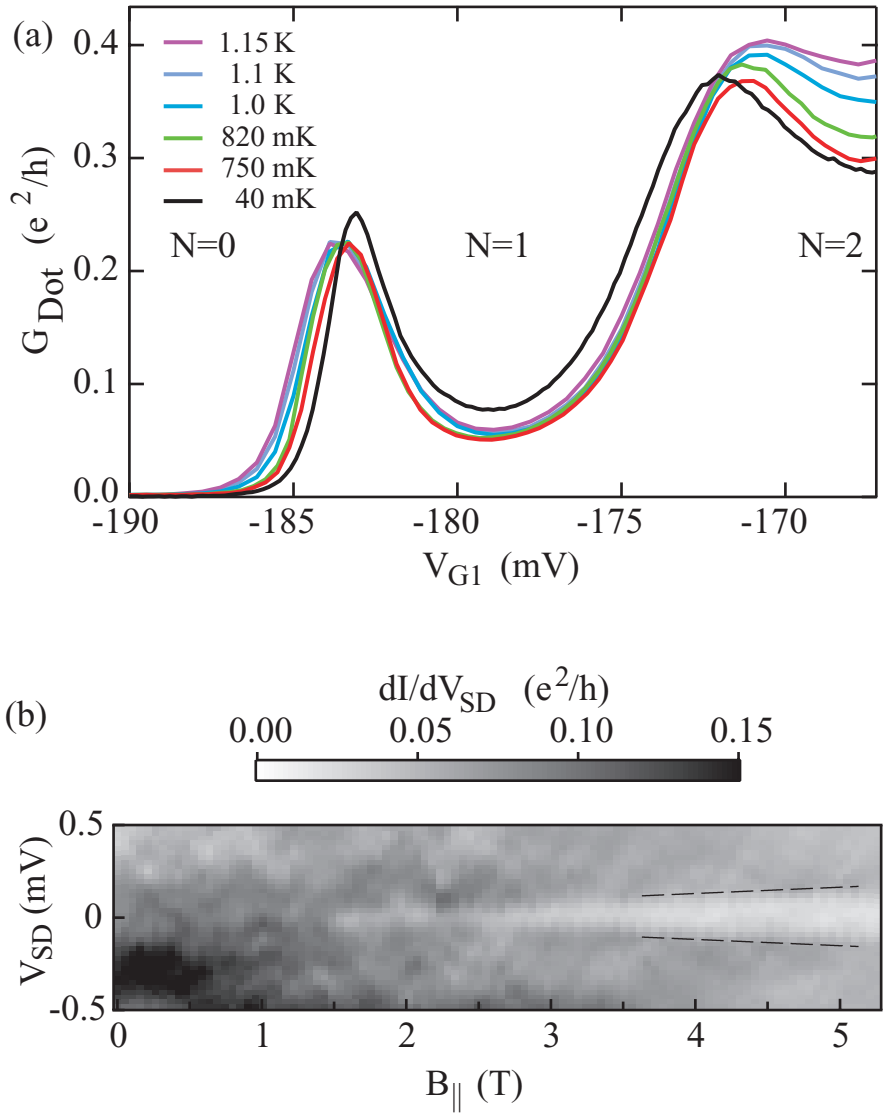

Figure 5.4 (a) Conductance versus side gate voltage V_{G1} for different mixing chamber temperatures. (b) Differential conductance as a function of source-drain voltage and in-plane magnetic field (with V_{G1} tuned to the center of the N = 1 valley) showing the Kondo peak splitting. Dashed lines are linear fits of the peaks to $\pm g\mu_B B_{||}$.

is an experimental realization of the canonical example of the Kondo effect with just a single isolated spin. From Equation (5.1), we see that the Kondo temperature T_K depends sensitively on the coupling to the leads. Figure 5.4 (a) shows that with decreasing temperature, the conductance in the single electron valley increases, whereas the trend is reversed for the two electron valley, as expected. Furthermore, we observe that the conductance peaks shift toward the center of the N = 1 valley as the temperature is lowered, in agreement with theoretical predictions for the Kondo effect [89,91,92]. Applying a parallel magnetic field $B_{\|}$ allows us to measure the Kondo peak splitting [91,92]. Figure 5.4 (b) shows the differential conductance as a function of V_{SD} and $B_{\|}$ at the center of the N = 1 valley. We find that above a critical value of in-plane magnetic field B_C = 1.45 T, the Kondo peak begins to split into two peaks located at $eV_{SD} = \pm g\mu_B B_{\|}$. This splitting allows us to determine the g factor g = 0.32 for our quantum dot. The value of the critical magnetic field B_C required for Kondo peak splitting gives us an estimate of the Kondo energy scale $k_B T_K \sim g\mu_B B_C \sim 27$ μeV. A critical magnetic field below which no splitting occurs is predicted by theory [96], and has been measured in other lateral quantum dots [90,97,98].

5.4 Multi-Peak Kondo Effect

Figure 5.5 shows the differential conductance through the quantum dot as a function of V_{SD} and V_{G1} in the one and two electron regime. Absence of diamonds at high bias and more negative side gate voltage gives further evidence of the absolute occupancy of the dot (N = 0, 1 and 2). The transport spectroscopy shown here has many interesting features. We find several horizontal lines within the Coulomb diamonds.

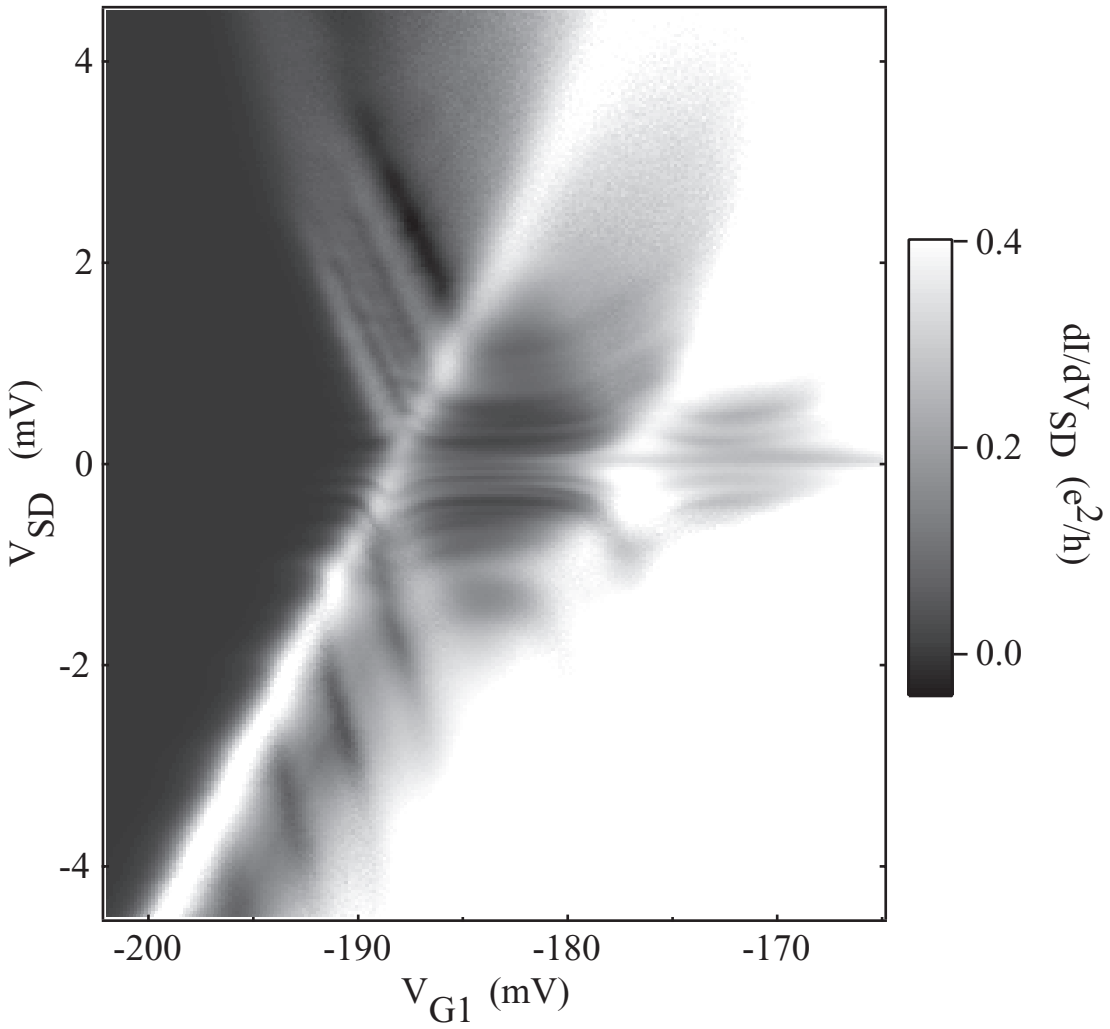

Figure 5.5 Differential conductance as a function of source-drain voltage and side gate voltage V_{G1}. Left region is N = 0, center diamond is N = 1, and right diamond is N = 2. Sharp horizontal conductance peaks are observed within the N = 1 and N = 2 diamonds. Also observed are regions of negative differential conductance above and below the N = 1 diamond.

These features form peaks in dI/dV_{SD} rather than steps. This is strong evidence of Kondo behavior since the Kondo effect relies on tunnel coupling of two (possibly degenerate) states with a Fermi surface or surfaces such that, within the natural level width, the levels have access to both occupied and unoccupied states, i.e. the levels are pinned to the Fermi surface(s). A multi-peak Kondo effect where one Fermi surface is pinned to an excited state (and the other to the ground state) has been predicted theoretically [99,100]. The conductance peaks in Figure 5.4 are found to be parallel and independent of V_{G1}, as expected [99,100]. To observe multiple Kondo peaks, the Kondo energy k_BT_K should be comparable to or larger than V_{SD}. In our quantum dot, the Kondo energy is expected to be enhanced by the presence of multiple levels in the quantum dot. With k_BT_K of 27 μeV as our single level Kondo energy, and a single additional level at 145 μeV, we obtain using Equation (3) in Ref. [99] an enhanced k_BT_K equal to 300 μeV.

We begin a closer analysis of Figure 5.5 with the N = 2 diamond, corresponding to a Helium artificial atom. We observe four horizontal peaks in the differential conductance, symmetrically situated, with two peaks above and two peaks below $V_{SD} = 0$. Horizontal features within a Coulomb blockade diamond at a source-drain bias $V_{SD} = \Delta/e$ are associated with transport through an excited state of energy Δ. The four horizontal peaks occur at $\Delta_1 = \pm 105$ μeV and $\Delta_2 = \pm 285$ μeV. We infer that the ground state for the N = 2 quantum dot (with $B_{\|} = 0$) is a singlet, because no zero-bias Kondo peak is observed. While the singlet has no Kondo effect, the triplet S = 1 typically has a lower T_K than a spin-½ system. However, for an even N system it has been demonstrated [85] that near a degeneracy of the singlet and triplet (induced by, say, a magnetic field) a sharp increase of the Kondo temperature results. We therefore propose that the peaks at

± 105 μeV and ± 285 μeV result from the Kondo coupling of the first and second excited-state triplet with the ground state singlet. In other words, the singlet-triplet degeneracy is brought about *modulo* the source-drain bias.

In the N = 1 diamond of Figure 5.5, we observe several peaks. In addition to a zero-bias conductance peak, associated with the single-electron Kondo effect, we find additional peaks spaced by roughly 145 μeV. These peaks correspond to the excitation spectrum of the quantum dot. The fabrication of a single electron dot still appreciably connected to the leads and possessing an excitation spectrum as small as this is non-trivial. The nominal 2DEG density in this heterostructure is $n_s = 3.8 \times 10^{11}$ cm^{-2}. Our modeling shows that with this density of ionized donors and the given geometry of the gates, the gate voltages required to deplete the dot down to one or two electrons would result in a deep, isolated potential depression with a level spacing greater than 1 meV. In these experiments, we have artificially reduced the ionized donor density in the region of the dot by cooling the device down with the gates energized at positive bias. Although we cannot measure the resultant local ion density directly, calculating the electronic structure over a range of 1.5×10^{11} cm^{-2} $\geq n_s \geq$ 0.25×10^{11} cm^{-2} results in a level spacing from 500 μeV down to around 200 μeV. The levels are affected by the particular gate voltages and also the addition of discrete donors (as opposed to jellium) to the calculation. While the donor distribution cannot be known for every device with precision, the success of the model in obtaining consistent excitation energies, even in such a low density regime, is significant. We note finally that recent measurements of nonlinear transport in nanowires exhibit comparable “Kondo stripes” in the Coulomb blockade diamond and a similar explanation has been considered [101].

Figure 5.6 (a) shows the differential conductance through the quantum dot as a function of V_{SD} and V_{G1} at a parallel magnetic field of 3.2 T and 5.2 T. We find that, in addition to the splitting at zero-bias, splitting is also found at non-zero bias, roughly at the locations of the peaks at zero magnetic field. Further indication that these peaks are caused by the Kondo effect is found from the peak splitting behavior. It has been predicted [102] that the peak splitting Δ_K, defined as half the separation between the positions of the positive and negative peaks, is proportional to $\log(1/T_K)$. The Kondo temperature T_K varies as $\exp(V_G^2)$, where V_G is the side gate voltage, as shown in Equation (5.3). Therefore, the peak splitting Δ_K is expected to vary quadratically with gate voltage. Figure 5.6 (b) shows the peak splitting Δ_K as a function of the side gate voltage for three representative peaks at zero, positive, and negative source-drain bias and $B_{\|} = 3.2$ T. We find that the peak splitting does indeed vary quadratically with gate voltage at both zero and finite source-drain bias. The fact that each parabola has a different curvature can be explained by the difference in the energy and tunneling rates of the different quantum dot states.

Our measurements on a small quasi-1D lateral quantum dot strongly coupled to its leads revealed a multi-peak Kondo effect in the one and two electron regime. Electronic structure simulations for our dot, which include the full 3D structure of the device, show that the shape of the quantum dot gives rise to low-energy excited states. These excited states are coupled to the leads via a Kondo resonance, giving rise to the observed Kondo stripes within the Coulomb blockade diamonds.

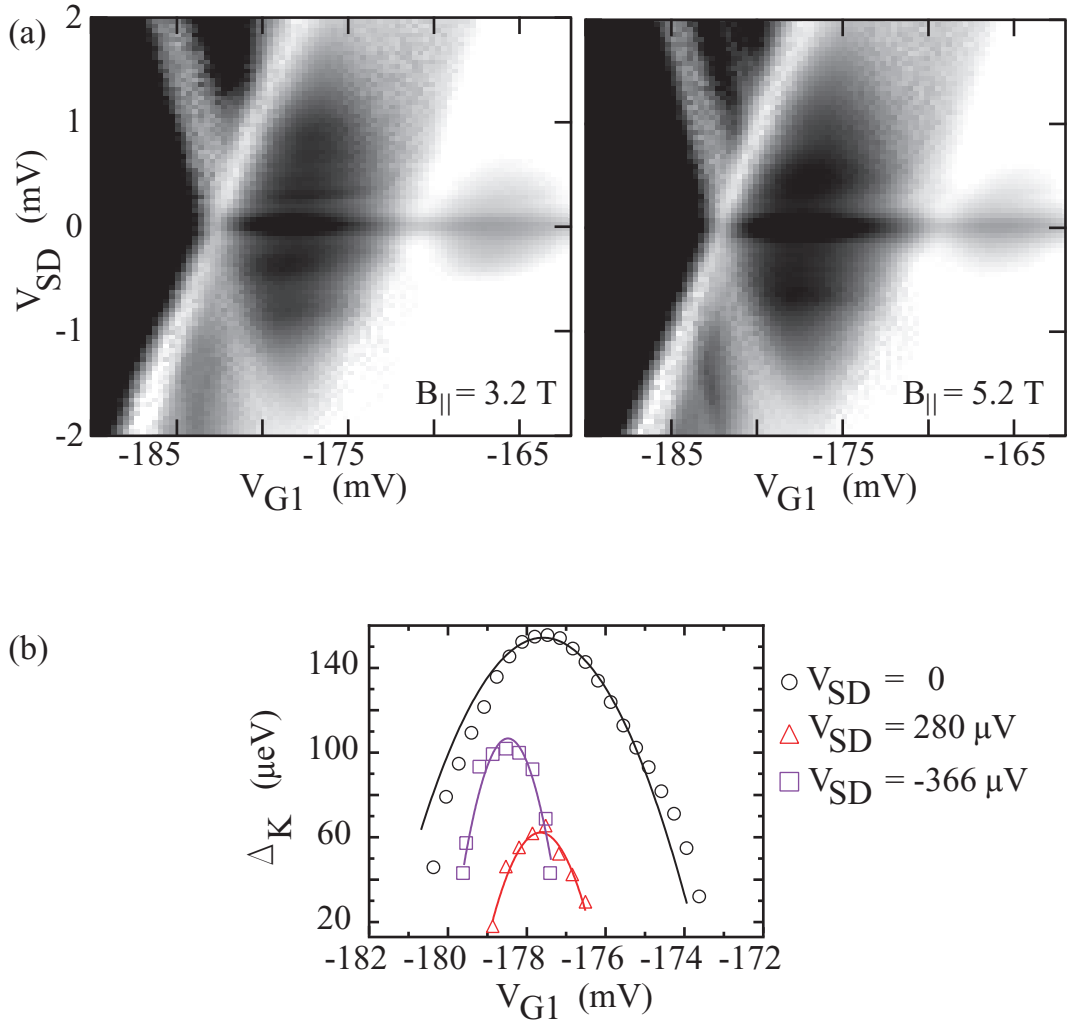

Figure 5.6 (a) Differential conductance as a function of source-drain voltage and side gate voltage V_{G1} with (left) $B_{||}$ = 3.2 T and (right) $B_{||}$ = 5.2 T. Light regions correspond to enhanced conductance. (b) Peak splitting Δ_K, and parabolic fits, for 3 representative peaks at 3.2 T.

VI

Ge/Si HETEROSTRUCTURE NANOWIRES

6.1 Overview

Semiconductor nanowires can serve as the building blocks of nanoelectronic circuits due to their ability to act as both interconnects and active devices [103]. The controlled growth and reduced dimensions of nanowires has allowed for a bottom-up approach [103] of assembling nanoscale electronic circuits. The nanowires studied in this thesis are Ge/Si core/shell heterostructure nanowires. Our interests in germanium and silicon stem from their increased technological importance [104]. Band structure engineering of nanowire heterostructures allow for low-dimensional carrier gases with enhanced mobility, low scattering, and reproducible contacts.

A Ge/Si nanowire contacted with aluminum electrodes allows for transport studies in a completely new regime: at low temperature, the aluminum superconducts and induces superconductivity in the nanowire through a proximity effect. Our goal is to investigate proximity-induced superconductivity in Ge/Si nanowires in order to provide new insights into some open problems in mesoscopic superconductivity.

In Section 6.2, we introduce the unique Ge/Si radial heterostructure nanowires, and describe the nanowire synthesis and device fabrication. In Section 6.3, we present conductance measurements of the one-dimensional Ge/Si nanowires. In Section 6.4, useful background information regarding superconductivity is described. The experimental results of superconducting proximity effect in Ge/Si nanowires are deferred to Chapter 7.

6.2 Ge/Si Core/Shell Nanowires

6.2.1 Nanowire Synthesis

Typically, semiconductor nanowires are single crystal wires with diameters ranging from 10 nm to 100 nm and lengths of a few micrometers. There are several excellent growth techniques that are currently used for nanowire synthesis. The core-shell (radial heterostructure) nanowires studied in this thesis were synthesized using a chemical vapor deposition (CVD) based vapor-liquid-solid (VLS) technique.

The VLS growth technique was first proposed and demonstrated by Wagner and Ellis [105,106] in 1964 for the growth of silicon whiskers. This technique was further developed to grow InAs and GaAs wires with nanometer scale diameters [107-109]. The first step in the VLS process is the deposition of a metallic particle on the surface of the substrate that acts as the solid catalyst (S). A precursor vapor (V), the source material carrier gas, is then introduced into the chamber which is held above the eutectic temperature, and a liquid alloy droplet (L) is formed. As the precursor vapor is further incorporated into the alloy droplet, the droplet saturates, and a crystal nucleation process is initiated. This results in axial growth of the wire at the liquid-solid interface, with the metal catalyst being continually lifted up from the substrate during growth. A schematic of the VLS growth technique is shown in Figures 6.1 (a) and (b). The metallic particle used in the VLS growth technique determines the diameter of the wire.

As described above, axial growth occurs at the liquid-solid (catalyst-nanowire) interface and not on the nanowire surface. For radial growth, the chamber conditions are altered to induce growth by vapor-phase deposition on the nanowire surface [110],

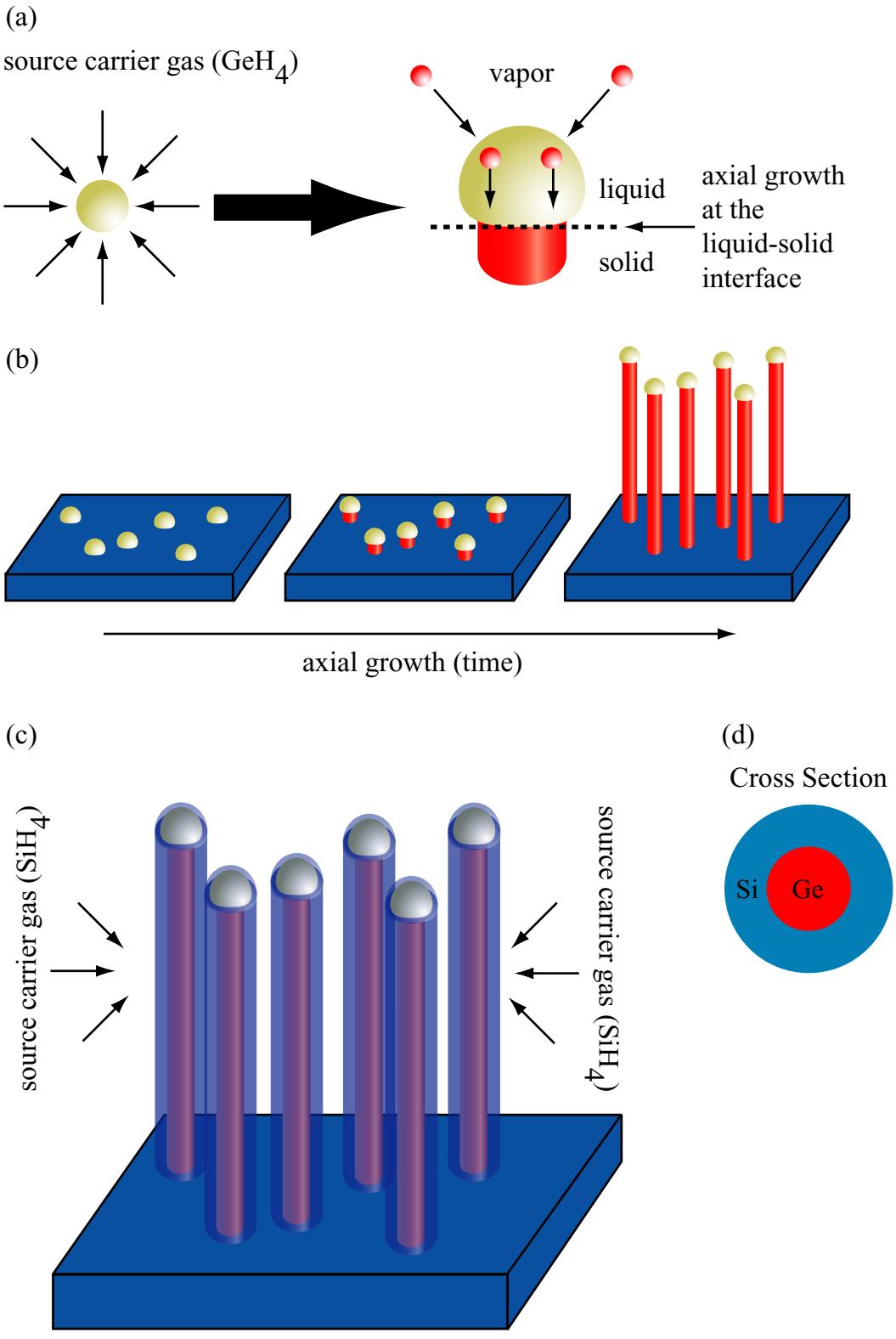

Figure 6.1 Schematic of the nanowire growth technique. (a) Vapor-Liquid-Solid mechanism. (b) Axial growth mechanism. (c) Shell growth mechanism. (d) Cross-section of the resulting Ge/Si core/shell nanowire.

schematically shown in Figure 6.1 (c). It is in this way that we are able to first grow Ge nanowires, and then coat them with a Si layer to form radial heterostructure nanowires, with a cross section as shown in Figure 6.1 (d).

The nanowires studied in this thesis are Ge/Si core shell nanowires grown by Jie Xiang of the Lieber group at Harvard University. The growth begins with the deposition of gold nanoparticles on oxidized silicon wafers. The gold nanoparticles used were 10 nm in diameter. The wafers were then placed in a quartz tube furnace. The germanium nanowire growth was initiated by nucleation at 315°C for 1 minute using 10% GeH_4 in H_2 (30 standard cm^3/min) and H_2 (200 standard cm^3/min) at 300 torr. Axial growth was performed at 280°C and 100 torr for 15 minutes. The growth rate for the Ge core was approximately 1 μm/min. The Si shell was deposited in the same chamber immediately following the Ge growth at 450°C and 5 torr for 1 minute using SiH_4 (5 standard cm^3/min). The growth rate for the Si shell was approximately 1 nm/min. Transmission electron microscopy images of the clean, epitaxially grown Ge/Si core/shell nanowires are shown in Figure 6.2 (a). The nanowires studied in this thesis have an average core diameter of 14.6 nm, with an average shell thickness of 1.7 nm.

The Ge/Si core/shell nanowires are radial heterostructures, with a valence band offset at the Ge/Si interface of approximately 500 meV. Measurements performed by the Lieber group on similar devices show that the Fermi level in these nanowires is pinned below the Ge valence band, as shown in Figure 6.2 (b) [111]. Therefore, there is an accumulation of hole carriers that are confined to the Ge-core quantum well. It is in this respect that we are able to form a one-dimensional hole gas. It is important to emphasize

(a)

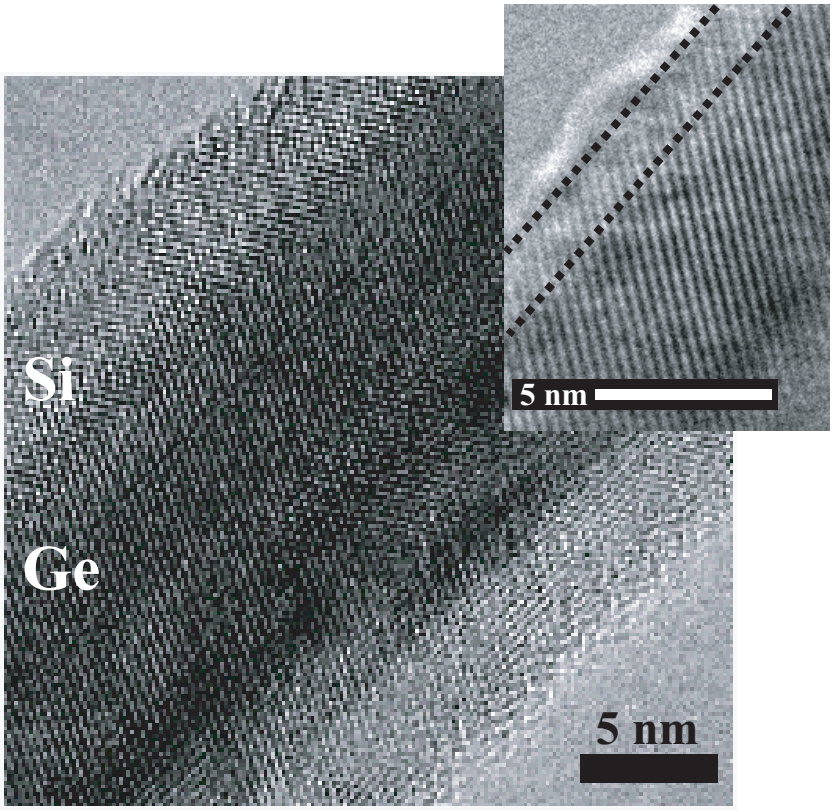

(b)

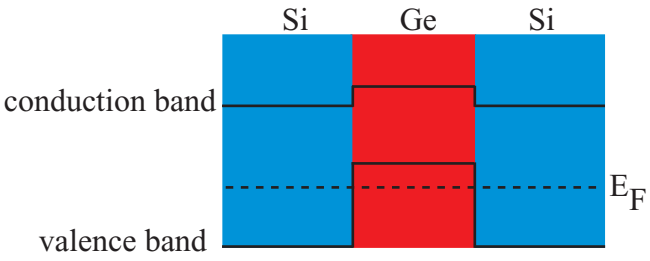

Figure 6.2 (a) Transmission electron micrographs of a Ge/Si core/shell nanowire. Contrast between the Ge and Si regions is due to the difference in atomic weights in Ge and Si. Dashed lines delineating the Si shell are included in the upper image.
(b) Schematic of the band diagram of the Ge/Si core/shell nanowire. The Fermi energy, indicated by the dashed line, lies below the Ge valence band.

that neither the Ge core nor the Si shell were doped during growth, and therefore, scattering from ionized dopants should be negligible.

6.2.2 Three-Terminal Device Fabrication

After growth, the substrates were sonicated in ethanol to aid in the lift-off of the nanowires from the substrates. The nanowires were then deposited on degenerately doped Si substrates (n-type, resistivity < 0.005 Ω-cm) with a 50 nm thermal oxide layer.

To create a three-terminal nanowire device, aluminum source and drain contacts were deposited using electron-beam lithography and metallization techniques described in Section 3.2. The source and drain contacts are 30 nm thick aluminum layers. No annealing step is performed after metallization. The length of the nanowire between the contacts is typically 100 nm to 150 nm. To achieve stronger gate-nanowire coupling than the back gate allows, a top gate was incorporated on the device. Atomic layer deposition [112] was used to deposit hafnium oxide (HfO_2) on the Ge/Si nanowires. Deposition was carried out at 110°C using 30 cycles to yield a thickness of 4 nm. Each cycle consists of a short exposure to a metal amide precursor, tetrakis(dimethylamido)hafnium (IV) and H_2O, and nitrogen purges. The top gate was then defined by electron-beam lithography, followed by deposition of 5 nm of Cr and 50 nm of Au. The complete three-terminal device is shown in Figure 6.3.

(a)

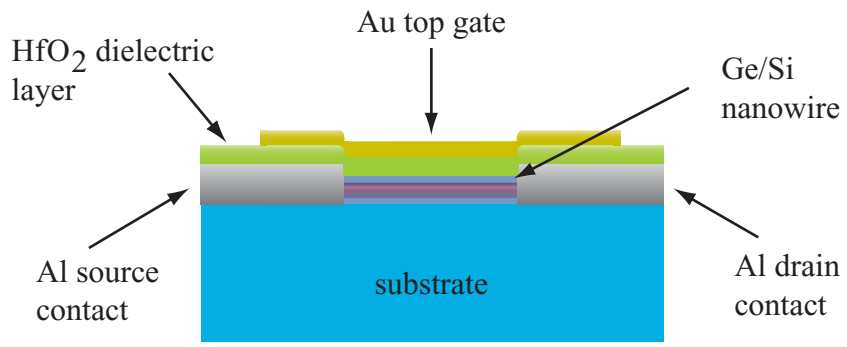

(b)

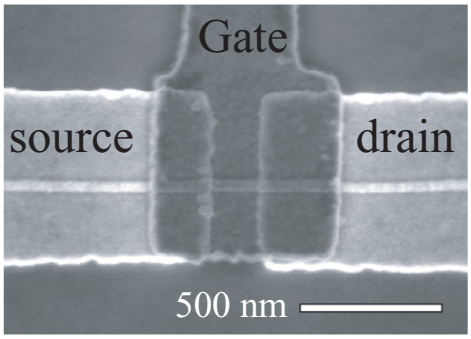

Figure 6.3 (a) Schematic and (b) scanning electron micrograph of the top gated nanowire device. The nanowire is contacted by 30 nm thick aluminum electrodes. A high-k dielectric layer covers the nanowire, and a gold top gate is deposited on the device. Typical length of the nanowire, between the electrodes, is 150 nm.

6.3 Electron Transport in One-Dimensional Ge/Si Nanowires

Assuming that a particle is confined to a narrow wire of length L_x, solutions of the Schrödinger equation can be written as

$$\psi(x,y,z) = Ae^{ik_x x}\xi_n(y,z) \tag{6.1}$$

where $\xi_n(y,z)$ satisfy a two-dimensional Schrödinger equation. These solutions describe 1D subbands, with free motion in the x-direction and quantized eigenstates bound in two dimensions. The energy spectrum is given by

$$E_n(k_x) = E_n + \frac{\hbar^2 k_x^{\,2}}{2m^*} \tag{6.2}$$

The 1D density of states (per unit length) in the n^{th} subband is

$$\rho_n(E) = 2g_s g_v\left(2\pi\frac{dE_n(k_x)}{dk_x}\right)^{-1} = \frac{g_s g_v}{\pi\hbar}\sqrt{\frac{m^*}{2(E-E_n)}} \tag{6.3}$$

Here, g_s and g_v are the spin degeneracy and valley degeneracy, respectively. A factor of 2 was included to account for both states with positive k_x and states with negative k_x. At equilibrium, the number of states with positive k_x equals the number of states with negative k_x and there is therefore no net current. If a small voltage bias V_{SD} is applied across the wire, causing a difference $eV_{SD} = \mu_{source} - \mu_{drain}$ between the electrochemical potentials of the source and drain contacts, a net current flows. The contribution to the current by a single occupied subband is

$$I_n = \int_{\mu_{drain}}^{\mu_{source}} e\left(\frac{1}{\hbar}\frac{dE_n(k_x)}{dk_x}\right)\frac{1}{2}\rho_n(E)dE \tag{6.4}$$

where the term in parentheses is the group velocity. The factor of 1/2 was included so that only states with positive k_x contribute to the current. The contribution to the current

by a single occupied subband can be calculated by solving Equation (6.4), and noting that the dependence on $E_n(k)$ simply cancels. This leads to

$$I_n = \frac{g_s g_v}{2\pi\hbar} e(\mu_{source} - \mu_{drain}) = \frac{g_s g_v}{2\pi\hbar} e(eV_{SD}) = \frac{g_s g_v e^2}{h} V_{SD} \tag{6.5}$$

The contribution to the conductance by a single occupied subband is therefore

$$G_n = \frac{I_n}{V_{SD}} = g_s g_v \frac{e^2}{h} \tag{6.6}$$

Every time a new subband is populated in the one-dimensional nanostructure, the conductance increases by this value. This leads to conductance plateaus, as described in Section 2.3 in relation to a quantum point contact.

Typically, when measuring transport through a one-dimensional nanostructure, a capacitively coupled gate with voltage V_G can be tuned to change the carrier density and consequently, the number of 1D subbands populated. However, a change in V_G modifies both the spacing of the 1D subbands, due to changes in the confining potential, and also the electrostatic potential energy eV of the nanostructure. A schematic diagram helpful in describing transport in one-dimensional conductors is shown in Figure 6.4. We can incorporate the gate voltage by rewriting Equation (6.2) as

$$E_n(k_x) = E_n(V_G) + \frac{\hbar^2 k_x^{\,2}}{2m^*} + eV. \tag{6.7}$$

The nonlinear conductance can be measured by applying a source-drain bias V_{SD} across the nanostructure, and allowing different numbers of subbands in the forward and reverse directions to be populated [113]. A typical measurement used to study a one-dimensional nanostructure consists of the differential conductance $G = dI/dV_{SD}$ as a function of both V_G and V_{SD}.

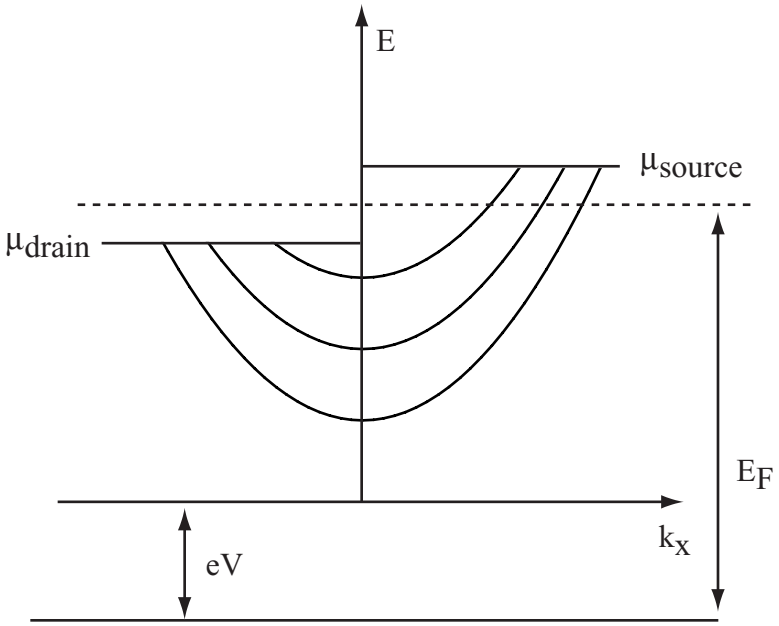

Figure 6.4 Series of 1D subbands with band bottoms at E_n, n = 1, 2, 3. An applied source-drain bias sets the electrochemical potential of the contacts: $eV_{SD} = \mu_{source} - \mu_{drain}$. When the number of occupied subbands is the same for both positive and negative k_x the conductance is quantized. The gate voltage changes the location of the band bottoms and also the spacing of the subbands.

Transport in a one-dimensional nanostructure can be diffusive, quasi-ballistic, or ballistic, depending on the various length scales involved. The important scales to consider are the length L_x of the nanostructure, the Fermi wavelength λ_F, the width W, and the elastic mean free path l_e. The Fermi wavelength λ_F, compared to the width of the nanostructure, determines the dimensionality of the system. For ballistic transport, $L_x, W \ll l_e$, and 1D quantum states extend across the wire. Scattering does not affect the transport; the carriers only feel the physical boundaries of the nanostructure. For quasi-ballistic transport, $W \ll l_e \ll L_x$, and a few impurities are present in the wire and mix the 1D modes. For diffusive transport, $l_e \ll W < L_x$, and scattering off impurities dominates. In the diffusive regime, l_e is the dominant length scale, and therefore, the one-dimensionality of the wire is lost.

As derived above, transport through one-dimensional nanostructures results in conductance quantization, and is typically observed in GaAs/AlGaAs 2DEGs using quantum point contacts, as discussed in Section 2.3. However, deviations from $2e^2/h$ are sometimes observed even in such clean systems [114]. Such deviations may arise from a sudden change in the electrostatic potential of the one-dimensional nanostructure that will result in inter-mode coupling or partial reflections of the electron waves.

We now turn to conductance measurements of the Ge/Si core shell nanowires. Figure 6.5 shows the conductance G as a function of the source-drain voltage V_{SD} for different values of top gate voltage V_G. Measurements were performed at 10 K. Dark regions corresponding to areas where curves are bunching are clearly observed and are spaced by approximately e^2/h. Regions where the curves are bunching are plateaus in the conductance because bunching indicates that a change in the top gate voltage V_G results

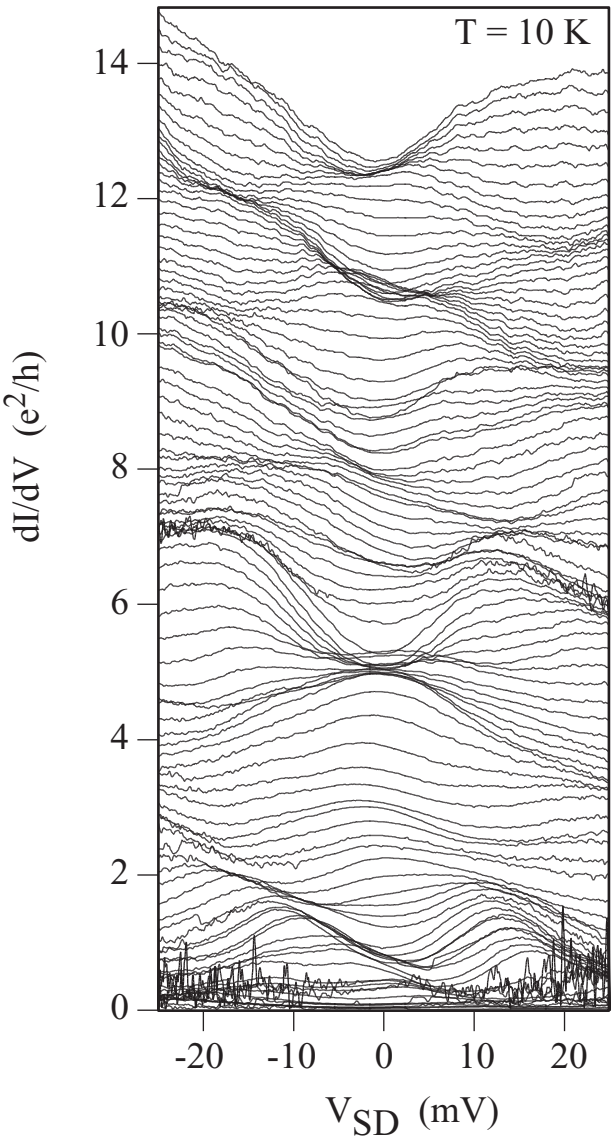

Figure 6.5 Differential conductance dI/dV_{SD} at T = 10 K as a function of the source-drain voltage V_{SD}. Each curve corresponds to a different value of gate voltage (V_G = 0.8 V to -3.5 V in 50 mV steps, with no offset applied). Dark regions where curves are bunching are clearly observed, and are the location of the conductance plateaus. Plateaus at zero source-drain bias evolve into plateaus at large bias.

in very small changes in G. We find deviations from conductance quantization in units of $2e^2/h$ possibly due to the reasons described above.

In Figure 6.5, we see that the plateaus (bunching) at zero-bias ($V_{SD} = 0$) evolve into plateaus (bunching) at large bias ($V_{SD} \sim \pm 20$ mV). The observed bunching of conductance curves evolving into half plateaus at large bias suggests of transport through one-dimensional subbands in the Ge/Si nanowire [111]. This is similar to nonlinear conductance measurements in quantum point contacts [115] where plateaus at zero-bias evolve into half plateaus at large bias when the electrochemical potentials of the source and drain contacts cross different subbands, resulting in a diamond pattern outlining the subband energy spacing.

6.4 Superconducting Proximity Effect

The BCS theory provides a microscopic theory for the origin of superconductivity in metals. The underlying concept of the BCS theory is that in the presence of a weak attractive potential between electrons, the energy of the Fermi sea of electrons could be lowered if opposite-momentum, opposite-spin electrons form bound pairs [116,117]. Two electrons in a metal generally feel a repulsive force due to a direct Coulomb interaction. However, at temperatures below a critical temperature T_C, an indirect phonon-mediated interaction may become dominant, and serves to attract two electrons at the Fermi surface. This leads to the formation of bound pairs of electrons, called Cooper pairs. A Cooper pair is a boson consisting of two electrons with equal and opposite momentum and spin. All the Cooper pairs in the conductor condense into a single state, resulting in an energy gap of width 2Δ centered on the Fermi energy E_F, as shown in Figure 6.6 (a).

The energy gap Δ is dependent on the temperature and magnetic field. At zero temperature, the BCS theory predicts that [26]

$$\Delta = 1.76 k_B T_C \tag{6.8}$$

The density of states for the superconducting state is given by [26]

$$N(E) = \begin{cases} \dfrac{N(0)E}{\sqrt{E^2 - \Delta^2}}, & |E| > \Delta \\ 0, & |E| < \Delta \end{cases} \tag{6.9}$$

were N(0) is the density of states at the Fermi surface and is a constant. There are no states available in a width 2Δ around E_F [Figure 6.6 (a)]. This energy gap affects the transport properties of normal-superconductor (N-S) junctions.

The coherence length ξ_0, one of the key characteristic length scales describing a superconductor, is calculated in the BCS theory to be (at T = 0)

$$\xi_0 = \frac{\hbar v_F}{\pi \Delta} \tag{6.10}$$

where v_F is the Fermi velocity. In the phenomenological Ginzburg-Landau theory of superconductivity [26], the coherence length can be understood as the spatial extent over which the superconducting order parameter reduces to zero.

We are interested in transport in superconductor-normal-superconductor (S-N-S) junctions where the normal metal is made superconductive by a proximity effect. The process of Andreev reflections [118] at a N-S interface is crucial to the understanding of the proximity effect [119]. Figure 6.6 (b) shows the energy spectrum of a N-S junction. An electron in the normal metal with energy less than Δ cannot enter the superconductor because no states exist at the same energy in the superconductor. However, transport into the superconductor can occur if a 4 particle process takes place: an electron in the normal

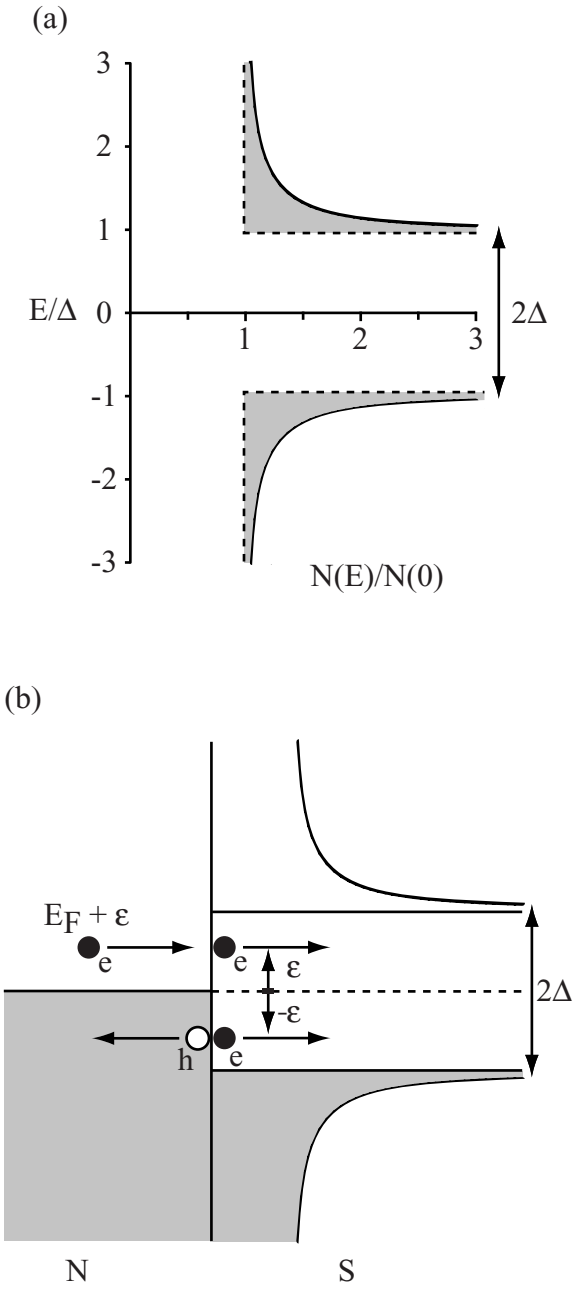

Figure 6.6 (a) Plot of the density of states (horizontal axis) of the superconducting state. (b) Schematic diagram of a N-S interface showing the Andreev reflection process. An electron with energy $E_F + \varepsilon$ in N incident on the N-S interface is reflected as a hole in N. The incident electron effectively drags a second electron with energy $E_F - \varepsilon$ to form a Cooper pair in S.

metal is reflected as a hole at the N-S interface, and a Cooper pair is generated in the superconductor. This process was first studied by Andreev in 1964 and is known as an Andreev reflection [118]. The process is shown in Figure 6.6 (b). The reflected hole has the same momentum as the incident electron, but its velocity is opposite to the momentum, and therefore the hole retraces the incident electron trajectory. The reflected hole is a result of a second electron being "dragged" into the superconductor by the incident electron to generate a Cooper pair. The Andreev reflection correlates the two electrons.

In an Andreev reflection process, charge and energy are conserved but momentum is, in general, not conserved. Conservation of charge is satisfied because the initial charge is just -*e* and the final charge is -2*e* of the Cooper pair plus *e* of the hole. For energy conservation, assuming the incident electron has energy $E_F + \varepsilon$, the hole has energy $E_F - \varepsilon$. Finally, momentum conservation is obtained when ε is zero only. Otherwise, the incident electron momentum $k_F + \frac{\Delta k(\varepsilon)}{2}$ and the reflected hole momentum $k_F - \frac{\Delta k(\varepsilon)}{2}$ are different by $\Delta k(\varepsilon) = k_F \varepsilon / E_F$.

In a S-N-S system, Andreev reflections can occur at either the left or right superconductor-normal interface. Successive Andreev reflections at both the S-N and N-S interfaces lead to the formation of Andreev bound states in the junction. An electron incident on the (right) N-S interface will generate a Cooper pair and reflect a hole. This hole will travel to the (left) S-N interface and reflect an electron by breaking up a Cooper pair. The net result of such reflections is the transfer of Cooper pairs across the junction. In this way, due to the proximity effect, a supercurrent (Josephson effect) can flow through the junction [119].

Multiple Andreev reflections allow for "Andreev channels" to open up in the S-N-S junction and gives rise to a subharmonic energy gap structure in the differential conductance dI/dV as a function of the bias voltage V. These Andreev channels arise from a progressive increase of the incident electron energy as it reflects between the two interfaces. Each time the electron (or hole) travels across the junction, it picks up an energy eV until the energy exceeds the gap energy. The multiple Andreev reflections are seen as peaks in dI/dV at the location of $eV = 2\Delta/n$ (for n = 1, 2, 3…). A general description of this effect was given by Blonder, Tinkham, and Klapwijk (BTK) [120]. The BTK theory uses the Bogoliubov-de Gennes equations to calculate the reflection and transmission probabilities for particles incident on the N-S interface. These probabilities are then used to calculate the net current.

The critical current I_C in the S-N-S junction is defined as the *maximum* supercurrent that can flow through the junction

$$I_C \sim \frac{ev_F}{L} \tag{6.11}$$

Here, L is the length of the normal metal. We can use the coherence length from Equation (6.10) for L, appropriate for zero temperature, to get

$$I_C \sim \frac{e\Delta}{\hbar} \tag{6.12}$$

If M modes are available, the total critical current is just the sum of the contribution from each mode:

$$I_C = M\,\frac{e\Delta}{\hbar} \tag{6.13}$$

Combining this with the normal state quantized conductance formula (with M modes) $G_N = M\left(2e^2/h\right) = 1/R_N$, we get:

$$I_C R_N \sim \frac{\Delta}{e} \tag{6.14}$$

We find that $I_C R_N$ is a constant, depending only on the material and temperature through the energy gap Δ. The relation

$$I_C R_N = C\frac{\Delta}{e} \tag{6.15}$$

is in fact true for weak links (Josephson junctions) in general [26]. The Ambegaokar-Baratoff formula defines C to be $\pi/2$, whereas the calculations by Kulik and Omel'yanchuk calculate a value of C either 1.32 or 2 times greater than $\pi/2$, for dirty and clean metallic junctions [26]. For this thesis, it is only important to note that $I_C R_N \sim \Delta/e$ and is expected to be constant for a given material and temperature regardless of the junction geometry.

In conclusion, the proximity effect in S-N-S junctions is a result of correlations between electrons and holes (quasi-particles) in the normal conductor as a result of Andreev reflections. The generated supercurrent in the normal conductor indicates the phase coherent motion of the quasi-particles. In the next chapter, we describe our research on the proximity effect in nanowires. We believe that this is an exciting area of research, and could lead to possible phase coherent electronic devices using superconducting circuit elements.

VII

SUPERCONDUCTING PROXIMITY EFFECT IN SEMICONDUCTOR NANOWIRES

7.1 Overview

S-N-S junctions [121] are interesting systems that can display rich behavior, including macroscopic quantum phenomena as manifested in the Josephson effect. S-N-S junctions are also important from a technological perspective because of their roles in SQUIDs [122] and Josephson field-effect transistors [123,124]. In almost all of the previous investigations of S-N-S junctions, conventional metals have been used as the weak links (the N regions). Furthermore, the junction size was of *fixed* width, with the normal metal having a large carrier density that cannot be depleted. Recent progress in nanoscale fabrication techniques now makes it possible to use a semiconductor as the weak link and create hybrid semiconductor-superconductor junctions. With an additional local metal gate, the carrier density of the semiconductor can be modified, effectively creating a S-N-S junction of variable width. This will allow an investigation of variable carrier density S-N-S junctions in the ballistic regime where quantization of supercurrent is expected to be observed [125]. Experiments on mechanically controllable break junctions have been performed showing possible quantization steps of the supercurrent [126]. However, the large fluctuations in the observed data highlight the need for a clean system that only a ballistic semiconductor weak link can provide.

The ability to create coherent hybrid semiconductor-superconductor nanostructures has opened up a new field of study combining mesoscopic physics and

superconductivity. Quantum confinement of carriers can be introduced in the semiconductor, for example, by using band structure engineering, allowing for a variety of new and exciting weak links consisting of low-dimensional systems where electron-electron interactions can play an important role.

In this chapter, Ge/Si semiconductor nanowires are used as weak links in a S-nanowire-S geometry, and the junction properties are investigated. These unique junctions offer the opportunity to investigate the interplay between one-dimensional quantum confinement and superconductivity. A local top gate allows for the nanowire carrier density to be modified, tuning the Fermi level through a discrete 1D density of states. In this way, transport through the nanowire can be restricted to the first few 1D modes.

The Ge/Si nanowires are fabricated in a three-terminal device geometry, with aluminum source and drain electrodes and a gold top gate. The device was discussed in detail in Chapter 6, where we also presented evidence of transport through 1D subbands in the Ge/Si nanowires. In the next section, we describe the low-noise filtering techniques that are necessary for the proximity-induced superconductivity measurements. In Section 7.3, we present our results on supercurrents in Ge/Si nanowires. In Section 7.4, we discuss multiple Andreev reflections in the S-nanowire-S junctions. Finally, in Section 7.5, we discuss the connection between 1D modes and superconductivity.

7.2 Low-Noise Measurement Setup

In order to observe supercurrents (with critical current I_C) in conventional S-N-S junctions, the Josephson energy $E_J = \hbar I_C / 2e$ must be greater than the thermal energy $k_B T$:

$$E_J = \hbar I_C / 2e \gg k_B T \rightarrow I_C \gg 2ek_B T / \hbar \tag{7.1}$$

A more practical form of this constraint can be derived by noting that $I_C R_N \sim \Delta/e$ [Equation (6.14)] and $\Delta = 1.76 k_B T_C$ [Equation (6.8)]. With these relations, we can rewrite Equation (7.1) as

$$E_J / k_B T \gg 1$$

$$\left(\frac{\hbar}{2e}\right)\left(\frac{I_C}{k_B T}\right) \gg 1$$

$$\left(\frac{\hbar}{2e}\right)\left(\frac{\Delta}{eR_N k_B T}\right) \gg 1$$

$$\left(\frac{\hbar}{2e}\right)\left(\frac{(1.76 k_B T_C)}{eR_N k_B T}\right) \gg 1$$

$$\left(\frac{h}{e^2 R_N}\right)\left(\frac{T_C}{T}\right) \gg 1$$

$$\left(\frac{R_Q}{R_N}\right)\left(\frac{T_C}{T}\right) \gg 1 \tag{7.2}$$

Where $R_Q = h/e^2$ is the quantum resistance and T_C is the critical temperature of the superconducting electrodes. Equation (7.2) clearly shows that observation of supercurrents requires that (i) the normal state resistance of the junction to be much less than the quantum resistance and that (ii) the temperature T must be much less than T_C.

This translates to having junctions with high contact transparency operating at low temperature.

The temperature T appearing in the equations above is very sensitive to noise. As stated in the text by M. Tinkham [26]: *I_C must be sufficient to overcome an effective noise temperature which may approach room temperature rather than the temperature of the superconductor, unless the electrical leads are very well screened*. Therefore, it is necessary to reduce the radiation noise fed down from the electronic circuitry to prevent electronic heating of the sample.

We employed three stages of filtering on all the electrical leads. An illustration of the experimental setup is shown in Figure 7.1 (a). At room temperature, before the electrical leads enter the cryostat, π filters (Spectrum Control Inc., Part # 9001-100-1017) are placed on each electrical lead. The π filters are mounted inside a Pomona box (Pomona Electronics, Part # 3752) through a RF-tight copper divider, as shown in Figure 7.2 (a). The copper divider separates the 'in' section from the 'out' section to further shield the outgoing signal from radiation. Above 1 MHz, the measured attenuation of these π filters is 80 dB. A second stage of filtering is provided by 10 kΩ metal film resistors embedded in a copper chuck, as shown in Figure 7.2 (b). The copper chuck is thermally anchored to the mixing chamber. The 10 kΩ metal film resistors, along with the cable inductance and capacitance, serve as *cold* low-pass RLC filters with an estimated noise cut off frequency of 10 kHz. The final stage of filtering of the leads, effective for frequencies above 1 GHz, is provided by a copper powder filter that is integrated on the cold finger, shown in Figure 7.2 (c). The area between the inner and outer tubes of the cold finger is filled with a mixture of surface-oxidized copper powder

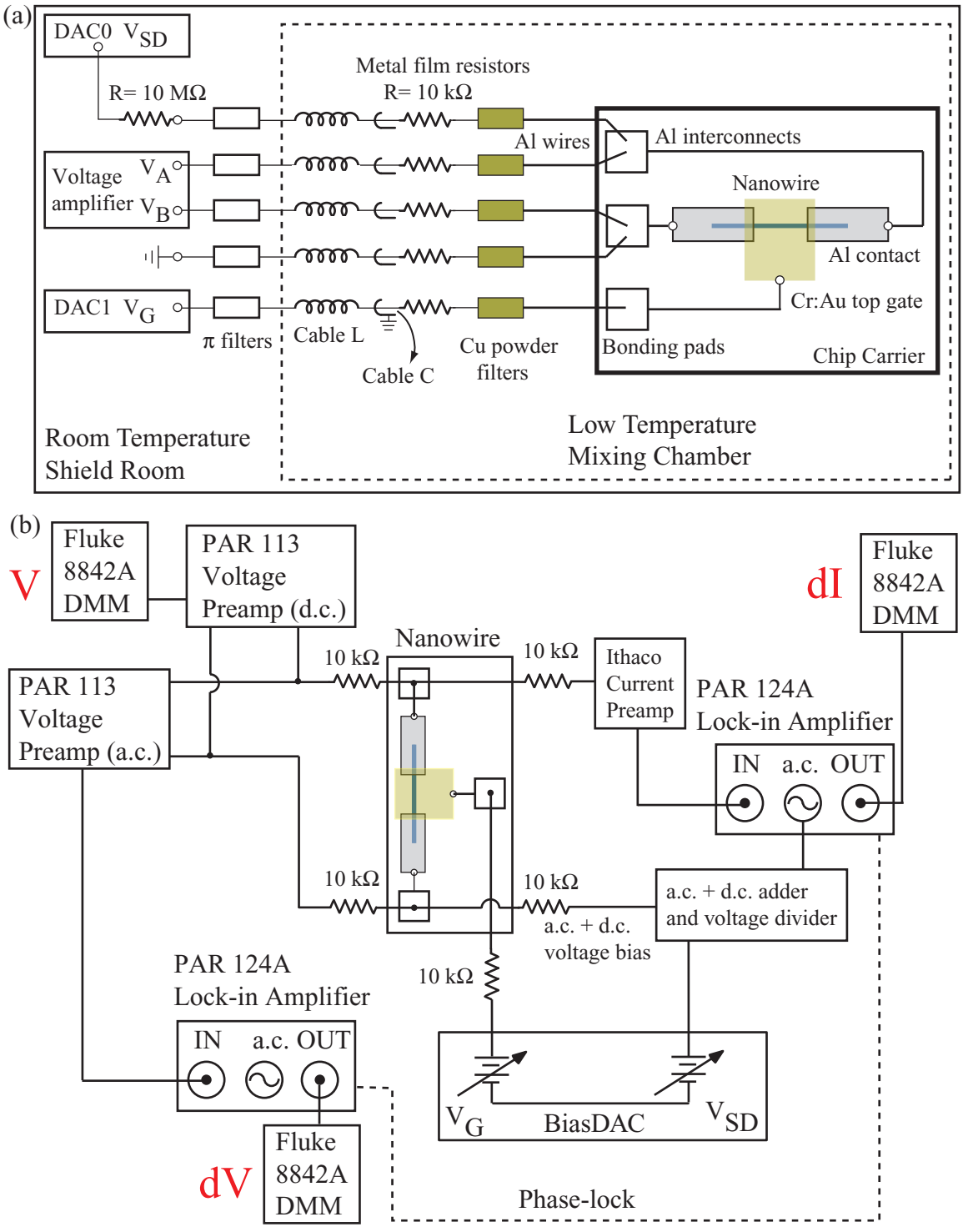

Figure 7.1 (a) Schematic diagram of a typical current bias nanowire measurement showing the three stages of filtering. Each electrical lead passes through a π filter placed on the top of the dilution insert. Metal film resistors and copper powder filters thermally anchored to the mixing chamber provide additional noise attenuation. The dilution refrigerator and measurement electronics are placed inside a shielded room. (b) Circuit diagram showing the four-probe voltage bias nanowire measurement setup.

and epoxy (Stycast #1266, Emerson and Cumming Inc.), and the electrical leads were coiled inside this cavity and then connected to the sample. RF noise is attenuated in these filters due to the large effective surface area of the copper particles and the small skin depth [127].

In addition to the filtering of the electrical leads, several layers of radiation shielding was provided. Once the sample is placed on the socket at the end of the cold finger, a copper cap screws over the sample. Therefore, the electrical leads exiting the copper powder filter connect directly to the sample while remaining shielded from electromagnetic interference. A 600 mK radiation shield is placed around the lower section of the ^{3}He/^{4}He insert. The can of the Inner Vacuum Chamber and the cryostat provide additional layers of shielding. Finally, the ^{3}He/^{4}He dilution refrigerator and the measurement electronics sit inside a sealed shielded room. The data acquisition computer is placed outside the shielded room, and communicates with the measurement electronics via optical fibers.

All measurements presented in this chapter were performed at the mixing chamber temperature of 60 mK. Four-probe measurements [Figure 7.2 (b)], as discussed in Section 3.4.1, were used to obtain voltage-bias measurements of dV/dI and dI/dV. The four probes were formed by wire bonding a pair of wires onto each aluminum electrode.

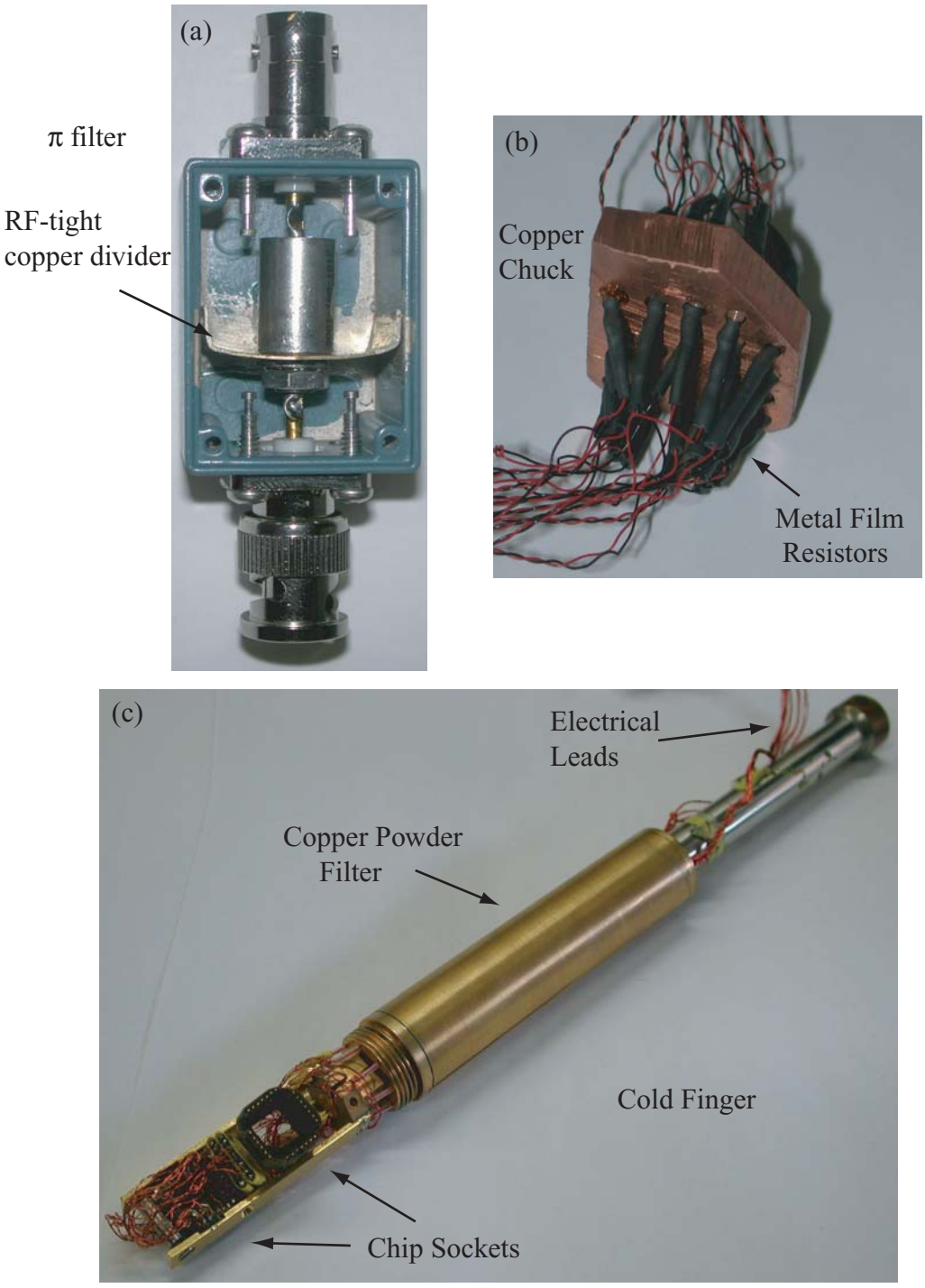

Figure 7.2 (a) Photograph of the π filter used in the measurements. A RF-tight copper divider separates the input section of the Pomona box from the output section. (b) Copper chuck with twenty four 10 kΩ metal film resistors embedded on the chuck. GE varnish is used to glue the resistors in place. (c) Cold finger for the dilution refrigerator with a copper powder filter. The copper powder filter exists between the inner and outer tubes. All electrical leads pass through the copper powder filter and then connect to the two chip sockets. A copper cap (not shown) screws over the bottom part of the cold finger.

7.3 Tunable Dissipationless Supercurrents

As discussed in Section 6.4, a normal metal contacted by superconducting electrodes exhibits superconductivity. Here, we present experimental results of Josephson dissipationless supercurrents through Ge/Si nanowires in contact with aluminum electrodes. The measured critical temperature of the aluminum electrodes, obtained from multiple Andreev reflections discussed in Section 7.4, is $T_C = 1.6$ K. Figure 7.3 shows a typical voltage-current characteristic of the S-nanowire-S junction obtained in a four-probe current bias configuration, with the top gate tuned to -3.5 V. A clear superconductive region of (effectively) zero resistance is observed. If the bias current is increased (black arrow) past the critical current I_C, V(I) abruptly switches to dissipative conduction. When the current bias is swept down (red arrow), V(I) switches back to a dissipationless state at a return current I_R that is smaller than I_C. This hysteretic behavior is typical for an underdamped Josephson junction [26]. The hysteretic behavior can also be explained from heating: as the current bias is increased from zero past I_C, the junction is heated. Therefore, when the current bias sweep is reversed, the wire is still hot and does not superconduct until it reaches a lower current bias. From Figure 7.3 we see that the critical current is approximately 113 nA. This is the largest critical current reported to date in semiconductor nanowires (see, for example, Ref. [128]).

The top gate field-effect geometry allows us to modify the carrier density in the nanowire by simply changing the voltage applied to the gate. As discussed in Chapter 6, the nanowire is p-type (hole carriers). Therefore, a more negative gate voltage induces carriers in the system and allows for higher critical currents. This results in a junction where the critical current can be tuned. Figure 7.4 shows V(I) curves for several values of

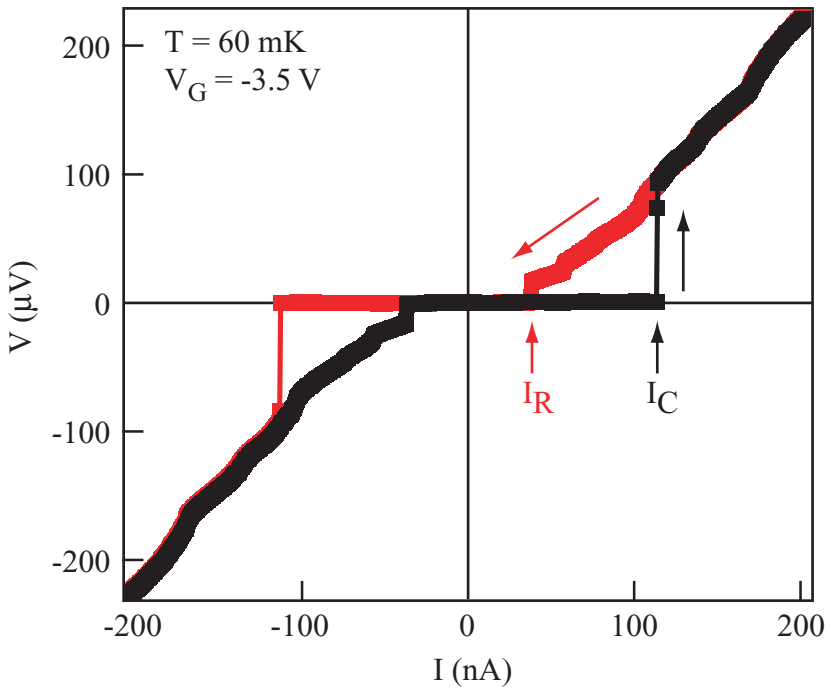

Figure 7.3 V-I characteristics of a Ge/Si nanowire measured at T = 60 mK using the four-probe current bias measurement setup shown in Figure 7.1 (a). The top gate is tuned to -3.5 V. The critical current I_C is observed as a sharp transition from the superconducting state to the resistive state. The black and red curves correspond to different current sweep directions, as indicated by the arrows. A hysteretic effect is observed, leading to a return current I_R that is smaller than I_C.

gate voltages, and shows that the extent of the superconductive coupling can be tuned with the change of the carrier density inside the semiconductor nanowire. The top gate provides an additional experimental knob that is not available in conventional S-N-S junctions employing metallic weak links. We note that the resistance in the superconductive region, measured from the slope of the V(I) curve, varies between 2 Ω to 5 Ω in our measurements. We believe this non-zero resistance arises from the wire bonding to the contact pads and also reflects the residual noise from the electromagnetic environment.

The V(I) curves display several kinks immediately above I_C, corresponding to multiple Andreev reflections, and is further discussed in the next section. Only at large bias, where $eV \gg 2\Delta$, is the normal state V(I) curve recovered, as shown in Figure 7.5. At high bias, the normal resistance R_N can be measured directly from the slope of V(I).

The contact transparency can be determined from the excess current of the V(I) curves. The excess current I_{exc} is the residual current at zero voltage when the high current bias V(I) curve is extrapolated to zero, as shown in Figure 7.5. From the values of the excess current, determined at several different gate voltages, and comparison to numerical calculations [129], we find that the contact transparency is approximately 80%. The high contact transparency, which was observed in all the other devices that were measured, demonstrates the excellent, reproducible contacts that can be formed using band structure engineered devices.

In Figure 7.6 we show I_C versus magnetic field B. The magnetic field is oriented perpendicular to the sample. As the magnetic field is increased, we observe an anomalous enhancement of superconductivity giving rise to an increase in I_C. Upon further

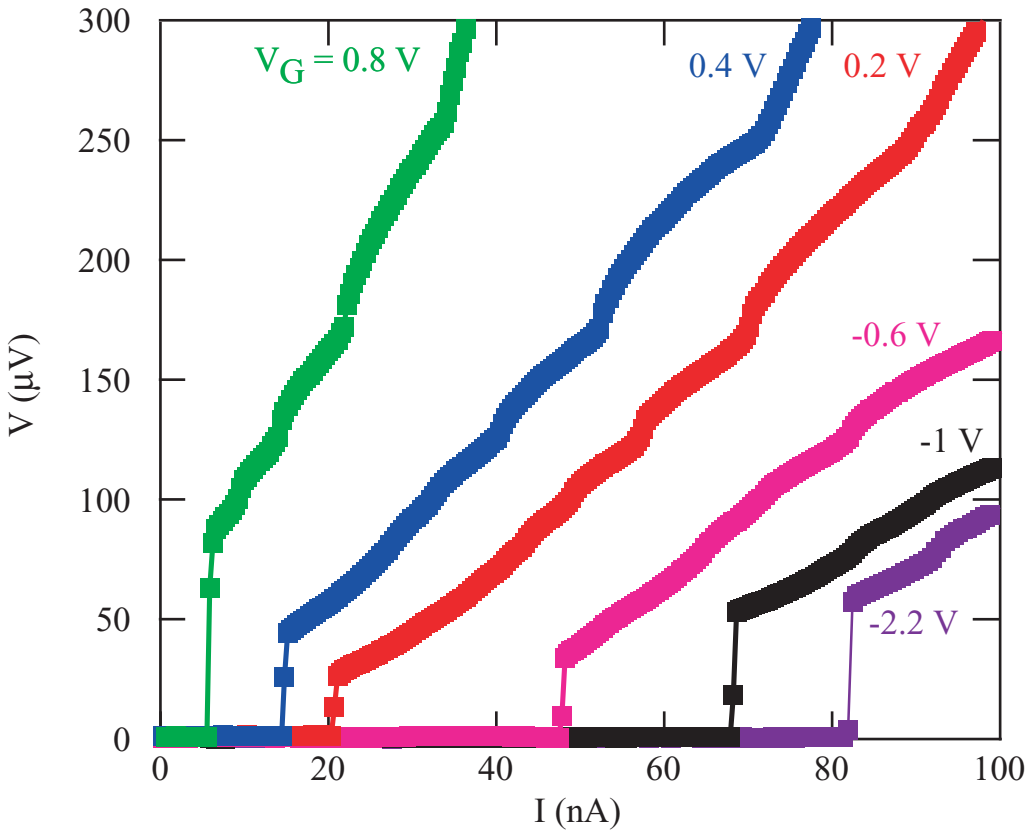

Figure 7.4 Tunable supercurrents in Ge/Si nanowires. The V-I curves are measured at different gate voltages, as indicated, with the voltage recorded while sweeping the current from zero toward 100 nA.

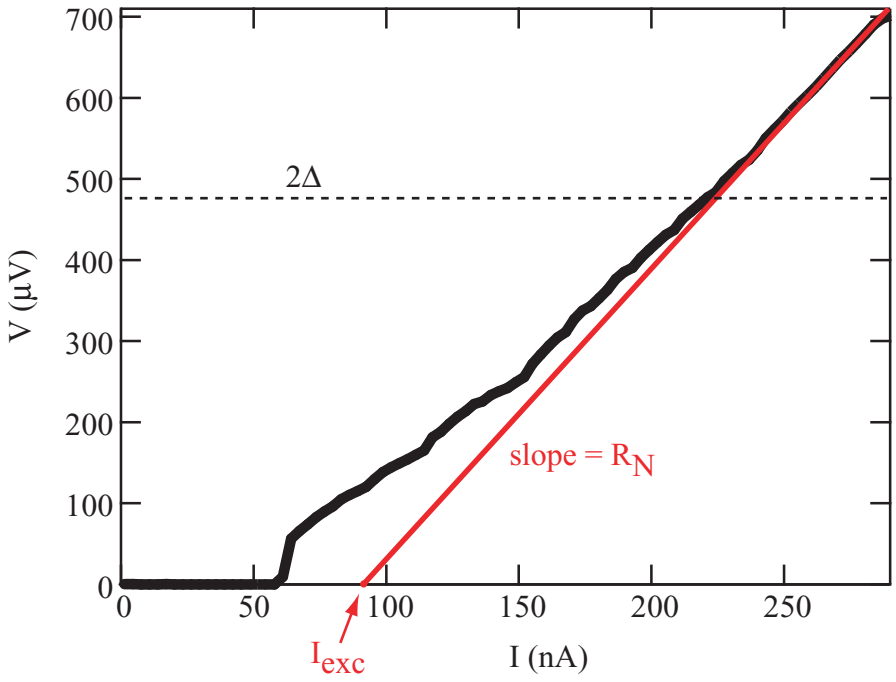

Figure 7.5 V-I curve (black line) measured with V_G = -1 V. V(I) returns to the normal state only when $eV > 2\Delta$ (dashed line). The value of 2Δ is determined from multiple Andreev reflection data (see text and Figure 7.7) and equals 470 μeV. In the high bias regime, a straight line is fitted to V(I) (red line) and the normal state resistance R_N and excess current I_{exc} can be determined from the slope and intercept, respectively. The non-zero excess current represents the enhanced conductivity due to the proximity induced superconductivity at $eV < 2\Delta$ and allows for an approximate value of the contact transparency to be extracted (see text).

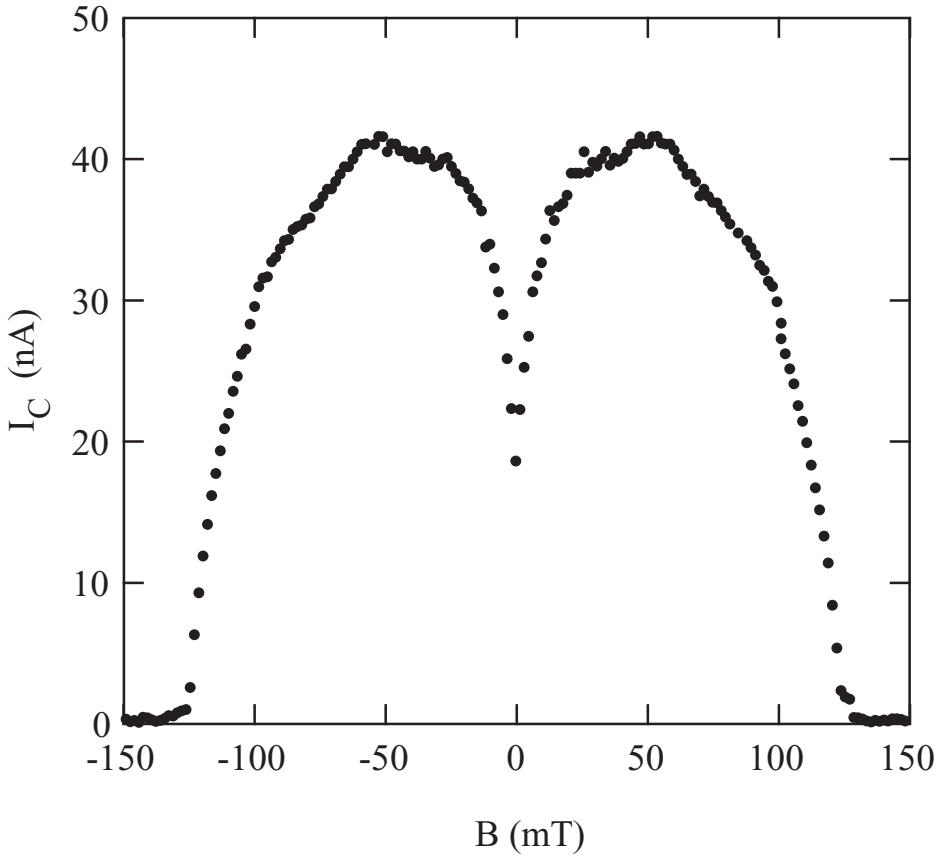

Figure 7.6 Critical current I_C versus magnetic field, with the field oriented perpendicular to the sample. At small magnetic field, an anomalous enhancement of the critical current is observed. Upon further increase of the magnetic field, superconductivity in the Al electrodes is suppressed, resulting in a decrease of I_C to zero.

increasing the magnetic field, superconductivity in the leads is suppressed and I_C goes to zero. We are not aware of any explanations for observing such an effect in our S-nanowire-S junctions. However, similar data in ultra-narrow MoGe and Nb wires was recently reported and explained by the presence of local magnetic moments in the surface oxide of the nanowires [130,131]. Further measurements in a *parallel* magnetic field orientation would allow for a more thorough investigation of this effect.

7.4 Multiple Andreev Reflections and Subharmonic Gap Structure

In Figures 7.3 and 7.4, we observed several kinks in V(I) immediately above I_C, which tend to develop at the same voltage levels for different values of V_G. These features can be attributed to multiple Andreev reflections. The multiple Andreev reflection (MAR) process allows carriers to gain the energy of the bias voltage each time it travels between the superconducting electrodes. Therefore, MAR gives rise to peaks in the differential conductance when the sum of the energy gain becomes multiples of the BCS gap energy Δ of the contact leads (see Section 6.4).

The subharmonic energy-gap structure resulting from multiple Andreev reflections can be observed in measurements of the differential conductance. Figure 7.7 shows a plot of the differential conductance dI/dV_{SD} as a function of the source-drain voltage bias V_{SD}. The top gate voltage is set at V_G = -900 mV. A four-probe lock-in measurement was used, with a 100 pV a.c. excitation voltage. Clear peaks are observed, symmetrically situated around $V_{SD} = 0$. The peak at zero source-drain bias, with a height greater than 1×10^4 e^2/h, corresponds to "infinite conductivity" when the nanowire becomes superconducting. This peak height is limited by several factors, including the

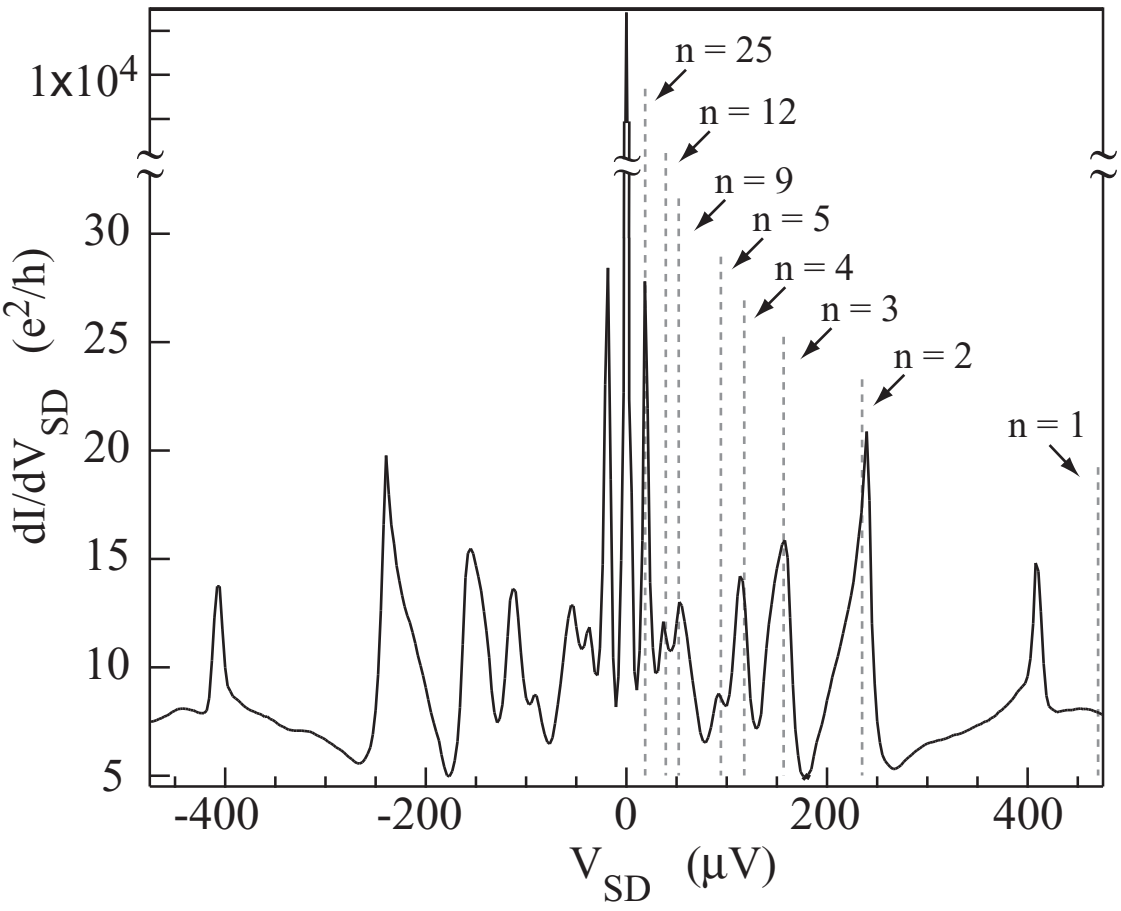

Figure 7.7 Four-probe measurement of dI/dV_{SD} showing the clear subharmonic gap structure of the Ge/Si nanowire device. The top gate is tuned to V_G = -900 mV. Arrows and dashed lines mark the expected MAR peak positions given by the BTK equation $eV_{SD} = 2\Delta/n$. A fit of the peak positions to this equation gives Δ = 235 μeV.

a.c. excitation voltage and the sweep rate. The peaks at finite source-drain voltage correspond to the subharmonic gap structure of the junction caused by MAR, with peak positions given by $eV_{SD} = 2\Delta/n$ (n = 1,2,3…), as is expected from the BTK theory [114]. From a fit of the MAR peak positions to $eV_{SD} = 2\Delta/n$ (n = 1,2,3…), we can determine the energy gap Δ = 235 μeV and find that the observed peaks correspond to n = 1, 2, 3, 4, 5, 9, 12 and 25. Using the BCS relation $\Delta = 1.76 k_B T_C$ [Equation (6.8)], the measured energy gap Δ = 235 μeV corresponds to T_C = 1.6 K for the Al leads in the BCS model. The arrows and dashed lines in Figure 7.6 mark the calculated peak positions and demonstrate the excellent fit of the observed data with theory. We note that the position of the first peak at high bias does not agree with this energy gap value. This can be explained by local heating of the junction due to the high voltage bias that is applied [132].

We typically observe 8 or 9 MAR peaks, with order n as high as 25. Such a clear signature of multiple Andreev reflections reflects the high contact transparency and the effectiveness of the noise filters. Figure 7.8 (a) shows a 2D color map of dI/dV_{SD} as a function of the source-drain voltage V_{SD} and top gate voltage V_G. For the n = 1 peak, the peak position fluctuates, and is the result of heating at such high voltage bias. For peaks of order n = 2 or higher, the peak positions remain constant with change in gate voltage, as expected. This is in contrast to the complicated shifts of MAR peaks around a resonant level in a quantum dot [133,134] and demonstrates the absence of such localized states in the Ge/Si nanowires. Figure 7.8 (b) shows two cuts of the 2D plot at V_G = -700 mV and V_G = -900 mV. We see that the n = 1 peak actually changes to a dip at different gate voltages.

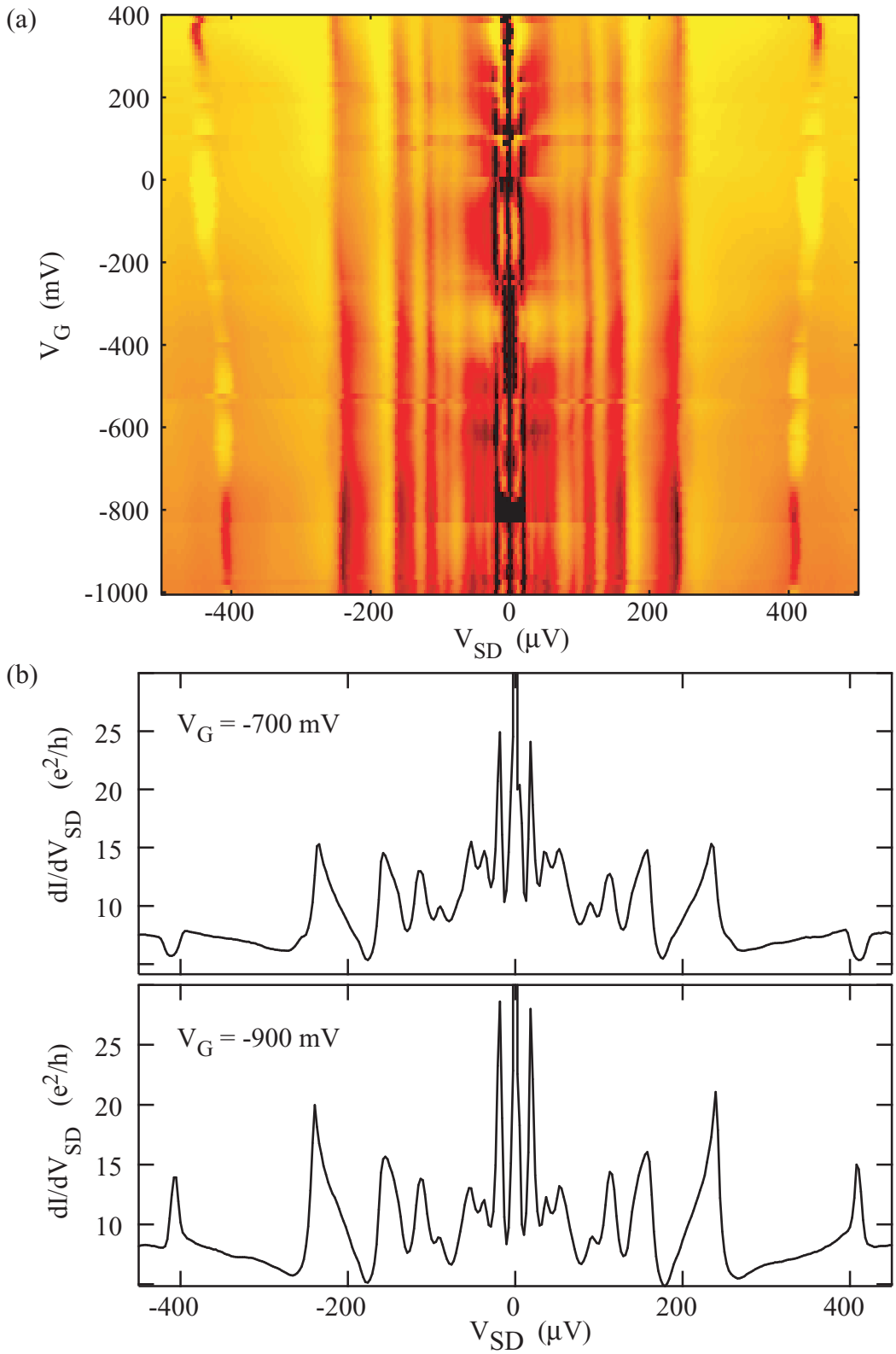

Figure 7.8 (a) dI/dV_{SD} versus V_{SD} and V_G color plot with black corresponding to high conductance and yellow corresponding to low conductance. Multiple Andreev reflection peaks in dI/dV_{SD} are clearly observed. The peak positions remain constant over the entire range of V_G. (b) Two cuts of the color plot in part (a) taken at V_G = -700 mV and V_G = -900 mV. We find that the n = 1 peak changes to a dip for different values of gate voltage.

7.5 Effects of One-Dimensional Quantum Confinement

We now turn to the one-dimensional nature of the nanowire. In Chapter 6, we presented data showing that transport through the Ge/Si nanowire occurs via 1D subbands due to the radial quantum confinement in the Ge core. Figure 7.9 (a) shows a plot of the critical current I_C and the normal state conductance G_N as a function of the gate voltage V_G at T = 60 mK. The normal state conductance was obtained at zero bias while applying a 250 mT magnetic field, which suppresses superconductivity in the aluminum electrodes. We find that both G_N and I_C show step-wise increases as the carrier density is increased. G_N shows plateau features at conductance values of $N \cdot e^2/h$, with N = 3, 4, 6, 8, and 10, indicative of transport through individual 1D subbands. This is similar to Figure 6.5, obtained at higher temperature, which shows clear plateaus corresponding to transport through 1D subbands. The critical current I_C, after being "turned on" at V_G = 870 mV, undergoes a step-wise increase with a step height of $\delta I_C \sim 20$ nA, strongly suggestive of quantization of the superconducting critical current in the Ge/Si nanowire heterostructure. The nanowire remains superconducting once it has been "turned on", in contrast to previous observations in carbon nanotube quantum dot S-N-S junctions where I_C shows oscillatory on-off behavior [134].

The correlation between the plateau features at quantized values in I_C and G_N can in fact be confirmed by plotting the ratio I_C/G_N, or $I_C R_N$, as shown in Figure 7.9 (b). The normal state resistance $R_N = 1/G_N$ is obtained from the slope, at high bias, of V(I) curves similar to those shown in Figures 7.4 and 7.5 (see Section 7.3). The $I_C R_N$ product is essentially a constant around 200 μV, and approximately equal to Δ/e, over a wide range

of gate voltages. It therefore suggests that the quantized steps in I_C occur when individual subbands are populated in the nanowire.

The theory developed by Beenakker and van Houten [125], applicable to our nanowire junctions with length L that is much smaller than the coherence length ξ_0, predicts a universal quantized value of critical current $\delta I_C = e\Delta/\hbar$. From the multiple Andreev reflections, we measured an energy gap $\Delta = 235$ μeV. Therefore, δI_C should equal 57 nA. Our measured δI_C of 20 nA is of the same order of magnitude as the value predicted, but is smaller by a factor of approximately 3. Such a discrepancy may be accounted for by premature switching due to thermal activation in a capacitively and resistively shunted junction [26], which would lead to a measured I_C that is smaller than the actual Josephson critical current.

The work presented here is the first study of proximity effect coupled with discrete 1D modes in the $L << \xi_0$ regime. Previous efforts by other groups investigated quantum point contact junctions with $L >> \xi_0$ and report δI_C that is only within two orders of magnitude from the universal value of $e\Delta/\hbar$ [135,136].

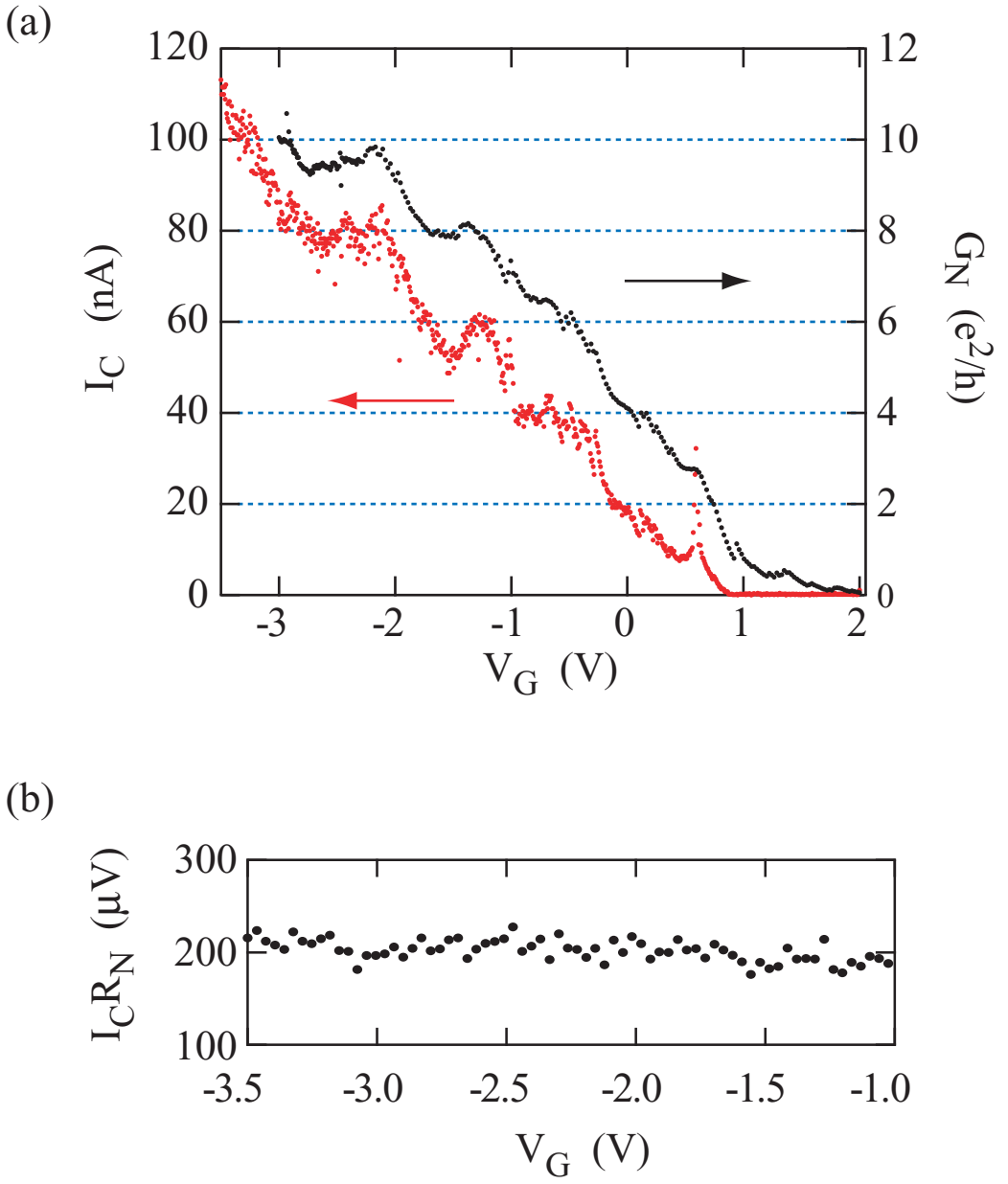

Figure 7.9 (a) Gate voltage dependence of the critical current I_C (red) and normal state conductance G_N (black), measured at T = 60 mK. The normal state conductance was measured at $V_{SD} = 0$ with an applied magnetic field of 250 mT in order to suppress superconductivity in the Al electrodes. A series resistance of 200 Ω is subtracted from the measured conductance. I_C is extracted from individual V-I measurement at the transition from superconducting to resistive states. (b) Product of I_C and R_N versus gate voltage. R_N is extracted from the slope of the individual V-I curves at voltages larger than $2\Delta/e$ (see Figure 7.5).

CONCLUSIONS

The focus of this thesis has been on electron transport in low-dimensional semiconductor systems. Semiconductor nanostructures allowed for systems where the Fermi wavelength was comparable to the size of the nanostructure, leading to quantum confinement of electrons and holes. Charge and spin effects were observed in the context of Coulomb blockade, Kondo effect, and proximity-induced superconductivity. In order to study these effects, semiconductor quantum dots and nanowires were fabricated and measured at low-temperatures. Low-noise transport experiments were performed by properly filtering and grounding the electronic devices.

The main results of the research described in this thesis are: the design, fabrication and measurement of a single-electron rectifier composed of three coupled quantum dots operating in the Coulomb blockade regime; the investigation of a symmetric triple quantum dot system, supplemented by numerical calculations determining the exchange splitting of a two-electron triple dot; measurements of a one- and two-electron quantum dot in the Kondo regime; measurements of a unique core/shell heterostructure nanowire connected to superconducting electrodes.

The work in this thesis is part of the current effort in the condensed matter physics community to create systems, on small length scales, where quantum effects modify the transport properties. The result of such research will be the eventual development of technologically useful artificial systems where the quantum properties of the systems can be controlled and manipulated. Several major challenges, including isolating the system from (thermal) noise and achieving long coherence times, must be

overcome in order to fully utilize these quantum nanostructures. As mentioned in the introduction to this thesis, the interdisciplinary approach taken to the design of such artificial systems, bringing together expertise from physics, chemistry and material science, has had a tremendous positive effect on the progress in this field. Furthermore, new techniques, such as epitaxial heterostructure nanowire growth and atomically-precise instrumentation (i.e., atomic force microscopy), are constantly allowing for new developments in research. Although the challenges that lie ahead are daunting, there is reason to be confident in our ability to overcome them.

REFERENCES

1. For a review, see F. Capasso, in *Semiconductors and Semimetals*, **24**, 319. R.K. Willardson and A.C. Beer, eds. (Academic Press, New York, 1987).

2. K. von Klitzing, G. Dorda and M. Pepper, "New method for high-accuracy determination of the fine-structure constant based on quantized hall resistance," *Phys. Rev. Lett.* **45**, 494 (1980).

3. D.C. Tsui, H.L. Stormer and A.C. Gossard, "Two-dimensional magnetotransport in the extreme quantum limit," *Phys. Rev. Lett.* **48**, 1559 (1982).

4. For a review, see *The Quantum Hall Effect*, R. Prange and S. Girvin, eds. (Springer, New York, 1987).

5. H.L. Stormer, A. Pinczuk, A.C. Gossard and W. Wiegmann, "Influence of undoped (AlGa)As spacer on mobility enhancement in GaAs-(AlGa)As superlattices," *Appl. Phys. Lett.* **38**, 691 (1981).

6. A.C. Gossard, "Molecular beam epitaxy of superlattices in thin films," *Treatise on Materials Science and Technology* **24**, 13 (1982).

7. M.A. Herman and H. Sitter, *Molecular Beam Epitaxy*, (Springer-Verlag, New York, 1989).

8. J.H. Davies, *The physics of low-dimensional semiconductors*, (Cambridge University Press, New York, 1998).

9. J. J. Harris, J. A. Pals and R Woltjer, "Electronic transport in low-dimensional structures," *Rep. Prog. Phys.* **52**, 1217 (1989).

10. T. Ando, A.B. Fowler and F. Stern, "Electronic properties of two-dimensional systems," *Rev. Mod. Phys.* **54**, 437 (1982).

11. H.Z. Zheng, H.P. Wei, D.C. Tsui and G. Weimann, "Gate-controlled transport in narrow GaAs/$Al_xGa_{1-x}As$ heterostructures," *Phys. Rev. B* **34**, 5635 (1986).

12. T.J. Thornton, M. Pepper, H. Ahmed, D. Andrews and G.J. Davies, "One-dimensional conduction in the 2D electron gas of a GaAs-AlGaAs heterojunction," *Phys. Rev. Lett.* **56**, 1198 (1986).

13. Yu. V. Sharvin, *Zh. Eksp. Teor. Fiz.* **48**, 984 (1965); *Sov. Phys. JETP* **21**, 655 (1965).

14. Yu. V. Sharvin and N. I. Bogatina, *Zh. Eksp. Teor. Phys.* **56**, 772 (1969); *Sov. Phys. JETP* **29**, 419 (1969).

15. R. Landauer, "Spatial variation of currents and fields due to localized scatterers in metallic conduction," *IBM J. Res. Dev.* **1**, 223 (1957).

16. R. Landauer, "Spatial variation of currents and fields due to localized scatterers in metallic conduction," *IBM J. Res. Dev.* **32**, 306 (1988).

17. M. Buttiker, "Four-terminal phase-coherent conductance," *Phys. Rev. Lett.* **57**, 1761 (1986).

18. B.J. van Wees, H. van Houten, C.W.J. Beenakker, J.G. Williamson, L.P. Kouwenhoven, D. van der Marel and C.T. Foxon, "Quantized conductance of point contacts in a two-dimensional electron gas," *Phys. Rev. Lett.* **60**, 848 (1988).

19. D.A. Wharam, T.J. Thornton, R. Newbury, M. Pepper, H. Ahmed, J.E.F. Frost, D.G. Hasko, D.C. Peacock, D.A. Ritchie and G.A.C. Jones, "One-dimensional transport and the quantization of the ballistic resistance," *J. Phys. C: Solid State Phys.* **21**, L209 (1988).

20. B.J. van Wees, "Quantum ballistic electron transport and conductance quantization in a constructed two-dimensional electron gas," *Proc. 3rd Int. Symp. Foundations of Quantum Mechanics*, S. Kobayashi, H. Ezawa, Y. Murayama and S. Nomura, eds. (Tokyo, 1990) p.212.

21. C.W.J. Beenakker and H. van Houten, "Quantum transport in semiconductor nanostructures" in *Solid State Physics*, **44**, H. Ehrenreich and D. Turnbull, eds. (Academic Press, San Diego, 1991), p.1.

22. H.R. Zeller and I. Giaver, "Tunneling, zero-bias anomalies, and small superconductors," *Phys. Rev.* **181**, 789 (1969).

23. C.A. Neugebauer and M.B. Webb, "Electrical conduction mechanism in ultrathin, evaporated metal films," *J. Appl. Phys.* **33**, 74 (1962).

24. H. van Houten and C.W.J. Beenakker, "Comment on 'Conductance oscillations periodic in the density of a one-dimensional electron gas'," *Phys. Rev. Lett.* **63**, 1893 (1989).

25. T.A. Fulton and G.J. Dolan, "Observation of single-electron charging effects in small tunnel junctions," *Phys. Rev. Lett.* **59**, 109 (1987).

26. M. Tinkham, *Introduction to Superconductivity*, (McGraw-Hill, New York, 1996).

27. C.W.J. Beenakker, "Theory of Coulomb-blockade oscillations in the conductance of a quantum dot," *Phys. Rev. B* **44**, 1646 (1991).

28. L.P. Kouwenhoven, N.C. van der Vaart, A.T. Johnson, W. Kool, C.J.P.M. Harmans, J.G. Williamson, A.A.M. Staring and C.T. Foxon, "Single electron charging effects in semiconductor quantum dots," *Z. Phys. B* **85**, 367 (1991).

29. C.H. Crouch, *Single Electron Transport and Charge Quantization in Coupled Quantum Dots*, Ph.D. thesis, Harvard University (1996).

30. C. Livermore, C.H. Crouch, R.M. Westervelt, K.L. Campman and A.C. Gossard, "The Coulomb Blockade in Coupled Quantum Dots," *Science* **274**, 1332 (1996).

31. W.G. van der Wiel, S. De Franceschi, J.M. Elzerman, T. Fujisawa, S. Tarucha and L.P. Kouwenhoven, "Electron transport through double quantum dots," *Rev. Mod. Phys.* **75**, 1 (2003).

32. J.M. Golden and B.I. Halperin, "Relation between barrier conductance and Coulomb blockade peak splitting for tunnel-coupled quantum dots," *Phys. Rev. B* **53**, 3893 (1996).

33. J.M. Golden and B.I. Halperin, "Higher-order results for the relation between channel conductance and the Coulomb blockade for two tunnel-coupled quantum dots," *Phys. Rev. B* **54**, 16757 (1996).

34. K.A. Matveev, L.I. Glazman and H.U. Baranger, "Tunneling spectroscopy of quantum charge fluctuations in the Coulomb blockade," *Phys. Rev. B* **53**, 1034 (1996).

35. K.A. Matveev, L.I. Glazman and H.U. Baranger, "Coulomb blockade of tunneling through a double quantum dot," *Phys. Rev. B* **54**, 5637 (1996).

36. I.H. Chan, P. Fallahi, A. Vidan, R.M. Westervelt, M. Hanson and A.C. Gossard, "Few-electron double quantum dots," *Nanotechnology* **15**, 609 (2004).

37. D. Loss and D.P. DiVincenzo, "Quantum computation with quantum dots," *Phys. Rev. A* **57**, 120 (1998).

38. I.H. Chan, *Quantum Dot Circuits: Single-Electron Switch and Few-Electron Quantum Dots*, Ph.D. thesis, Harvard University (2003).

39. R.L. Garwin, "Calculation of heat flow in a medium the conductivity of which varies with temperature," *Rev. Sci. Instrum.* **27**, 826 (1956).

40. R.C. Richardson and E.N. Smith, *Experimental Techniques in Condensed Matter Physics at Low Temperatures*, (Addison-Wesley, Menlo Park, 1988) p.120.

41. H. London, *Proc. Int. Conf. on Low Temp. Phys.*, (Oxford, 1951) p.157.

42. O.V. Lounasmaa, *Experimental Principles and Methods Below 1 K*, (Academic Press, New York, 1974).

43. M.A. Kastner, "Artificial Atoms," *Physics Today* **46**, 24 (1993).

44. L.P. Kouwenhoven, C.M. Marcus, P. McEuen, S. Tarucha, R.M. Westervelt and N. Wingreen, in *Mesoscopic Electron Transport*, L.L. Sohn, L.P. Kouwenhoven and G. Schön, eds. (Kluwer, Dordrecht, 1997), p. 105.

45. F.R. Waugh, R.M. Westervelt, K. Campman and A.C. Gossard, "Single-electron charging in double and triple quantum dots with tuneable coupling," *Phys. Rev. Lett.* **75**, 705 (1995).

46. K. K. Likharev, *Proceedings of the IEEE* **87**, 606 (1999).

47. D.S. Duncan, C. Livermore, R.M. Westervelt, K.D. Maranowski and A.C.Gossard, "Direct Measurement of the Destruction of Charge Quantization in a Single Electron Box," *Appl. Phys. Lett.* **74**, 1045 (1999).

48. I.H. Chan, R.M. Westervelt, K.D. Maranowski and A.C. Gossard, "Strongly Capacitively Coupled Quantum Dots," *Appl. Phys. Lett.* **80**, 1818 (2002).

49. K.K. Likharev and A.N. Korotkov, "Single-Electron Parametron: Reversible Computation in a Discrete-State System," *Science* **273**, 763 (1996).

50. M. Stopa, "Rectifying behavior in Coulomb blockades: charging rectifiers," *Phys. Rev. Lett.* **88**, 146802 (2002).

51. A. Vidan, R.M. Westervelt, M. Stopa, M. Hanson and A.C. Gossard, "Triple Quantum Dot Charging Rectifier," *Appl. Phys. Lett.* **85**, 3602 (2004).

52. D.S. Saraga and D. Loss, "Spin-entangled currents created by a triple quantum dot," *Phys. Rev. Lett.* **90**, 166803 (2003).

53. L. Gaudreau, S. Studenikin, A. Sachrajda, P. Zawadzki, A. Kam, J. Lapointe, M. Korkusinski and P. Hawrylak, "The stability diagram of a few electron artificial triatom," cond-mat/0601597

54. *Single Charge Tunneling*, H. Grabert and M.H. Devoret, eds. (Plenum, New York, 1992).

55. H. Linke, W. Sheng, A. Lofgren, H. Xu, P. Omling and P.E. Lindelof, "A quantum dot ratchet: Experiment and theory," *Europhys. Lett.* **44**, 341 (1998).

56. H. Linke, T.E. Humphrey, A. Lofgren, A.O. Sushkov, R. Newbury, R.P. Taylor and P. Omling, "Experimental tunneling ratchets," *Science* **286**, 2314 (1999).

57. For a review, see P. Reimann, "Brownian motors: Noisy transport far from equilibrium," *Phys. Rep.* **361**, 57 (2002).

58. C. Joachim, J.K. Gimzewski and A. Aviram, "Electronics using hybrid-molecular and mono-molecular devices," *Nature* **408**, 541 (2000).

59. K. Ono, D. G. Austing, Y. Tokura and S. Tarucha, "Current rectification by Pauli exclusion in a weakly coupled double quantum dot system," *Science* **297**, 1313 (2002).

60. M. Stopa, "Quantum dot self-consistent electronic structure and the Coulomb blockade," *Phys. Rev. B* **54**, 13767 (1996).

61. W.G. van der Wiel, M. Stopa, T. Kodera, T. Hatano and S. Tarucha, "Semiconductor quantum dots for electron spin qubits," *New Journal of Physics* **8**, 26 (2006).

62. G. Burkard, D. Loss and D. P. DiVincenzo, "Coupled quantum dots as quantum gates," *Phys. Rev. B* **59**, 2070 (1999).

63. T. Hatano, M. Stopa, T. Yamaguchi, T. Ota, K. Yamada and S. Tarucha, "Electron-spin and electron-orbital dependence of the tunnel coupling in laterally coupled double vertical dots," *Phys. Rev. Lett.* **93**, 066806 (2004).

64. X. Hu and S. Das Sarma, "Hilbert-space structure of a solid-state quantum computer: Two-electron states of a double-quantum-dot artificial molecule," *Phys. Rev. A* **61**, 062301 (2000).

65. V. Fock, "Bemerkung zur Quantelung des harmonischen Oszillators im Magnetfeld," *Z. Phys.* **47**, 446 (1928); C.G. Darwin, "The diamagnetism of the free electron," *Proc. Cambridge Philos. Soc.* **27**, 86 (1930).

66. A. Harrison, "First catch your hare: The design and synthesis of frustrated magnets," *J. Phys.: Condens. Matter* **16**, S553 (2004), and the references cited therein.

67. M. Ciorga, A.S. Sachrajda, P. Hawrylak, C. Gould, P. Zawadzki, Y. Feng and Z. Wasilewski, "Addition spectrum of a lateral dot from Coulomb and spin-blockade spectroscopy," *Phys. Rev. B* **61**, R16315 (2000).

68. Y. Wang, N.S. Rogado, R.J. Cava and N.P. Ong, "Spin entropy as the likely source of enhanced thermopower in $Na_xCo_2O_4$," *Nature* **423**, 425 (2003).

69. C.W.J. Beenakker and A.A.M. Staring, "Theory of the thermopower of a quantum dot," *Phys Rev. B* **46**, 9667 (1992).

70. A.S. Dzurak, C.G. Smith, C.H.W. Barnes, M. Pepper, L. Martin-Moreno, C.T. Liang, D.A. Ritchie and G.A.C. Jones, "Thermoelectric signature of the excitation spectrum of a quantum dot," *Phys. Rev. B* **55**, R10197 (1997).

71. J. Kondo, "Resistance minimum in dilute magnetic alloys," *Prog. Theor. Phys.* **32**, 37 (1964).

72. A.C. Hewson, *The Kondo Problem to Heavy Fermions*, Cambridge Studies in Magnetism (Cambridge University Press, Cambridge, 1993).

73. S. De Franceschi, S. Sasaki, J.M. Elzerman, W.G. van der Wiel, S. Tarucha and L.P. Kouwenhoven, "Electron Cotunneling in a Semiconductor Quantum Dot," *Phys. Rev. Lett.* **86**, 878 (2001).

74. J. Nygard, D.H. Cobden and P.E. Lindelof, "Kondo physics in carbon nanotubes," *Nature* **408**, 342 (2000).

75. W.J. deHaas, J.H. de Boer and G. J. van den Berg, "The electrical resistance of gold, copper and lead at low temperatures," *Physica* **1**, 1115 (1934).

76. P.W. Anderson, "Localized magnetic states and fermi-surface anomalies in tunneling," *Phys. Rev. Lett.* **17**, 95 (1966).

77. L.I. Glazman and M.E. Raikh, "Resonant Kondo transparency of a barrier with quasilocal impurity states," *Pis'ma Zh. Eksp. Teor. Fiz.* **47**, 378 (1988); *JETP Lett.* **47**, 452 (1988).

78. T.K. Ng and P.A. Lee, "On-site Coulomb repulsion and resonant tunneling," *Phys. Rev. Lett.* **61**, 1768 (1988).

79. D. Goldhaber-Gordon, H. Shtrikman, D. Mahalu, D. Abusch-Maggder, U. Meirav and M.A. Kastner, "Kondo effect in a single-electron transistor," *Nature* **391**, 156 (1998).

80. S.M. Cronenwett, T.H. Oosterkamp and L.P. Kouwenhoven, "A tunable Kondo effect in quantum dots," *Science* **281**, 540 (1998).

81. J. Schmid, J. Weis, K. Eberl and K. von Klitzing, "A quantum dot in the limit of strong coupling to reservoirs," *Physica B* **256**, 182 (1998).

82. F. Simmel, R.H. Blick, J.P. Kotthaus, W. Wegscheider and M. Bichler, "Anomalous Kondo effect in a quantum dot at nonzero bias," *Phys. Rev. Lett.* **83**, 804 (1999).

83. S. De Franceschi, R. Hanson, W.G. van der Wiel, J.M. Elzerman, J.J. Wijpkema, T. Fujisawa, S. Tarucha and L.P. Kouwenhoven, "Out-of-equilibrium Kondo effect in a mesoscopic device," *Phys. Rev. Lett.* **89**, 156801 (2002).

84. J. Schmid, J. Weis, K. Eberl and K. von Klitzing, "Absence of odd-even parity behavior for Kondo resonances in quantum dots," *Phys. Rev. Lett.* **84**, 5824 (2000).

85. S. Sasaki, S. De Franceschi, J.M. Elzerman, W.G. van der Wiel, M. Eto, S. Tarucha and L.P. Kouwenhoven, "Kondo effect in an integer-spin quantum dot," *Nature* **405**, 764 (2000).

86. A. Kogan, G. Granger, M.A. Kastner, D. Goldhaber-Gordon and H. Shtrikman, "Singlet–triplet transition in a single-electron transistor at zero magnetic field," *Phys. Rev. B* **67**, 113309 (2003).

87. P.W. Anderson, "Localized magnetic states in metals," *Phys. Rev.* **124**, 41 (1961).

88. F.D.M. Haldane, "Scaling theory of the asymmetric Anderson model," *Phys. Rev. Lett.* **40**, 416 (1978).

89. D. Goldhaber-Gordon, J. Göres, M.A. Kastner, H. Shtrikman, D. Mahalu and U. Meirav, "From the Kondo regime to the mixed-valence regime in a single-electron transistor," *Phys. Rev. Lett.* **81**, 5225 (1998).

90. S. Amasha, I.J. Gelfand, M.A. Kastner and A. Kogan, "Kondo temperature dependence of the Kondo splitting in a single-electron transistor," *Phys. Rev. B* **72**, 045308 (2005).

91. Y. Meir, N.S. Wingreen and P.A. Lee, "Low-temperature transport through a quantum dot: The Anderson model out of equilibrium," *Phys. Rev. Lett.* **70**, 2601 (1993).

92. N.S. Wingreen and Y. Meir, "Anderson model out of equilibrium: Noncrossing-approximation approach to transport through a quantum dot," *Phys. Rev. B* **49**, 11040 (1994).

93. L. Wang, J.K. Zhang and A.R. Bishop, "Microscopic theory for conductance oscillations of electron tunneling through a quantum dot," *Phys. Rev. Lett.* **73**, 585 (1994).

94. M. Field, C.G. Smith, M. Pepper, D.A. Ritchie, J.E.F. Frost, G.A.C. Jones and D.G. Hasko, "Measurements of Coulomb blockade with a noninvasive voltage probe," *Phys. Rev. Lett.* **70**, 1311 (1993).

95. M. Pioro-Ladrière, J.H. Davies, A.R. Long, A.S. Sachrajda, L. Gaudreau, P. Zawadzki, J. Lapointe, J. Gupta, Z. Wasilewski and S. Studenikin, "Origin of switching noise in GaAs/$Al_xGa_{1-x}As$ lateral gated devices," *Phys. Rev. B* **72**, 115331 (2005).

96. T.A. Costi, "Kondo effect in a magnetic field and the magnetoresistivity of Kondo alloys," *Phys. Rev. Lett.* **85**, 1504 (2000).

97. A. Kogan, S. Amasha, D. Goldhaber-Gordon, G. Granger, M.A. Kastner and H. Shtrikman, "Measurements of Kondo and spin splitting in single-electron transistors," *Phys. Rev. Lett.* **93**, 166602 (2004).

98. D.M. Zumbuhl, C.M. Marcus, M.P. Hanson, and A.C. Gossard, "Cotunneling spectroscopy in few-electron quantum dots," *Phys. Rev. Lett.* **93**, 256801 (2004).

99. T. Inoshita, A. Shimizu, Y. Kuramoto and H. Sakaki, "Correlated electron transport through a quantum dot: The multiple-level effect," *Phys. Rev. B* **48**, R14725 (1993).

100. T. Inoshita, A. Shimizu, Y. Kuramoto and H. Sakaki, "Nonlinear low-temperature transport of electrons through a multilevel quantum dot," *Superlattices Microstruct.* **22**, 75 (1997).

101. C.M. Lieber (private communication).

102. J.E. Moore and X-G. Wen, "Anomalous magnetic splitting of the Kondo resonance," *Phys. Rev. Lett.* **85**, 1722 (2000).

103. C.M. Lieber, "Nanoscale science and technology: Building a big future from small things," *MRS Bull.* **28**, 486 (2003).

104. P.M. Mooney and J.O. Chu, "SiGe technology: Heteroepitaxy and high-speed microelectronics," *Annu. Rev. Mater. Sci.* **30**, 335 (2000).

105. R.S. Wagner and W.C. Ellis, "Vapor-liquid-solid mechanism of single crystal growth," *Appl. Phys. Lett.* **4**, 89 (1964).

106. R.S. Wagner, in *Whisker Technology*, A.P. Levitt, ed. (Wiley-Interscience, New York, 1970), pp. 47-119.

107. M. Yazawa, M. Koguchi and K. Hiruma, "Heteroepitaxial ultrafine wire-like growth of InAs on GaAs substrates," *Appl. Phys. Lett.* **58**, 1080 (1991).

108. K. Haraguchi, T. Katsuyama, K. Hiruma and K. Ogawa, "GaAs p-n junction formed in quantum wire crystals," *Appl. Phys. Lett.* **60**, 745 (1992).

109. K. Hiruma, M. Yazawa, T. Katsuyama, K. Ogawa, K. Haraguchi, M. Koguchi and H. Kakibayashi "Growth and optical properties of nanometer-scale GaAs and InAs whiskers," *J. Appl. Phys.* **77**, 447 (1995).

110. L.J. Lauhon, M.S. Gudiksen, D. Wang and C.M. Lieber "Epitaxial core-shell and core-multi-shell nanowire heterostructures," *Nature* **420**, 57 (2002).

111. W. Lu, J. Xiang, B.P. Timko, Y. Wu and C.M. Lieber, "One-dimensional hole gas in germanium/silicon nanowire heterostructures," *Proc. Natl. Acad. Sci. USA* **102**, 10046 (2005).

112. M. Ritala and M. Leskelä, "Atomic layer epitaxy - a new tool for nanotechnology?" *Nanotechnology* **10**, 19 (1999).

113. L.P. Kouwenhoven, B.J. van Wees, C.J.P.M. Harmans, J.G. Williamson, H. van Houten, C.W.J. Beenakker, C.T. Foxon and J. J. Harris, "Nonlinear conductance of quantum point contacts," *Phys. Rev. B* **39**, 8040 (1989).

114. B.J. van Wees, L.P. Kouwenhoven, E.M.M. Willems, C.J.P.M. Harmans, J.E. Mooij, H. van Houten, C.W.J. Beenakker, J.G. Williamson and C. T. Foxon, "Quantum ballistic and adiabatic electron transport studied with quantum point contacts," *Phys. Rev. B* **43**, 12431 (1991).

115. N.K. Patel, J.T. Nicholls, L. Martn-Moreno, M. Pepper, J.E.F. Frost, D.A. Ritchie and G.A.C. Jones, "Evolution of half plateaus as a function of electric field in a ballistic quasi-one-dimensional constriction," *Phys. Rev. B* **44**, 13549 (1991).

116. L.N. Cooper, "Bound electron pairs in a degenerate Fermi gas," *Phys. Rev.* **104**, 1189 (1956).

117. J. Bardeen, L.N. Cooper and J.R. Schrieffer, "Theory of superconductivity," *Phys. Rev.* **108**, 1175 (1957).

118. A.F. Andreev, *Zh. Eksp. Teor. Fiz.* **46**, 1823 (1964); *Sov. Phys. JETP* **19**, 1228 (1964); **51**, 1510 (1966); **24**, 1019 (1967).

119. T.M. Klapwijk, "Proximity effect from an Andreev perspective," *Journal of Superconductivity: Incorporating Novel Magnetism* **17**, 593 (2004).

120. G.E. Blonder, M. Tinkham and T.M. Klapwijk, "Transition from metallic to tunneling regimes in superconducting microconstrictions: Excess current, charge imbalance, and supercurrent conversion," *Phys. Rev. B* **25**, 4515 (1982).

121. K.K. Likharev, "Superconducting weak links," *Rev. Mod. Phys.* **51**, 101 (1979).

122. *Superconducting Devices*, S.T. Ruggiero and D.A. Rudman, eds., (Academic Press, San Diego, 1990).

123. T.D. Clark, R.J. Prance and A.D.C. Grassie, "Feasibility of hybrid Josephson field effect transistors," *J. Appl. Phys.* **51**, 2736 (1980).

124. H. van Houten, "Three-terminal quantum box resonant tunneling Josephson field-effect switch," *Appl. Phys. Lett.* **58**, 1326 (1991).

125. C.W.J. Beenakker and H. van Houten, "Josephson current through a superconducting point contact shorter than the coherence length," *Phys. Rev. Lett.* **66**, 3056 (1991).

126. C.J. Muller, J.M. van Ruitenbeek and L.J. de Jongh, "Conductance and supercurrent discontinuities in atomic-scale metallic constrictions of variable width," *Phys. Rev. Lett.* **69**, 140 (1992)

127. J. Martinis, M. Devoret and J. Clarke, "Experimental tests for the quantum behavior of a macroscopic degree of freedom: The phase difference across a Josephson junction," *Phys. Rev. B* **35**, 4682 (1987).

128. Y.J. Doh, J.A. van Dam, A.L. Roest, E.P.A.M. Bakkers, L.P. Kouwenhoven and S. De Franceschi, "Tunable supercurrent through semiconductor nanowires," *Science* **309**, 272 (2005).

129. K. Flensberg, J.B. Hansen and M. Octavio, "Subharmonic energy-gap structure in superconducting weak links," *Phys. Rev. B* **38**, 8707 (1988).

130. T.-C. Wei, D. Pekker, A. Rogachev, A. Bezryadin and P.M. Goldbart, "Enhancing superconductivity: Magnetic impurities and their quenching by magnetic fields," cond-mat/0510476

131. A. Rogachev, T.-C. Wei, D. Pekker, A.T. Bollinger, P.M. Goldbart and A. Bezryadin, "Magnetic field enhancement of superconductivity in ultra-narrow wires," cond-mat/0604351

132. M. Octavio, W.J. Skocpol and M. Tinkham, "Improved performance of tin variable-thickness superconducting microbridges," *IEEE Transactions on Magnetics*, **MAG-13**, 739 (1977).

133. M.R. Buitelaar, W. Belzig, T. Nussbaumer, B. Babic, C. Bruder and C. Schoenenberger, "Multiple Andreev reflections in a carbon nanotube quantum dot," *Phys. Rev. Lett.* **91**, 057005 (2003).

134. P. Jarillo-Herrero, J.A. van Dam and L.P. Kouwenhoven, "Quantum supercurrent transistors in carbon nanotubes," *Nature* **439**, 953 (2006).

135. H. Takayanagi, T. Akazaki and J. Nitta, "Observation of maximum supercurrent quantization in a superconducting quantum point contact," *Phys. Rev. Lett.* **75**, 3533 (1995).

136. T. Bauch, E. Hürfeld, V.M. Krasnov, P. Delsing, H. Takayanagi and T. Akazaki, "Correlated quantization of supercurrent and conductance in a superconducting quantum point contact," *Phys. Rev. B* **71**, 174502 (2005).